

© 2012

ZIQING DUAN

ALL RIGHTS RESERVED

**MOCVD GROWTH OF $\text{Mg}_x\text{Zn}_{1-x}\text{O}$ FILMS AND NANOSTRUCTURES FOR
PHOTOVOLTAICS**

by

ZIQING DUAN

A Dissertation submitted to the

Graduate School-New Brunswick

Rutgers, The State University of New Jersey

In partial fulfillment of the requirements

For the degree of

Doctor of Philosophy

Graduate Program in Electrical and Computer Engineering

Written under the direction of

Professor Yicheng Lu

And approved by

New Brunswick, New Jersey

MAY, 2012

ABSTRACT OF THE DISSERTATION

MOCVD GROWTH OF $\text{Mg}_x\text{Zn}_{1-x}\text{O}$ FILMS AND NANOSTRUCTURES FOR PHOTOVOLTAICS

By ZIQING DUAN

Dissertation Director:
Professor Yicheng Lu

$\text{Mg}_x\text{Zn}_{1-x}\text{O}$, which is formed by alloying ZnO with MgO, has been developed as a promising window layer in chalcopyrite thin film solar cells and hybrid polymer solar cells for enhanced open-circuit voltage and solar conversion efficiency because of its bandgap tunability. The surface morphology of $\text{Mg}_x\text{Zn}_{1-x}\text{O}$ layers in those photovoltaic applications plays important roles on the performances of solar cells. Two-dimensional (2-D) dense and smooth film is preferred in the inorganic p-n junction solar cells while one-dimensional (1-D) nanostructures are favorable for the hybrid polymer solar cells. In this dissertation, metal-organic chemical vapor deposition (MOCVD) is used to grow both of $\text{Mg}_x\text{Zn}_{1-x}\text{O}$ polycrystalline 2-D films and single crystalline 1-D nanostructures for solar cells. A low-temperature ($\sim 250^\circ\text{C}$) ZnO buffer layer, followed by the high-temperature ($\sim 500^\circ\text{C}$) growth of $\text{Mg}_x\text{Zn}_{1-x}\text{O}$, is found to be beneficial for the formation of a 2-D dense and smooth film. On the other hand, a high-temperature ($\sim 520^\circ\text{C}$) ZnO buffer layer followed by a high temperature (530°C - 560°C) growth of $\text{Mg}_x\text{Zn}_{1-x}\text{O}$ is

needed to grow the 1-D $\text{Mg}_x\text{Zn}_{1-x}\text{O}$ ($0 \leq x \leq 0.15$) nanostructures on Si. For the first time, 1-D $\text{Mg}_x\text{Zn}_{1-x}\text{O}$ nanostructures ($0 \leq x \leq 0.1$) are sequentially grown on a Ga-doped ZnO (GZO) 2-D film to form the 3-D photoelectrode, which is used to fabricate the P3HT- $\text{Mg}_x\text{Zn}_{1-x}\text{O}$ hybride solar cells. The preliminary testing results of solar cells show that $\text{Mg}_x\text{Zn}_{1-x}\text{O}$ is promising to be used in hybrid polymer solar cells for the enhancement of open circuit voltage (V_{OC}). $\text{Mg}_x\text{Zn}_{1-x}\text{O}$ ($0 \leq x \leq 0.1$) polycrystalline films are used in Cu_2O - $\text{Mg}_x\text{Zn}_{1-x}\text{O}$ heterojunction solar cells. The current density-voltage (J-V) measurements of solar cells under illumination show that V_{OC} , shunt resistance R_{sh} and the solar conversion efficiency η are improved with increasing of Mg% until 10%. A relatively high solar conversion efficiency, $\eta_{AM1.5} = 0.71 \%$ with a short circuit current $J_{SC} = 3.0 \text{ mA/cm}^2$ and $V_{OC} = 575 \text{ mV}$, is obtained on the $\text{Mg}_{0.1}\text{Zn}_{0.9}\text{O}$ sample. The band alignment between Cu_2O and $\text{Mg}_x\text{Zn}_{1-x}\text{O}$ is analyzed by using X-ray photoelectron spectroscopy (XPS) measurements.

DEDICATED TO

My mom, my old brother and other family members

Acknowledgements

I am heartily thankful to my dissertation advisor, Professor Yicheng Lu, whose continuous support, invaluable guidance, sound advice and encouragement enabled me to successfully complete my doctoral studies and PhD thesis. His motivation, enthusiasm, carefulness, responsibility and immense knowledge have inspired me to get improvement not only in scientific and technical skills but also personal attributes.

I would like to show my gratitude to Dr. Aurelien Du Pasquier for his great help in photovoltaic solar cells fabrication, testing, results analysis and discussion. This thesis would not have been possible without his helpful contribution.

I would like to sincerely thank my thesis committee: Prof. Wei Jiang, Prof. Jaeseok Jeon, Dr. Warren Lai and Prof. Frederic Cosandey for their encouragement, helpful advices, insightful comments and questions. I appreciate they were taking time to review this dissertation and contribute on the thesis modification.

I am also grateful to senior students in our group, Dr. Hanhong Chen, Dr. Gaurav Saraf and Dr. Jian Zhong. Their kind guidance, assistance, teaching and help in MOCVD film growth, material characterization and development of research skills during the first several years of my PhD study made me quickly involved in my PhD research projects.

I wish to thank all my group members, including Mr. Pavel Reyes, Mr. Chieh-Jen Ku, Mr. Yang Zhang, Mr. Rui Li, Mr. Wen-Chiang Hong, Mr. Faraz Khan and other previous senior students, postdoctors and visiting scholars, for their discussion, assistance, collaboration and help throughout my whole PhD study in Rutgers University.

Table of Contents

Abstract.....	ii
Acknowledgements.....	v
Table of Contents.....	vi
List of Tables.....	viii
Lists of Illustrations.....	ix
Chapter 1 Introduction.....	1
1.1 Motivation.....	1
1.2 Objectives.....	4
1.3 Dissertation Organization.....	5
Chapter 2 Technical Background.....	7
2.1 Fundamental properties of $\text{Mg}_x\text{Zn}_{1-x}\text{O}$ alloy and its applications.....	7
2.2 Growth technologies of $\text{Mg}_x\text{Zn}_{1-x}\text{O}$ polycrystalline films.....	15
2.3 Growth technologies of $\text{Mg}_x\text{Zn}_{1-x}\text{O}$ nanostructures.....	24
2.4 Metalorganic chemical vapor deposition.....	30
2.5 Summary.....	41
Chapter 3 Growth and characterization of $\text{Mg}_x\text{Zn}_{1-x}\text{O}$ polycrystalline films.....	42
3.1 Growth optimization of Ga-doped ZnO (GZO) films.....	43
3.2 Growth of $\text{Mg}_x\text{Zn}_{1-x}\text{O}$ polycrystalline films on GZO films.....	51
3.3 Summary.....	57
Chapter 4 Growth and characterization of $\text{Mg}_x\text{Zn}_{1-x}\text{O}$ nanostructures.....	59
4.1 Growth optimization of $\text{Mg}_x\text{Zn}_{1-x}\text{O}$ nanostructures on Si substrates.....	59
4.2 Growth optimization of $\text{Mg}_x\text{Zn}_{1-x}\text{O}$ nanostructures on GZO films.....	72

4.3 Summary.....	76
Chapter 5 Photovoltaic cells fabricated on $\text{Mg}_x\text{Zn}_{1-x}\text{O}$ films and nanostructures.....	77
5.1 P3HT- $\text{Mg}_x\text{Zn}_{1-x}\text{O}$ hybrid solar cells.....	78
5.1.1 Solar cell structure and operating mechanism.....	78
5.1.2 Solar cell testing system.....	83
5.1.3 Preliminary results of solar cells.....	86
5.2 Cu_2O - $\text{Mg}_x\text{Zn}_{1-x}\text{O}$ heterojunction thin film solar cells.....	89
5.2.1 Solar cell structure and fabrication.....	90
5.2.2 Testing results of Cu_2O - $\text{Mg}_x\text{Zn}_{1-x}\text{O}$ heterojunction solar cells.....	101
5.2.3 The effect of Mg composition on V_{OC}	103
5.3 Summary.....	110
Chapter 6 Conclusions and suggestions for future work.....	112
6.1 Conclusions.....	112
6.2 Suggestions for future work.....	115
References.....	118
Curriculum Vitae.....	125

Lists of tables

Table 2.1 Comparison of growth technologies for $\text{Mg}_x\text{Zn}_{1-x}\text{O}$ polycrystalline films. *Page 23*

Table 2.2 Comparison of growth technologies for $\text{Mg}_x\text{Zn}_{1-x}\text{O}$ nanostructures. *Page 30*

Table 2.3 Vapor pressure and melting point of metalorganic precursors. *Page 38*

Table 5.1 Photovoltaic parameters of the $\text{FTO}/\text{Mg}_x\text{Zn}_{1-x}\text{O}-\text{Cu}_2\text{O}/\text{Ag}$ solar cells with different Mg composition x examined under AM1.5 simulated sunlight. *Page 101*

List of illustrations

Figure 2.1 The schematic illustrations: (a) the crystal structure of wurtzite ZnO; (b) the projection along the $[11\bar{2}0]$ direction. *Page 8*

Figure 2.2 Crystal structure of rocksalt MgO (Cubic). *Page 10*

Figure 2.3 Equilibrium phase diagram of the MgO-ZnO system. *Page 12*

Figure 2.4 Band-gap energy as a function of Mg content in $\text{Mg}_x\text{Zn}_{1-x}\text{O}$ films. *Page 13*

Figure 2.5 A schematic diagram of Rutgers MOCVD system for the growth of ZnO-based films and nanostructures. *Page 32*

Figure 2.6 A schematic diagram of Rutgers MOCVD growth reactor for ZnO and $\text{Mg}_x\text{Zn}_{1-x}\text{O}$ growth. *Page 35*

Figure 2.7 A schematic diagram of the flow patterns in an axisymmetric rotating-disk vertical flow reactor. *Page 37*

Figure 3.1 Resistivity of GZO films as a function of Ga content. *Page 46*

Figure 3.2 XRD results of GZO films with different Ga content, in which pure ZnO is included for a comparison. *Page 47*

Figure 3.3 XRD patterns of GZO films with same Ga content (~10%) grown at different T_s . *Page 48*

Figure 3.4 Transmission spectra of GZO film with a 10% of Ga% and a low resistivity of $9.6 \times 10^{-4} \text{ ohm}\cdot\text{cm}$. *Page 49*

Figure 3.5 FESEM image of GZO film with a 10% of Ga% and a low resistivity of $9.6 \times 10^{-4} \text{ ohm}\cdot\text{cm}$. *Page 50*

Figure 3.6 FESEM images of (a) $\text{Mg}_{0.08}\text{Zn}_{0.92}\text{O}$ film grown on GZO without a buffer layer, (b) $\text{Mg}_{0.08}\text{Zn}_{0.92}\text{O}$ film grown on GZO with a LT ZnO buffer layer. *Page 52*

Figure 3.7 AFM images of $\text{Mg}_{0.08}\text{Zn}_{0.92}\text{O}$ film grown on GZO film (a) without any buffer, (b) with a LT ZnO buffer. *Page 53*

Figure 3.8 The XRD pattern of (i) GZO film on glass, (ii) $\text{Mg}_{0.08}\text{Zn}_{0.92}\text{O}$ film grown on glass, (iii) $\text{Mg}_{0.08}\text{Zn}_{0.92}\text{O}$ film grown on GZO film without a buffer and (iv) and $\text{Mg}_{0.08}\text{Zn}_{0.92}\text{O}$ film grown on GZO film with a LT ZnO buffer. *Page 55*

Figure 4.1 FESEM images of $\text{Mg}_x\text{Zn}_{1-x}\text{O}$ nanotips grown on Si substrates at different T_s (a) 500°C, (b) 530°C, (c) 560°C, (d) 590°C. *Page 61*

Figure 4.2 Transmission spectra of $\text{Mg}_x\text{Zn}_{1-x}\text{O}$ nanotips grown under different T_s from 500°C to 590°C. The transmission spectrum of ZnO is included as a reference. *Page 62*

Figure 4.3 Transmission spectra of $\text{Mg}_x\text{Zn}_{1-x}\text{O}$ nanotips grown with different O/Zn precursors flow rate ratios. (a) O/Zn flow ratio is 2250/65; (b) O/Zn flow ratio is 2250/45. *Page 64*

Figure 4.4 Relationship between the maximum Mg incorporation and the flow rate of DEZn, under the fixed O_2 flow rate (2250 sccm). *Page 65*

Figure 4.5 FESEM images of $\text{Mg}_x\text{Zn}_{1-x}\text{O}$ ($x \sim 7\%$) samples grown on different buffer layers. (a) no buffer; (b) a LT ZnO buffer; (c) a low-T MgZnO buffer; (d) a high-T ZnO buffer. *Page 70*

Figure 4.6 XRD patterns of $\text{Mg}_{0.07}\text{Zn}_{0.93}\text{O}$ samples grown on different buffer layers. *Page 71*

Figure 4.7 FESEM images of $\text{Mg}_x\text{Zn}_{1-x}\text{O}$ nanostructures on GZO films with (a) $x=0$, (b) $x=0.04$, (c) $x=0.06$, (d) $x=0.08$, (e) $x=0.10$ and (f) $x=0.12$. *Page 74*

Figure 4.8 Transmission spectra of 1-D $\text{Mg}_x\text{Zn}_{1-x}\text{O}$ ($0 \leq x \leq 0.10$) nanostructures. *Page 75*

Figure 5.1 A schematic diagram of Ag-P3HT-Mg_xZn_{1-x}O-GZO/glass solar cell. *Page 80*

Figure 5.2 Band diagram of Ag-P3HT-Mg_xZn_{1-x}O-GZO/glass solar cell. *Page 81*

Figure 5.3 Band diagram of ITO-Mg_xZn_{1-x}O-P3HT-Ag hybrid polymer-metal oxide device, showing the effect of Mg content on the V_{OC} of the device. *Page 82*

Figure 5.4 Schematic illustration of solar cell testing system, (a) quantum efficiency measurements; (b) power conversion efficiency measurements. *Page 85*

Figure 5.5 UV-vis spectra of the GZO-Mg_xZn_{1-x}O-P3HT solar cells with x= 0, 0.04, 0.05. *Page 87*

Figure 5.6 J-V curves of GZO-Mg_{0.04}Zn_{0.96}O-P3HT solar cells in the dark and under 1 sun before and after annealing. *Page 88*

Figure 5.7 The schematic diagram of Ag-Cu₂O-Mg_xZn_{1-x}O-FTO heterojunction solar cells. *Page 91*

Figure 5.8 (a) Transmission spectra of Mg_xZn_{1-x}O (0 ≤ x ≤ 0.13) films, (b) Plots of α² versus hν for Mg_xZn_{1-x}O (0 ≤ x ≤ 0.13) films. *Page 93*

Figure 5.9 FESEM images of as-grown $\text{Mg}_x\text{Zn}_{1-x}\text{O}$ layers with (a) $x = 0$ and (b) $x = 0.10$.

Page 94

Figure 5.10 Resistivity of $\text{Mg}_x\text{Zn}_{1-x}\text{O}$ ($0 \leq x \leq 0.13$) films as a function of Mg content (x). *Page 95*

Figure 5.11 (a) an FESEM image of the Cu_2O film deposited on $\text{Mg}_{0.1}\text{Zn}_{0.9}\text{O}$ -FTO films; (b) A plot of α^2 versus photon energy ($h\nu$) for the Cu_2O film. *Page 98*

Figure 5.12 A typical XRD pattern of the Cu_2O film. *Page 99*

Figure 5.13 (a) The Cu $2p_{3/2}$ XPS spectrum from a Cu_2O film; (b) Cu LMM-2 Auguer peak of Cu_2O film. *Page 100*

Figure 5.14 Current density (J)-voltage (V) characteristics of FTO/ $\text{Mg}_x\text{Zn}_{1-x}\text{O}$ - Cu_2O /Ag solar cells under AM1.5 simulated sunlight. *Page 102*

Figure 5.15 XPS spectra of (a) a Cu_2O -ZnO heterojunction, (b) a Cu_2O - $\text{Mg}_{0.1}\text{Zn}_{0.9}\text{O}$ heterojunction, showing the binding energy separations (i) between the Zn $2p_{3/2}$ core level and the VBM of bulk ZnO (a), bulk $\text{Mg}_{0.1}\text{Zn}_{0.9}\text{O}$ (b), (ii) between the Cu $2p_{3/2}$ core level and the VBM of a bulk Cu_2O film, and (iii) between the Zn $2p_{3/2}$ and the Cu $2p_{3/2}$ core levels at the heterojunction interface, respectively. *Page 104*

Figure 5.16 Schematic of the flat-band diagrams at the heterojunction interfaces determined from the XPS measurements. For simplicity, the Cu_2O - ZnO and Cu_2O - $\text{Mg}_{0.1}\text{Zn}_{0.9}\text{O}$ interfaces are drawn with Cu_2O in the middle. *Page 105*

Figure 5.17 Energy-band diagrams for a p-n heterojunction with type II band alignment under forward bias V , where V is set to V_{bi} , the upper limit of V_{OC} . *Page 107*

Figure 5.18 Equivalent circuit of the solar cell, where I_{ph} , I_d and I_{sh} are photogenerated current, dark current and shunt current, respectively. *Page 108*

Figure 5.19 (a) Schematic image of the interface between Cu_2O and ZnO , showing a relatively big junction area; (b) Schematic image of the interface between Cu_2O and $\text{Mg}_{0.1}\text{Zn}_{0.9}\text{O}$, showing a relatively small junction area. *Page 109*

Chapter 1 Introduction

1.1 Motivation

By the end of 2008, total world energy consumption was approximately 15TW and that value is still keeping a strong increase in recent years due to the rapid development of some developing countries such as China and India. It is assumed that the world energy consumption will increase by about 70% between 2000 and 2030 ^[1]. The energy reserves of fossil fuels on earth, accounting 80% of the all energy consumed worldwide, will be used up in the next 200 years. The growing demand for energy, combined with the depletion of fossil resources, global warming and its associated climate change, has taken over as a main driving force in promoting alternative energy sources, in particular, photovoltaic (PV) solar energy.

Solar PVs are a promising large-scale supply option to reduce the world's dependency on current fossil-fuel-based electricity generation for a low-carbon future. The high-cost manufacture and concomitant pollution during manufacturing of crystalline silicon-based PV modules, dominant technologies in current PV market, however, make such great promise economically as well as ecologically unrealistic. Lots of alternative PV technologies with low-cost, ecologically-beneficial materials and fabrications, such as organic-organic, organic-inorganic hybrid, dye-sensitized solar cells (DSSCs) and some inorganic thin-film heterojunction solar cells, have been being greatly developed. ZnO, as a low-cost, nontoxic wide-bandgap semiconductor with easy synthesis of various low dimensional structures, is being widely used in such cost-effective PV cells. DSSCs built from ZnO nanoparticles showed the second highest efficiency after TiO₂-based one ^[2], and

lots of DSSCs fabricated on ZnO nanostructures have been demonstrated [3, 4, 5]. ZnO nanoparticles and nanostructures were also used in organic-inorganic hybrid solar cells, showing decent solar conversion efficiency [6, 7, 8]. Besides that, ZnO has been experimentally confirmed to be a good candidate for forming high quality heterojunction solar cells with p-type Cu_2O [9, 10]. It was also used as a conducting transparent window layer in chalcopyrite thin film solar cells to collect and transport the electrons [11].

ZnO can be alloyed with MgO to form the ternary $\text{Mg}_x\text{Zn}_{1-x}\text{O}$, tuning the energy bandgap value from 3.3 eV (ZnO) to 7.8 eV (MgO). Just because of such tunability of the energy bandgap, $\text{Mg}_x\text{Zn}_{1-x}\text{O}$ has been used in several types of solar PVs to modify the band offset between “n-type” and “p-type” semiconductors and thus improves the solar performance of those cells. It was reported that $\text{Mg}_x\text{Zn}_{1-x}\text{O}$, used as a window layer in the $\text{Cu}(\text{In}, \text{Ga})\text{Se}_2$ (CIGS) solar cells, could tune the conduction band offset for improved device performance [12, 13]. It has also been found that $\text{Mg}_x\text{Zn}_{1-x}\text{O}$ could be used in the poly(3-hexylthiophene) (P3HT)- $\text{Mg}_x\text{Zn}_{1-x}\text{O}$ hybrid solar cells for enhanced open circuit voltage V_{OC} [14].

In terms of charge generation mechanism, current existing solar cells can be classified into two distinct categories: conventional solar cells and excitonic solar cells (XSCs) [15]. A fundamental difference between these two PV cells is easily recognized: light absorption results in the formation of excitons in organic materials rather than the free electron-hole pairs directly generated in the inorganic semiconductors. The exciton, considered to be a bounded electron-hole pair, in the organic semiconductor, usually doesn't possess enough energy to dissociate in the bulk except at the interface, where the band offset between n and p-semiconductor provides an exothermic pathway for dissociation of excitons. Therefore

the heterointerface area in the XSCs directly determines how much photocurrent can be generated. By contrast, the free electron-hole pairs generated in inorganic semiconductors are easily separated by the bandgap but meanwhile easily recombine except at the p-n junction area (space charge region), where the built-in potential separate them into electron donor (p) and acceptor (n), respectively. Since the carrier separation occurs throughout the interface and interface defects or dislocations could serve as recombination centers contributing on photogeneration loss, sharp interface with good contact is preferred in the conventional solar cells. With regard to above concepts, the surface morphology of $\text{Mg}_x\text{Zn}_{1-x}\text{O}$ film needs to be well controlled as it is used for various types of solar cells. One-dimensional (1-D) single crystalline nanostructures such as nanometer-scale tips, rods, and wires are preferred in the XSCs, in which the nanostructured 1-D architecture provides a larger interface area (i.e. charge generation area) and faster electron transport path, leading to a higher solar conversion efficiency ^[6]. On the other hand, two-dimensional (2-D) film with smooth surface is needed in the conventional inorganic p-n junction solar cells since the rough film surface results in large interface area and hence high recombination probabilities.

Various deposition techniques, such as pulsed laser deposition (PLD) ^[16], molecular beam epitaxy (MBE) ^[17], sputtering ^[18], metalorganic chemical vapor deposition (MOCVD) ^[19], sol-gel ^[20], and electrophoresis deposition ^[21] have been used for the growth of $\text{Mg}_x\text{Zn}_{1-x}\text{O}$ films. Among them, MOCVD is an attractive technique because of its ability to realize various in-situ doping, large-area uniform deposition and high growth rate. Much work has been done on single crystalline $\text{Mg}_x\text{Zn}_{1-x}\text{O}$ epitaxial films grown by MOCVD ^[19, 22]. But the study on MOCVD growth of polycrystalline $\text{Mg}_x\text{Zn}_{1-x}\text{O}$ films or

nanostructures for photovoltaic applications is still few^[23]. Much more efforts should be put on such research topics especially for photovoltaic applications, in which high quality epitaxial films are not applicable because of the limitations from substrates and on the other hand, low-temperature processing and cost-effective fabrication for polycrystalline films or nanostructures are preferred.

1.2 Objectives

In this dissertation, we investigate the growth of $\text{Mg}_x\text{Zn}_{1-x}\text{O}$ films and nanostructures by using the MOCVD technique, and explore their applications in organic-inorganic solar cells and Cu_2O - $\text{Mg}_x\text{Zn}_{1-x}\text{O}$ heterojunction solar cells.

For the $\text{Mg}_x\text{Zn}_{1-x}\text{O}$ polycrystalline films growth, a dense and smooth film is expected for its applications in inorganic p-n junction solar cells. Ga-doped ZnO (GZO) films, transparent conductive electrodes, are chosen as the substrates. In order to control the surface morphology of $\text{Mg}_x\text{Zn}_{1-x}\text{O}$ films grown on GZO films, we use a low-temperature ZnO buffer layer and meanwhile investigate the buffer layer effects on film surface morphology, texturing and surface roughness. The growth of GZO films is also needed to be optimized. Both electrical and morphological properties of GZO films are optimized. For the $\text{Mg}_x\text{Zn}_{1-x}\text{O}$ nanostructures growth, it is still a challenge to achieve good wurtzite $\text{Mg}_x\text{Zn}_{1-x}\text{O}$ nanostructures with high Mg composition ($x > 10\%$). We optimize the growth of 1-D $\text{Mg}_x\text{Zn}_{1-x}\text{O}$ ($0 \leq x \leq 0.15$) nanostructures on Si substrates first and then on GZO substrates. Since the nucleation layer plays important roles on the development of nanostructures, we investigate the effect of buffer layers on the nanostructures growth.

After the optimization of MOCVD growth, we fabricate $\text{Mg}_x\text{Zn}_{1-x}\text{O}$ -P3HT hybrid solar cells and $\text{Mg}_x\text{Zn}_{1-x}\text{O}$ - Cu_2O heterojunction solar cells by using $\text{Mg}_x\text{Zn}_{1-x}\text{O}$ nanostructures and films. Enhanced solar conversion efficiency with other improved parameters including open-circuit voltage (V_{OC}), short-circuit current (I_{SC}), fill factor (FF), shunt resistance (R_{sh}) etc. are expected by using $\text{Mg}_x\text{Zn}_{1-x}\text{O}$ instead of ZnO and moreover by controlling surface morphology of $\text{Mg}_x\text{Zn}_{1-x}\text{O}$ layers. We investigate not only the effects of Mg composition but also the influence of surface morphology of $\text{Mg}_x\text{Zn}_{1-x}\text{O}$ layers on the solar cell performance.

In summary, the objectives of this research are (i) Growth optimization of polycrystalline $\text{Mg}_x\text{Zn}_{1-x}\text{O}$ films on transparent conductive electrodes to achieve dense and smooth 2-D films; (ii) Growth optimization of $\text{Mg}_x\text{Zn}_{1-x}\text{O}$ 1-D nanostructures on transparent conductive electrodes to achieve enough high Mg composition and good nanostructures; (iii) Demonstration of $\text{Mg}_x\text{Zn}_{1-x}\text{O}$ -polymer hybrid solar cells and $\text{Mg}_x\text{Zn}_{1-x}\text{O}$ - Cu_2O heterojunction thin film solar cells and trying to achieve enhanced solar performance by controlling Mg composition and surface morphology of $\text{Mg}_x\text{Zn}_{1-x}\text{O}$ layers.

1.3 Dissertation Organization

The research motivation and objectives of this dissertation is given in Chapter 1. Chapter 2 presents a technical background for this dissertation, which includes fundamental properties of $\text{Mg}_x\text{Zn}_{1-x}\text{O}$, growth technologies for $\text{Mg}_x\text{Zn}_{1-x}\text{O}$ polycrystalline films and nanostructures and an introduction of Rutgers MOCVD system. In Chapter 3, growth optimization of GZO films and $\text{Mg}_x\text{Zn}_{1-x}\text{O}$ polycrystalline films grown on GZO films is discussed in details. Growth optimization of $\text{Mg}_x\text{Zn}_{1-x}\text{O}$ nanostructures is

presented in Chapter 4, which includes the growth optimization on Si substrates and on GZO films. In Chapter 5, photovoltaic cells fabricated on $\text{Mg}_x\text{Zn}_{1-x}\text{O}$ polycrystalline films and nanostructures are demonstrated. Two different kinds of solar cells, $\text{Mg}_x\text{Zn}_{1-x}\text{O}$ -P3HT hybrid solar cell and $\text{Mg}_x\text{Zn}_{1-x}\text{O}$ - Cu_2O heterojunction solar cell, are discussed respectively. Finally, conclusions and suggestions for future work are given in Chapter 6.

Chapter 2 Technical Background

2.1 Fundamental Properties of $\text{Mg}_x\text{Zn}_{1-x}\text{O}$ Alloy and Its Applications

ZnO is a wide-bandgap semiconductor belongs to the II-VI semiconductor group. It crystalizes in two main forms: hexagonal wurtzite and cubic zincblende. At a relatively high pressure about 10GPa, it also crystalizes in the cubic rocksalt structure. The most stable at ambient conditions and thus most common structure of ZnO is wurzite hexagonal structure, which belongs to the space group of $P6_3mc$. Fig. 2.1 shows the wurtzite crystal structure of ZnO and its projection along the $[11\bar{2}0]$ direction. Such ZnO structure can be described as the alternatively stacking of hexagonal close packed (hcp) zinc and oxygen ionic layers along the c-axis, i.e. $[0001]$ direction. In terms of the atom positions in the hcp lattice, the O and Zn layers can be classified as A&B and a&b, respectively, as shown in Fig. 2.1(b). The stacking sequence of ZnO wurtzite structure can be considered as $\cdots \text{.AaBbAaBb....}$ as compared to $\text{....AaBbCcAaBbCc....}$ in diamond cubic (silicon) and sphalerite (GaAs etc.). The lattice parameters of ZnO are $a = 3.24982 \text{ \AA}$ and $c = 5.20661 \text{ \AA}$. The ratio of lattice parameter c/a is 1.602, which is slightly less than the value of 1.633 for an ideal hcp structure. The Zn–O bond length is 1.992 \AA parallel to the c-axis and 1.973 \AA in all the other three directions of the tetrahedral arrangement of nearest neighbors. In the unit cell, O^{2-} ions (by convention) occupy $(0, 0, 0)$ and $(0.6667, 0.3333, 0.5)$ positions, Zn^{2+} ions occupy $(0, 0, 0.3825)$ and $(0.6667, 0.3333, 0.8825)$ positions.

The hexagonal wurtzite ZnO has a point group $6mm$ or C_{6v} , which has no inversion symmetry, resulting in piezoelectricity and pyroelectricity of ZnO. The alternating positively charged Zn-terminated (0001) planes and negatively charged O-terminated $(000\bar{1})$ planes create a normal dipole moment and spontaneous polarization along the c-axis, resulting in divergence in surface energy. The polar (0001) plane, with no reconstruction or passivation, should have the maximum surface energy amongst the low-index planes, which therefore leads to a big growth rate along [0001] direction. This is in fact observed under most conditions during vapor phase growth. Crystals grown via the vapor phase usually are needle shaped with a hexagonal cross-section. The crystals are elongated in the [0001] direction and the prismatic sides of the crystals are usually the $\{10\bar{1}0\}$ or $\{11\bar{2}0\}$ planes, which implies that the (0001) plane has the highest energy and as a result, the growth rate along the c-direction is the highest. Thus, it is very easy to obtain c-axis oriented films on almost any substrate, even under non-epitaxial conditions.

MgO, usually used as an insulator with a big bandgap of 7.8 eV, can be alloyed with ZnO, forming $Mg_xZn_{1-x}O$, which has been reported as a promising II-VI semiconductor because of its tunable bandgap^[16]. MgO has a stable rocksalt structure as shown in figure 2.2, which belongs to the space group $Fm\bar{3}m$ with the lattice parameter of $a=4.215\text{\AA}$ and the Mg–O distance of 2.1075\AA . Unlike ZnO that is tetrahedrally bonded and has a 4-fold coordination, MgO is octahedrally bonded having a 6-fold. The lattice consists of interpenetrating face centered cubic lattices, separated along the c-axis by $u=0.5$ (fractional coordinates). While oxygen (by convention) occupies the (0,0,0) and (0.5,0.5,0) positions, magnesium occupies the (0,0,0.5) and (0.5,0.5,0.5) positions^[24].

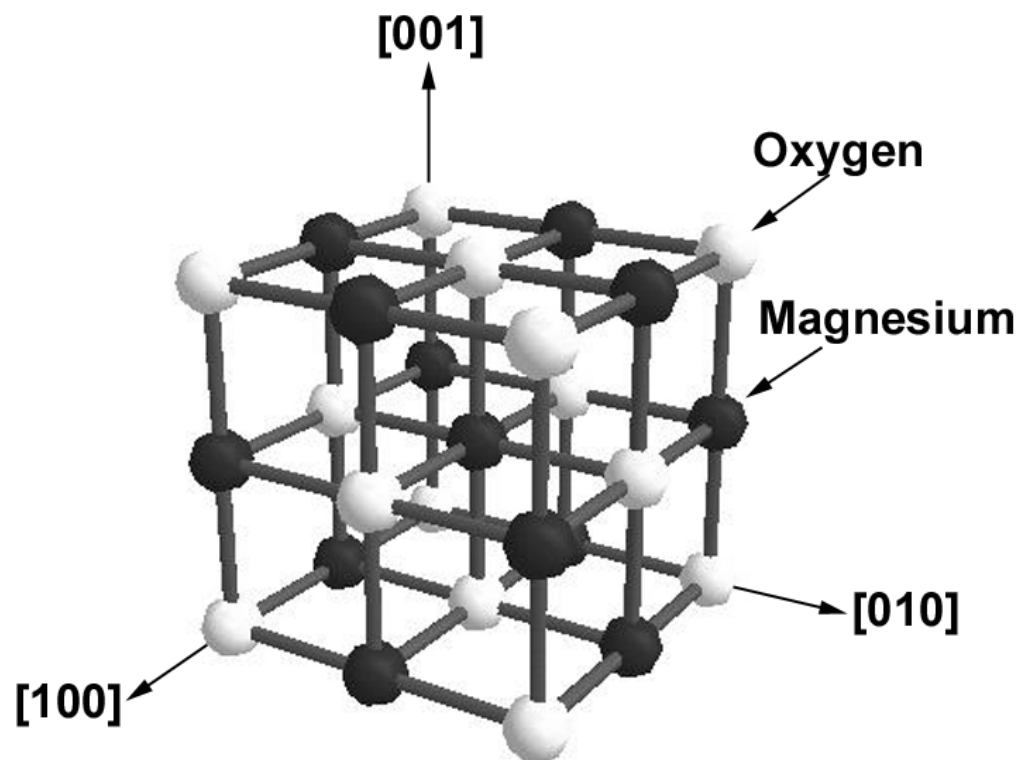


Figure 2.2 Crystal structure of rocksalt MgO (Cubic).

As the big difference of crystal structure, symmetry, ionic bonding distance and energy between ZnO and MgO is seen, the possibility to grow related $\text{Mg}_x\text{Zn}_{1-x}\text{O}$ crystals with a wurtzite structure is far from obvious. A slight distortion in the lattice can destroy the symmetry in the crystal and multi-phases with both wurtzite and rocksalt symmetry are easily produced. The equilibrium thermodynamic phase diagram of the MgO-ZnO system is given in Fig. 2.3 [25]. Seen from that figure, the thermodynamic solid solubility of MgO in ZnO is only ~5% and there is a big mixed-phases region, which limits the band gap engineering applications.

A decade ago, A. Ohtomo et al [16, 26] found that it was possible to grow these alloyed films with the wurtzite structure over a certain range of concentrations. Through using a non-equilibrium film-growth method, pulsed laser deposition (PLD), they found the solubility of MgO in ZnO could reach to 33% in $\text{Mg}_x\text{Zn}_{1-x}\text{O}$ epitaxial films, which led to a bandgap of ~ 4.0 eV for wurtzite $\text{Mg}_x\text{Zn}_{1-x}\text{O}$. And meanwhile, they reported that the epitaxial films having Mg up to $x=0.15$ were thermodynamically stable up to about 700°C [27]. One reason for the high Mg incorporation could be due to the accommodation of strain in the films at the interface between the epilayer and substrate. Soon later, W. Yang et al. [28] grew multicomposition $\text{Mg}_x\text{Zn}_{1-x}\text{O}$ films with Mg content x varying continuously from 0 to 1 on a single substrate (c-plane sapphire) by PLD and drew the bandgap energy of $\text{Mg}_x\text{Zn}_{1-x}\text{O}$ as a function of x , shown in Fig. 2.4. From that, the mixed-phases region was narrowed in $0.37 \leq x \leq 0.62$. This mixed-phases region was reported to disappear in the $\text{Mg}_x\text{Zn}_{1-x}\text{O}$ films grown by S. Fujita et al. [29] During their growth, a-plane sapphire substrates with a ZnO buffer were used and the solubility of MgO in wurtzite ZnO went up to 50%, after which a cubic $\text{Mg}_x\text{Zn}_{1-x}\text{O}$ phase was formed.

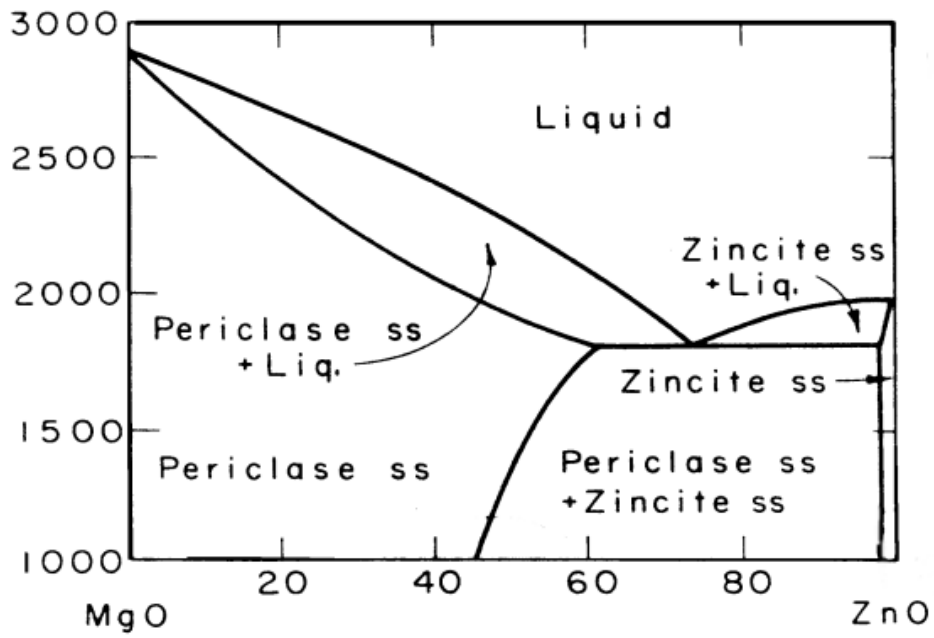
MgO-ZnO

Figure 2.3 Equilibrium phase diagram of the MgO-ZnO system ^[25].

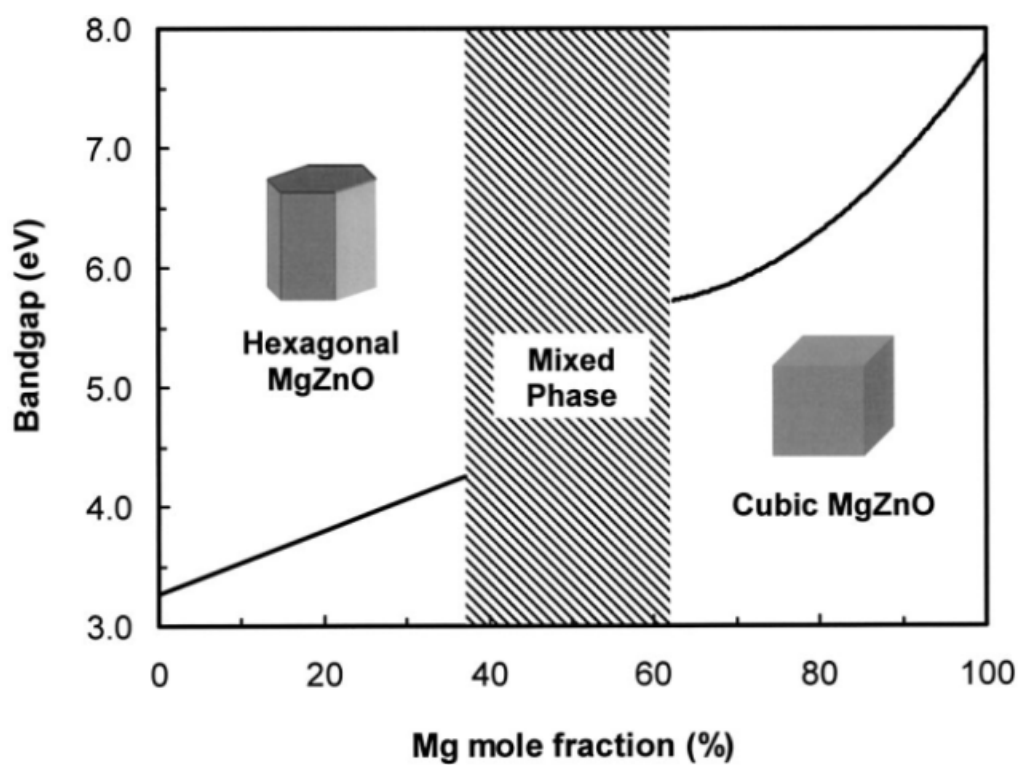


Figure 2.4 Band-gap energy as a function of Mg content in $\text{Mg}_x\text{Zn}_{1-x}\text{O}$ films ^[28].

$\text{Mg}_x\text{Zn}_{1-x}\text{O}$ has been investigated for various electronic and optoelectronic devices since it was first reported as a promising II-VI semiconductor by A. Ohtomo^[16]. With tunable bandgap values and similar lattice constants to ZnO, $\text{Mg}_x\text{Zn}_{1-x}\text{O}$ was used as a barrier layer in MgZnO/ZnO heterojunctions^[27, 30, 31, 32], superlattices^[26, 33, 34] and quantum wells^[35, 36, 37, 38, 39], showing big potential on short-wavelength optoelectronic applications such as light emitting diodes (LED) or laser diodes (LD). Besides that, $\text{Mg}_x\text{Zn}_{1-x}\text{O}/\text{ZnO}$ heterostructures were also investigated by some researchers for high electron mobility transistors (HEMTs) since the 2-D electron gas formed by the polarization effect provide very high electron mobility. Related reviews on those kinds of heterostructures can be found in references^[40, 41, 42]. $\text{Mg}_x\text{Zn}_{1-x}\text{O}$ (wurtzite structure) is also a piezoelectric material with similar lattice structure and symmetry to ZnO, which can be used in the surface acoustic wave (SAW) and bulk acoustic wave (BAW) devices. Moreover, it allows for flexibility in thin film SAW device design, as its piezoelectric properties can be tailored by controlling the Mg composition, as well as by using MgZnO/ZnO multilayer structures^[43, 44]. As a promising photovoltaic material, wurtzite $\text{Mg}_x\text{Zn}_{1-x}\text{O}$ can also be used in the solar cells. D. C. Olson et al. proposed a band-offset engineering approach for enhanced open-circuit voltage (V_{OC}) in polymer-oxide hybrid solar cells^[14]. In that research, $\text{Mg}_x\text{Zn}_{1-x}\text{O}$ was found to decrease the conduction band offset between P3HT and $\text{Mg}_x\text{Zn}_{1-x}\text{O}$ and thus increase the theoretical V_{OC} . Besides that, many researchers investigated the band offset effect on V_{OC} of heterojunction $\text{CuIn}_{1-x}\text{Ga}_x\text{Se}_2$ solar cells using $\text{Mg}_x\text{Zn}_{1-x}\text{O}$ instead of ZnO^[12, 13]. Polycrystalline $\text{Mg}_x\text{Zn}_{1-x}\text{O}$ films used as an active layer in a thin-film transistor (TFT) was reported recently, where Mg substitution was believed to increase the activation energy for

defect-related donor states by increasing the band gap and thus reduce the carrier density in the ZnO channel layer ^[45]. And moreover, $\text{Mg}_x\text{Zn}_{1-x}\text{O}$ alloy could enlarge the band tail states by increasing E_g of ZnO and improve the stability of TFT performance under visible light ^[46]. Our newest result also showed that substitution of Mg into ZnO suppressed the oxygen vacancies in the TFT channel, improving the field effect mobility, subthreshold swing and thermal stability of the device ^[47]. As $\text{Mg}_x\text{Zn}_{1-x}\text{O}$ (E_g can be tuned from 3.3 eV to 7.8 eV) has a very wide range of sensing spectra from UV-A (320-400 nm) to UV-C (200-280 nm) regions, it has been considered as a promising candidate semiconductor in the metal-semiconductor-metal (MSM) structured ultraviolet (UV) photodetectors ^[48] and many researchers are putting their focus on the cubic-phase $\text{Mg}_x\text{Zn}_{1-x}\text{O}$ films and the UV detectors based on them ^[28, 49, 50]. $\text{Mg}_x\text{Zn}_{1-x}\text{O}$ was also found to exhibit resistive switching characteristic and two simple devices based on Pt/ $\text{Mg}_{0.2}\text{Zn}_{0.8}\text{O}$ /Pt and Pt/spinel- $\text{Mg}_x\text{Zn}_{1-x}\text{O}$ ($x > 0.6$)/Pt have been reported for the nonvolatile memory applications ^[51, 52]. One-dimension (1-D) nanostructured $\text{Mg}_x\text{Zn}_{1-x}\text{O}$ is particularly promising for the field emission applications, showing excellent emission behavior with extremely improved brightness, ~ 80 times higher current density than that of the ZnO nanowires grown under the same conditions ^[53]. Besides that, many efforts have been put to prepare the p-type $\text{Mg}_x\text{Zn}_{1-x}\text{O}$ using N, P or N-Al doping ^[54, 55, 56] and then make p-n heterojunction with ZnO for photodiodes ^[57].

2.2 Growth Technologies of $\text{Mg}_x\text{Zn}_{1-x}\text{O}$ Polycrystalline Films

In terms of the crystallinity and surface morphology, $\text{Mg}_x\text{Zn}_{1-x}\text{O}$ low dimensional layers (thin films) can be divided into 3 types, which are epitaxial films, polycrystalline

films and nanostructures. Each type of thin film is needed for certain applications. For instance, MgZnO/ZnO superlattices or quantum wells need good MgZnO epi-films with excellent surface flatness, crystallinity and electron mobility, while some transistors-based applications with particular low temperature processing need polycrystalline MgZnO films grown at a relatively low T but with well-controlled electrical properties. Good SAW devices need the piezoelectric MgZnO films to have a smooth surface, perfect c -axis texture and high resistivity, while some polarization sensitive devices, such as an optically addressed high-contrast UV light modulator, need the in-plane optical anisotropy in the film and hence the non-polar epi-films of MgZnO ^[58]. For photovoltaic applications, two types of thin films are needed just as what we discussed in the motivation part (chapter 1). Nanostructured MgZnO could be used in organic-inorganic hybrid and dye-sensitized solar cells for enhanced device performance. Smooth and dense film is preferred for the conventional thin film heterojunction solar cells and the best choice is epitaxial films. In the real cases, however, it is unrealistic to choose epitaxial films because of two factors (1) devices structure, most of which don't provide epitaxial substrates for epi-film growth; (2) fabrication cost, which prefers a low-temperature polycrystalline or amorphous film growth.

As discussed above, polycrystalline MgZnO film has stimulated a growing interest due to its easy fabrication, multifunctional properties and various applications. Many growth technologies have been developed for the synthesis of MgZnO polycrystalline films, including radio-frequency (RF) magnetron sputtering, sol-gel, MOCVD, chemical spray pyrolysis and electrophoretic deposition. The Mg composition, microstructure, electrical

and optical properties were intensively investigated. Each growth technology has its unique advantages for specific applications but also drawbacks.

2.2.1 RF Magnetron Sputtering

RF magnetron sputtering is a very common physical vapor deposition (PVD) technology, used widely in the semiconductor industry. It was first used to synthesis MgZnO polycrystalline films by T. Minemoto et al.^[18], who aimed to synthesis $\text{Mg}_x\text{Zn}_{1-x}\text{O}$ films with wider band gap, i.e. higher Mg composition and lower growth temperature. They utilized a co-sputtering technique, where two targets, ZnO and MgO, were simultaneously used, to deposit $\text{Mg}_x\text{Zn}_{1-x}\text{O}$ films on fused silica at room temperature (RT). The Mg contents were controlled by varying the sputtering power applied to each target to control the sputtering rate. In their results, the solid solubility of MgO in ZnO went up to 46% and beyond 62%, the MgZnO became cubic MgO-like structure. Besides that, they characterized the electrical and optical properties of films and found the $\text{Mg}_x\text{Zn}_{1-x}\text{O}$ films had the similar transmittance and resistivity to those of non-doped ZnO but with wider bandgap that was expected to serve as a useful window layer of solar cells. Their study proposed that the RF magnetron sputtering was a perfect technology for depositing polycrystalline $\text{Mg}_x\text{Zn}_{1-x}\text{O}$ films at a low substrate temperature for photovoltaic applications.

Recently, C. X. Cong et al investigated the effect of the partial pressure of sputtering gas N_2 on the Mg composition, structural and optical properties of $\text{Mg}_x\text{Zn}_{1-x}\text{O}$ polycrystalline films grown by RF magnetron sputtering^[59]. In their research, a single target, $\text{Mg}_{0.18}\text{Zn}_{0.82}\text{O}$, was used and the film was deposited on the quartz substrate at 500°C

and then annealed at 600°C. The Mg composition was tuned by changing nitrogen partial pressure ratio of sputtering gases. Their as-grown $\text{Mg}_x\text{Zn}_{1-x}\text{O}$ films were highly textured with a preferential orientation of [0001] for hexagonal wurtzite phase and [100] for cubic rocksalt phase. The solid solubility of MgO in ZnO was found to be 50% and the mixed-phases region (50%-83%) was a little large.

RF magnetron sputtering was also used to grow $\text{Mg}_x\text{Zn}_{1-x}\text{O}$ thin films on Si substrates by J. Y. Moon et al.^[60] very recently. MgO and ZnO targets were used for the co-sputtering. They grew the film at a very high temperature, ~700°C, trying to achieve epitaxial films. But the results showed that an interfacial reaction happened and Mg_2Si formed between MgZnO and Si induced the formation of polycrystalline MgZnO thin films. They, therefore, applied a low-T (450°C) ZnO buffer layer on the Si substrate to improve the epitaxial relationships between MgZnO and Si. And it was found that that ZnO buffer reduced the formation of Mg_2Si and an epitaxial growth was resulted in. The $\text{Mg}_x\text{Zn}_{1-x}\text{O}$ film was characterized by the photoluminescence (PL), from which the Mg composition was estimated to be ~2%.

2.2.2 Sol-Gel

The sol-gel process is a wet-chemical technique usually used for the synthesis of amorphous or polycrystalline films. It has some advantages such as simplicity of fabrication, low-cost, high deposition rate, large-area uniform deposition on various substrates. The early study on $\text{Mg}_x\text{Zn}_{1-x}\text{O}$ polycrystalline film growth deposited by sol-gel method was reported by D. Zhao et al.^[61]. They coated Mg and Zn precursor sols on Si (100) and quartz substrates by spinning and then annealed the sample at 100°C and 350°C

subsequentially, to get the final polycrystalline $\text{Mg}_x\text{Zn}_{1-x}\text{O}$ films. The Mg composition was adjusted by changing the Mg^{2+} concentration in the solution. The maximum Mg% they could achieve in the wurtzite film was ~36% and the bandgap of film was tunable between 3.40 and 3.93 eV. The PL properties of polycrystalline $\text{Mg}_x\text{Zn}_{1-x}\text{O}$ thin films were then reported and discussed. Z. Ji et al also deposited $\text{Mg}_x\text{Zn}_{1-x}\text{O}$ ($0 \leq x \leq 0.3$) polycrystalline films on quartz substrates by sol-gel dip coating process and then did film characterization by PL [20]. They used similar sol-gel process to previously-reported one [61] but with different preheat and anneal temperature, which were 80°C and 500°C, respectively. All films show a c-axis preferred orientation but with very poor crystallinity. The PL peaks of $\text{Mg}_x\text{Zn}_{1-x}\text{O}$ films in the spectra appeared to be broad with low intensity, which could be related to the poor crystallinity of films. The post-annealing effect on the Mg incorporation and band gap values of sol-gel prepared $\text{Mg}_x\text{Zn}_{1-x}\text{O}$ ($0 \leq x \leq 0.3$) thin films was investigated by S. R. Meher et al recently [62]. It was found that bandgap values of $\text{Mg}_x\text{Zn}_{1-x}\text{O}$ films made by sol-gel had a dependency on the post-annealing temperature and there existed a certain critical annealing temperature, up to which the bandgap increased with increasing annealing T and decreased thereafter. The critical annealing temperature for the $\text{Mg}_x\text{Zn}_{1-x}\text{O}$ with $x=0.3$ was found to be lower than that of films with lower x. The reason was attributed to the poor bonding of Mg atoms in the alloy film at higher Mg concentration. Very recently, B. K. Sonawane et al deposited $\text{Mg}_x\text{Zn}_{1-x}\text{O}$ ($0.05 \leq x \leq 0.33$) films on Si substrate by the sol-gel spin coating method and studied the refractive index and stress of MgZnO films [63]. They succeeded in tailoring refractive index of MgZnO films from 1.44 to 1.11 to provide optical confinement in the waveguides. The stress of $\text{Mg}_x\text{Zn}_{1-x}\text{O}$ polycrystalline

films on Si was also estimated and the compressive stress value didn't change too much for x increasing from 0.05 to 0.30.

2.2.3 MOCVD

MOCVD is an attractive film growth technique because of its ability to realize various in-situ doping, well control of composition, large-area uniform deposition and high growth rate. Compared to the sputtering technology, it is also a damage-free process because there is no high-energy species in the vapor phase. Besides that, it can be used to grow different types of film including single-crystalline epitaxial films and nanostructures, polycrystalline and amorphous films. Since much work about the MOCVD growth of $\text{Mg}_x\text{Zn}_{1-x}\text{O}$ epitaxial film was done already on c-sapphire^[22] and r-sapphire^[19] substrates, however, the growth of polycrystalline $\text{Mg}_x\text{Zn}_{1-x}\text{O}$ films by MOCVD has not been well investigated. For the first time, wurtzite-type MgZnO films with the controllable bandgap energies from 3.3 to 3.72 eV were successfully grown on the fused silica substrates by MOCVD in A. Yamada's group^[23]. The effect of the growth temperature and $\text{Mg}/(\text{Mg}+\text{Zn})$ molar flow rate ratio of precursors on the crystalline structure of film was investigated. The growth temperature was modulated from 115°C and 215°C and the molar flow ratio of $\text{Mg}/(\text{Mg}+\text{Zn})$ was varied in the range of (0.68-0.91). The results showed that wurtzite structure preferred a high T and low $\text{Mg}/(\text{Mg}+\text{Zn})$ ratio. At a growth temperature of 145°C and a $\text{Mg}/(\text{Mg}+\text{Zn})$ ratio of 0.86, they got the $\text{Mg}_x\text{Zn}_{1-x}\text{O}$ film with a Mg content of 23% and a bandgap of 3.73 eV^[64]. The wurtzite MgZnO polycrystalline film had good optical properties and comparable resistivity to that of ZnO film, which indicated that MgZnO film was superior to CdS or ZnO film as buffer and window layers in the CIGS

solar cells. They also fabricated the CIGS solar cell with MgZnO as the window layer and obtained the efficiency of 10.24%.

2.2.4 Chemical Spray Pyrolysis

Chemical spray pyrolysis is another attractive film deposition technology that possesses ability to grow large-area films with good uniformity and low cost. Polycrystalline $\text{Mg}_x\text{Zn}_{1-x}\text{O}$ ($x < 0.20$) films were first grown by chemical spray pyrolysis in 2002 ^[65]. T. Terasako et al chose a-plane sapphire (11-20) as the substrate and deposit MgZnO film at a substrate temperature of $\sim 400^\circ\text{C}$. All $\text{Mg}_x\text{Zn}_{1-x}\text{O}$ ($x < 0.20$) films were highly textured with a preferential orientation along c-axis. They also grew MgZnO films on Si(100) substrate but didn't obtain the c-axis preferred orientation. The $\text{Mg}_x\text{Zn}_{1-x}\text{O}$ films grown on a-sapphire showed the unstructured near-band-edge (NBE) emission, shifting continuously towards higher energy with the increase of x . They attributed the NBE emission to the radiative transitions from tail states of the conduction band to those of the valence band. X. Zhang et al ^[66] used a similar technique but with a different name, called the ultrasonic spray pyrolysis deposition, to synthesize $\text{Mg}_x\text{Zn}_{1-x}\text{O}$ films. A Si (100) substrate was used and the substrate temperature was set at 400°C during the growth. All films appear to be polycrystalline with a wurtzite structure. The maximum Mg composition they obtained was $\sim 27\%$, corresponding to a bandgap of ~ 3.58 eV.

2.2.5 Electrophoretic Deposition

Electrophoretic deposition (EPD) is a process industrially used for applying coatings to metal fabricated products or other electrically conductive surfaces. A characteristic feature

of this process is that colloidal particles suspended in a liquid medium migrate under the influence of an electric field (i.e. electrophoresis) and are deposited onto an electrode. The research focused on the $\text{Mg}_x\text{Zn}_{1-x}\text{O}$ films deposited by EPD is not too much. Y. Jin et al.^[21] fabricated $\text{Mg}_x\text{Zn}_{1-x}\text{O}$ films from high purity ZnO nanocrystalline powder by EPD on conductive glass substrates (FTO/glass). The annealing temperature was set at 450°C. The film showed polycrystalline structure with a more preferential crystalline orientation than the ZnO powder. But the film morphology didn't look good. The film (2 - 3 μm) looked non-uniform with a very rough surface. From the PL measurement, the Mg incorporation was less than 5%.

In summary, $\text{Mg}_x\text{Zn}_{1-x}\text{O}$ polycrystalline films can be deposited by many technologies. Each of them has its advantages but also disadvantages, as listed in Table 2.1. RF magnetron sputtering and MOCVD provide the ability of processing at low substrate temperature, which is particularly attractive for the photovoltaic applications. In comparison with RF magnetron sputtering, MOCVD is more advantageous because of its damage-free process. Moreover, MOCVD has advantages on in-situ doping, morphology control and large-area uniformly deposition. Compared to sputtering and MOCVD methods, the chemical solutions related synthesis technologies, such as sol-gel, chemical spray pyrolysis, and electrophoretic deposition, are more attractive due to their easy and low-cost fabrication. But usually a relatively high temperature (400-500°C) post annealing process is needed in those technologies. The doping level, film morphology and microstructure are not easily controlled, which generally are critical factors influencing the overall efficiency of the solar cells.

Table 2.1 Comparison of growth technologies for $\text{Mg}_x\text{Zn}_{1-x}\text{O}$ polycrystalline films

	Advantages	Disadvantages
RF Magnetron Sputtering	Provide ability of processing at Low T_s .	Ionic bombardment damage; Introducing impurities; High vacuum; Target is needed.
MOCVD	In-situ doping; Morphology control; Large-area uniform deposition; Damage-free process	Specific precursors (expensive, toxic); Expensive equipment.
Sol-Gel	Simple process; Low-cost equipment; Low-cost raw materials.	A post annealing process is needed, usually at a relatively high T ; Doping level, morphology and microstructure are not easily controlled.
Chemical Spray Pyrolysis		
Electrophoresis Deposition		

2.3 Growth Technologies of $\text{Mg}_x\text{Zn}_{1-x}\text{O}$ Nanostructures

To date, most of growth study of $\text{Mg}_x\text{Zn}_{1-x}\text{O}$ has been focused on epitaxial thin films and only little reported work discussed $\text{Mg}_x\text{Zn}_{1-x}\text{O}$ nanostructures. The main challenge is coming from the synthesis difficulties. As we known, the formation of various 1-D ZnO nanostructures is usually attributed to the polarity of ZnO along $\langle 0001 \rangle$ directions, which leads to a high surface energy on $\{0001\}$ planes and hence a fast growth rate along c-axis^[67]. With the Mg incorporation into ZnO, however, this polarity is weakened and the anisotropy of surface energy among all ZnO planes is reduced^[68]. The growth rate along a- and b-axis starts to increase, while that along c-axis is decreasing. And moreover, this trend increases with increasing Mg incorporation. As a result, the growth habit along one direction is broken and the formation of 1-D nanostructure is becoming more and more difficult with the increase of Mg content. So far, the maximum Mg composition in reported 1-D $\text{Mg}_x\text{Zn}_{1-x}\text{O}$ nanostructure is limited to $\sim 18\%$ ^[69]. In the following, we will review the current work and efforts that have been put on the synthesis of $\text{Mg}_x\text{Zn}_{1-x}\text{O}$ nanostructures.

2.3.1 MOCVD

As we discussed above, MOCVD has many advantages such as controllable in-situ doping, available large-area uniformly deposition, high growth rate and so on. One of the most attractive advantages is its ability on growing almost all types of low-dimensional layers including epitaxial, amorphous, polycrystalline films and nanostructures. So far, MOCVD is the most widely used technology for the $\text{Mg}_x\text{Zn}_{1-x}\text{O}$ nanostructures growth. The reported maximum Mg content of $\text{Mg}_x\text{Zn}_{1-x}\text{O}$ nanostructures, around 18%, is reached by this technology.

In MOCVD growth of $\text{Mg}_x\text{Zn}_{1-x}\text{O}$ nanostructures, several growth factors are critical, which are substrate temperature, buffer layers, metal-organic sources (i.e. precursors), growth pressure and flow rates of reactive species. The latter two factors, i.e. the growth pressure and flow rates of reactive species, determine the flow pattern and growth rate of films, and hence influence the growth mechanism. But they are system structure-based factors and could shift too much from one system to another. Therefore, the most focus will be put on the former 3 factors. The substrate temperature, one of the most critical factors in growth kinetics, determines the nucleation behavior and structure development. For the growth of $\text{Mg}_x\text{Zn}_{1-x}\text{O}$ nanostructures, most researchers set the substrate temperature to be around 500°C [70, 71, 72] or higher (600°C) [69], which is a little bit higher than the ZnO nanostructures growth [73]. Besides the substrate temperature, the nucleation behavior is also influenced by the substrate surface conditions such as surface energy, crystallographic orientation, atomic bonding, defects, roughness, and so on, which usually depends on the substrate itself. But as the surface conditions are not expected, film growers can modify them by using a buffer layer. People also choose a buffer layer to reduce the lattice and thermal mismatch between epilayers and substrates. In almost all MOCVD-grown $\text{Mg}_x\text{Zn}_{1-x}\text{O}$ nanostructures reported so far, buffers are seldom used except J. Yoo et al's work [69], where a low T MgZnO buffer layer was used. The growth mechanism is still unclear. The big lattice mismatch between $\text{Mg}_x\text{Zn}_{1-x}\text{O}$ and substrate (Si or SiO_2/Si in almost all cases) and surface energy anisotropy of $\text{Mg}_x\text{Zn}_{1-x}\text{O}$ lattice could probably determine the formation of $\text{Mg}_x\text{Zn}_{1-x}\text{O}$ nanostructures directly on the substrate without using a buffer. But D. C. Kim et al [53, 74] found that surface phase separation happened during the initial growth at high T and $\text{Mg}_x\text{Zn}_{1-x}\text{O}$ nanowires only grew on the Zn-rich

region. The choice of the precursor chemicals is also very important in MOCVD growth, which strongly influences the reaction pathways although how to influence is not clearly understood yet. The growth of $\text{Mg}_x\text{Zn}_{1-x}\text{O}$ nanostructure needs two metalorganic sources, i.e. precursors of Zn and Mg. If both precursors have too much different molecular mass and hence different diffusion coefficient, and too much different decomposition and reaction rate at a fixed substrate temperature, at least one will tend to develop a concentration gradient in the growing crystal along the direction of gas flow. The alloy composition gradients are easily formed. To eliminate it, it is desirable to select precursors with similar masses and diffusion coefficient. Diethylzinc (DEZn) and bis-cyclopentadienylmagnesium (Cp_2Mg) are usually used as Zn and Mg precursors, respectively. The formula weight for them is similar, which is 123.49 for DEZn and 154.49 for Cp_2Mg . Besides that, C. H. Ku et al.^[70] chose Zinc acetylacetonate ($\text{Zn}(\text{C}_5\text{H}_7\text{O}_2)_2$) and Magnesium acetylacetonate ($\text{Mg}(\text{C}_5\text{H}_7\text{O}_2)_2$) as Zn and Mg precursors, respectively. By using those two sources, they obtained a maximum Mg composition of ~16.5%. J. R. Wang et al.^[71] used DEZn as Zn precursor, but chose the $[\text{Mg}(\text{H}_2\text{O})_6](\text{NO}_3)_2$ solution as the Mg source and oxidizer. They first deposited a $[\text{Mg}(\text{H}_2\text{O})_6](\text{NO}_3)_2$ layer on the substrate, Si (111) wafer, and then loaded it into MOCVD chamber for ZnO growth. Since the Mg atom was firstly deposited and got incorporation into the ZnO nanostructures through diffusion, the Mg composition in this case was not very high, <6%.

2.3.2 Thermal evaporation

Thermal evaporation is a very simple method for synthesizing $\text{Mg}_x\text{Zn}_{1-x}\text{O}$ nanostructures. In this method, source materials (pure Zn and Mg powders) were loaded

into a horizontal tube furnace heated at a high temperature, usually 700-800°C and then the carrier (Ar or N₂) and reactive gas (O₂) were flowed through to carry the evaporated source vapors to the substrate. The substrate was usually put downstream and at a relatively low T zone to collect the deposition. Si (100) and Si (111) wafers were usually chosen as the substrates and B. H. Kong et al ^[75] also tried to deposit Mg_xZn_{1-x}O nanostructures on c-plane sapphire by the thermal evaporation method. If no buffers were used, as-deposited Mg_xZn_{1-x}O nanostructures appeared to be dendritic nanowires ^[76, 77] or randomly-inclined nanorods ^[76]. But with designed buffers or templates, well-aligned nanorods could be obtained. L. Zhu et al ^[78] used a two-step growth process to deposit a ZnO-droplets layer first and then got MgZnO nanorods with abrupt tips on that template layer. B. H. kong et al ^[75] deposited a ZnO template and a MgZnO template on Si substrates, respectively, by sputtering. And then the vertically well-aligned MgZnO nanorods were grown on those templates. Besides ZnO-based buffer layers, Au, as a catalyst, was also used for the MgZnO nanostructures growth. Through pre-depositing Au nanoparticles with diameters in the range of 40-60 nm on Si(100) substrate, Y. Z. Zhang et al ^[79] successfully synthesized quasi-aligned Mg_xZn_{1-x}O (x=0 and 0.23) nanorods by the thermal evaporation method. They found the Au catalyst played important roles in the MgZnO nanostructures growth but the growth mechanism didn't follow the vapor-liquid-solid (VLS) process model. It is possible to tune the Mg composition by changing the molar ratio or weight ratio of Zn and Mg powders, or by varying the distance between substrates and the source materials ^[77], but it is hard to control it since the growth mechanism is unclear. The maximum Mg incorporation in Mg_xZn_{1-x}O nanostructures grown by thermal evaporation was reported to be 23% ^[79]. However, the fluctuations in alloy compositions exist.

2.3.3 Other technologies

There are still many technologies that have been tried to grow $\text{Mg}_x\text{Zn}_{1-x}\text{O}$ nanostructures, which includes catalysis driven molecular beam epitaxy (MBE) ^[80], pulsed laser deposition (PLD) ^[81], ion-beam sputtering ^[82] and thermal diffusion ^[83]. Y. W. Heo et al ^[80] reported the optical properties of MgZnO nanorods grown by catalyst driven MBE. As catalyst, a 0.2-20 nm thick Ag layer was pre-deposited on the SiO_2/Si substrate and then the nanorods growth was done at a substrate temperature of 300-500°C. From SEM results, they found the morphology of the nanorods changed with the addition of Mg, becoming more uniform compared to pure ZnO nanostructures synthesized under similar conditions. The growth mechanism was not discussed too much except that the growth of $\text{Mg}_x\text{Zn}_{1-x}\text{O}$ nanostructures was realized via nucleation on Ag films or islands. The MgZnO nanorods exhibited a strong photoluminescence response. From the shift of PL peak, the Mg composition was estimated to be 3-4%. First attempts to obtain nanostructured MgZnO using PLD was reported by M. Lorenz et al ^[81]. They chose a-plane and c-plane sapphires as substrate and Au as the catalyst. The growth temperature was controlled at 870-950°C. The distance between target and substrate was proved to be extremely important in determining the nanowire morphology. The Mg content could be controlled via the PLD gas pressure and the maximum Mg content they could achieve was 20%. They characterized the spatial homogeneity of the Mg content in the $\text{Mg}_x\text{Zn}_{1-x}\text{O}$ nanowire arrays by cathodoluminescence (CL) imaging of the excitonic peak energy and found the wire-to-wire fluctuation of the Mg content was negligible. H. Y. Yang et al ^[82] reported $\text{Mg}_x\text{Zn}_{1-x}\text{O}$ nanoneedles prepared by an ion-beam sputtering technique on $\text{Mg}_x\text{Zn}_{1-x}\text{O}$ thin

films with Mg contents of up to 21%. The $\text{Mg}_x\text{Zn}_{1-x}\text{O}$ nanoneedles had the cone structure, which had a length of 200-400 nm and a diameter of ~ 100 nm. The high temperature lasing of the $\text{Mg}_x\text{Zn}_{1-x}\text{O}$ nanoneedles implied the high crystal quality of the nanoneedles, enhancement of oscillator strength in nanostructures and a self-compensation mechanism in random laser cavities. MgZnO nanostructures with wurtzite phase could be prepared simply by thermal diffusion of Mg into the ZnO nanowires^[83]. ZnO nanowires were firstly synthesized on c-sapphire in a simple vapor transport process mediated by “self-catalyst” vapor-liquid-solid (VLS) growth. Then ZnO nanowires were spin-coated by the solution prepared by the sol-gel approach using acetate of magnesium in a homogeneous aqueous reaction medium. Finally, the samples were sintered at 1000°C for 2h while diffusion occurred to form the $\text{Mg}_x\text{Zn}_{1-x}\text{O}$ nanostructures. Based on the PL spectra of MgZnO nanostructures, the Mg composition was estimated to be around 7%.

In summary, $\text{Mg}_x\text{Zn}_{1-x}\text{O}$ nanostructures have attracted much attention because of its unique physical properties and multifunctionality. Many technologies have been investigated to grow $\text{Mg}_x\text{Zn}_{1-x}\text{O}$ nanostructures. The comparison for those growth technologies is listed in the table 2.2. Thermal evaporation and thermal diffusion methods are really attractive due to their simple growth process. But the high growth temperature and difficulties in control of Mg composition and surface morphology make those technologies unrealistic in large-scale fabrication of devices. Compared to thermal evaporation and diffusion technologies, PLD and ion-beam sputtering show advantages on controlling Mg incorporation and surface morphology of MgZnO nanostructures. Vertically well-aligned nanorods and nanoneedles with high Mg content, $\sim 20\%$ has been achieved by those technologies. But a high substrate T and high vacuum are needed

making the fabrication cost of these technologies relatively high. As MBE was used for $\text{Mg}_x\text{Zn}_{1-x}\text{O}$ nanostructures growth, a relatively low substrate temperature was used. But the usage of Ag catalyst and low Mg incorporation make this technology unpromising especially for photovoltaics. In comparison with all above technologies, MOCVD allows $\text{Mg}_x\text{Zn}_{1-x}\text{O}$ nanostructures to be grown at a relatively low substrate T without a catalyst, doesn't need a high vacuum and provides ability on good control of morphology and alloy composition.

Table 2.2 Comparison of growth technologies for $\text{Mg}_x\text{Zn}_{1-x}\text{O}$ nanostructures

	Advantages	Disadvantages
MOCVD	Low T_s ; Without using a catalyst; Good control of morphology and alloy composition.	Specific precursors (expensive, toxic); Expensive equipment.
PLD	Good control of morphology and alloy composition.	High T_s ; High vacuum; Usage of catalyst.
Ion-Beam Sputtering		
MBE	Low T_s .	Usage of catalyst; Low Mg incorporation.
Thermal Evaporation	Simple process; Low-cost fabrication.	High T_s ; Poor control of Mg incorporation and surface morphology.
Electrophoresis Deposition		

2.4 Metalorganic Chemical Vapor Deposition

Metalorganic chemical vapor deposition (MOCVD), also known as organometallic vapor phase epitaxy (OMVPE) is a chemical vapor deposition method usually for epitaxial growth of compound semiconductors. It follows the CVD process, in which one or more

volatile precursors, usually organic compounds or metalorganics and metal hydrides containing the required chemical elements, react and/or decompose on the substrate surface to produce the desired deposit. The growth of crystal is by chemical reaction not physical deposition, which takes place not in a vacuum but from the gas phase at moderate pressure (2-100 kPa). This technique is preferred for the formation of devices incorporating thermodynamically metastable alloys, and has become a major process in the manufacture of optoelectronics.

2.4.1 MOCVD system at Rutgers

The MOCVD growth system in Rutgers University is shown in Fig. 2.5. The MOCVD system is composed of three main parts: the reacting chamber, the gas delivering system, and the control system.

An I/O interface hardware, also called as data acquisition boards, with a software program loaded in the PC is used as the control system, controlling and monitoring the mass flow controllers (MFC), control valves, pneumatic valves and meanwhile maintaining temperature and pressure in the reactor and the gas lines.

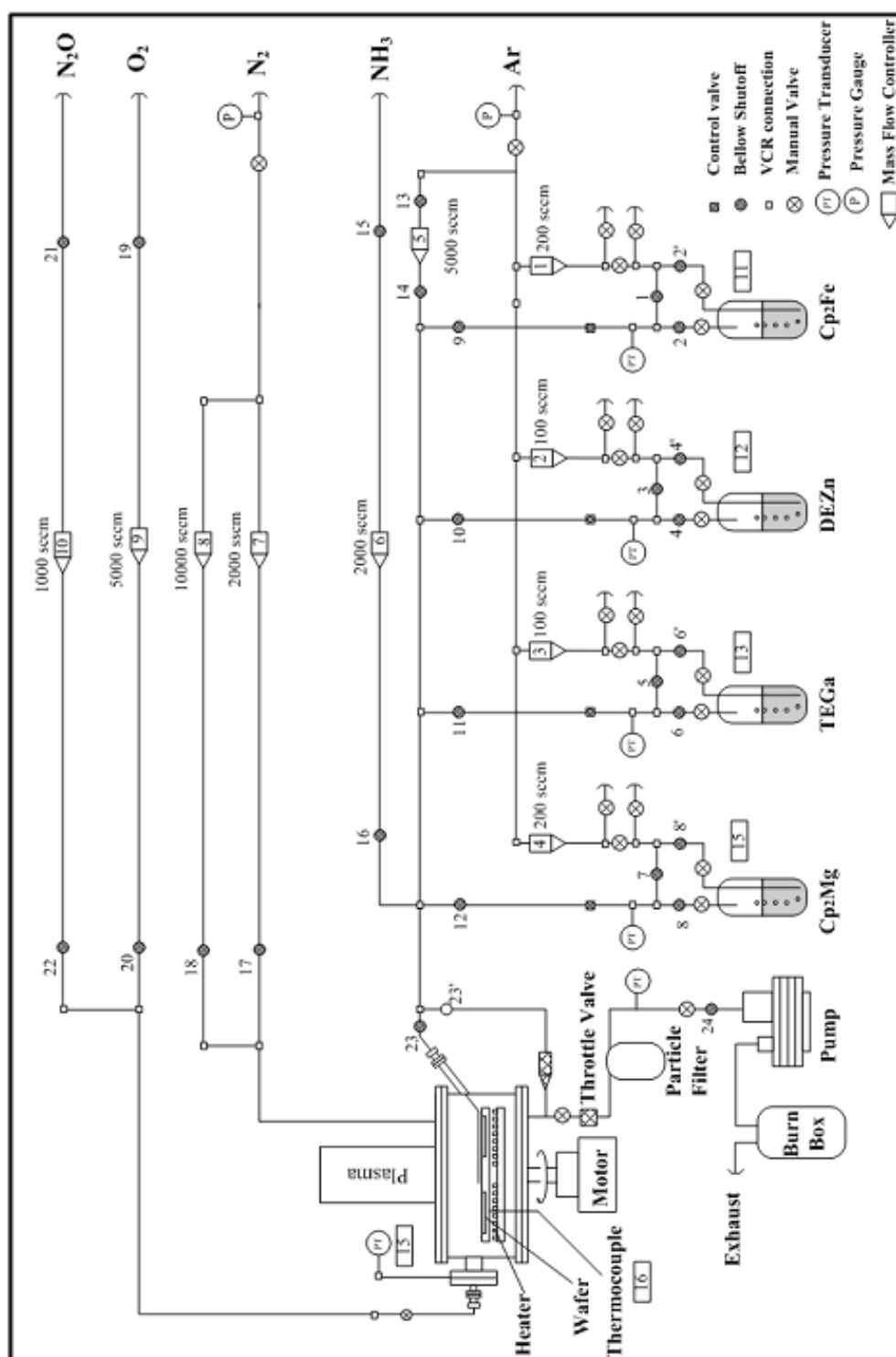


Figure 2.5 A schematic diagram of Rutgers MOCVD system for the growth of ZnO-based films and nanostructures.

The gas delivering system is composed of MFCs, control valves, pneumatic valves, throttle valves, pressure monitors, metal pipes and other connection components. N_2 is used as the carrier gas, which is introduced into the MOCVD reactor from the top. Ultra high purity (UHP) Ar gas is used as the carrier gas, which flows through the precursors bubblers to carry the vapor of precursors into the reactor. In the Rutgers MOCVD system, four precursors bubblers are used, which are MCp_2Mg (Cp_2Mg labeled in Fig. 2.5 is another precursor for Mg source), TEGa , DEZn and Cp_2Fe . Among them, MCp_2Mg and Cp_2Fe bubblers need to be kept at relatively high temperature (above room temperature, $\sim 45^\circ\text{C}$ for MCp_2Mg and $\sim 65^\circ\text{C}$ for Cp_2Fe) for enough high vapor pressure. In order to prevent the condensation of precursors vapors in the delivery lines and clogging of the gas handling system, all portions of this network that transport such chemical vapor must be heated to or above the evaporation temperature of the precursor. Therefore, the MCp_2Mg and Cp_2Fe lines are heated up to the inlet into the reactor. These requirements can be met by simply wrapping the delivery lines with electrically resistive heating tapes. To reduce the transit time of precursor vapor in the lines, an additional Ar push flow is added to the exit side of the bubblers, as shown in Fig. 2.5. Ultra high purity O_2 is used as a reactive gas and introduced into the reactor through a separate line. N_2O can also be used as a reactive gas. NH_3 gas sometimes is used as a dopant gas and can also be used to modify the structure development of films during the growth. The vacuum system consists of two stages, the first stage is a roots blower that allows a high volume of gas to flow, and the second stage is a roughing pump. The best vacuum that can be achieved by this system (with no gas flow) is 10^{-1} to 10^{-2} torr.

The MOCVD chamber is an axisymmetric rotating-disk vertical flow reactor, as shown in Fig. 2.6. It consists of a horizontal stainless steel susceptor, which is connected to a motor via electrical feedthroughs and can rotate at high speed. A substrate holder (3 inch or 4 inch) will be loaded on the susceptor and rotate with the susceptor during growth. A resistive filament made from Kanthal AF alloy is placed closely underneath the susceptor to heat the substrates. A thermocouple is inserted into the narrow space between the heating filament and the susceptor to monitor the substrate temperature. On top of the susceptor, there are two separated gas injectors (as shown in Fig. 2.6), which are metalorganic precursors carried by UHP Ar gas and reactive gas O_2 . Each injector has a series of small holes facing the substrate, and is placed horizontally at the optimum distance from the susceptor. The two injectors are separately positioned, such that the gases from each injector reach the substrate at different regions at any instant. This injector configuration provides the separation of metalorganic precursors from O_2 gas before reaching the substrate surface and thus prevents the phase reaction between precursors and oxygen. A small transit time for the gaseous species due to the high speed of gases coming out of the small holes on the injectors and the short distance from the injectors to the substrate also reduce the possibilities of gas phase reactions. To further reduce the transit time and prevent phase reaction, high volume flow of N_2 is introduced from the ceiling of the chamber to push the metalorganics and oxygen gas further down to the substrates. A microwave plasma system is installed at the top of the reactor for in-situ substrate cleaning and surface treatment of as-grown ZnO-based films and nanostructures.

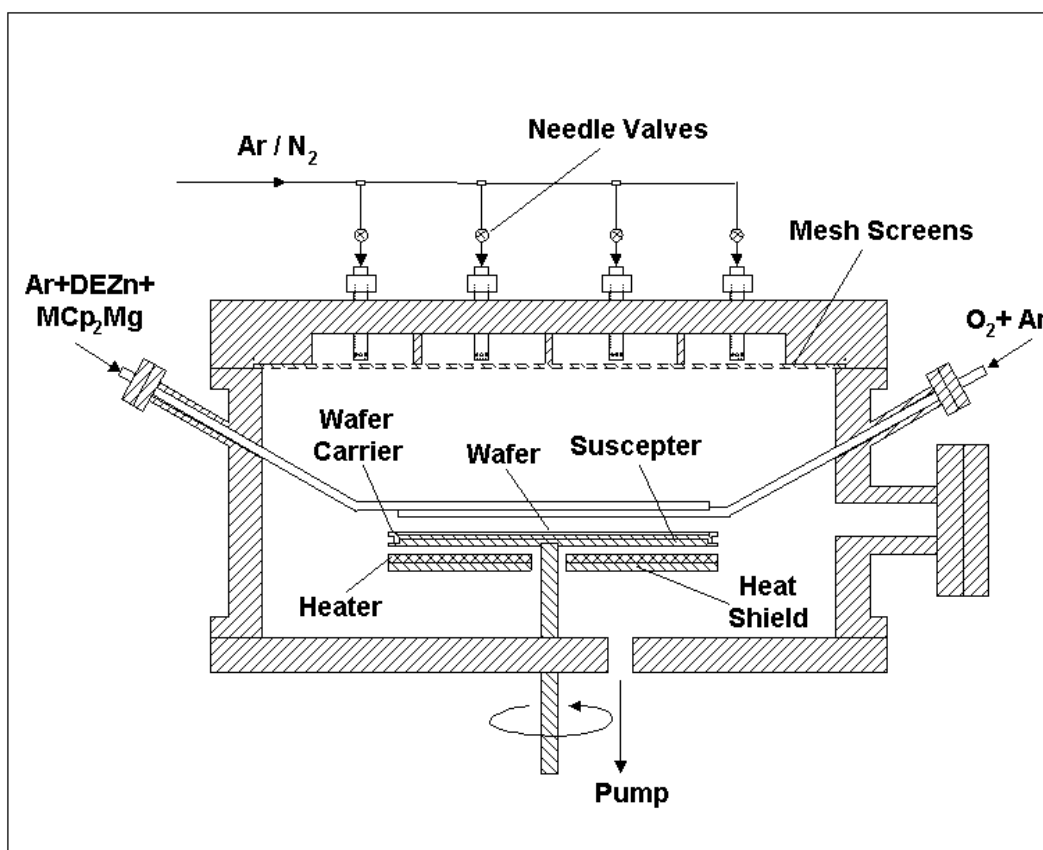


Figure 2.6 A schematic diagram of Rutgers MOCVD growth reactor for ZnO and $\text{Mg}_x\text{Zn}_{1-x}\text{O}$ growth.

In the MOCVD chamber, metalorganic precursors and reactive gases flow from the top of susceptor and exit through an exhaust at the bottom. A schematic diagram of the flow pattern over a rotating susceptor is shown in Fig. 2.7 ^[84]. The vertical velocity of gas flowing downward is reduced as it approaches the susceptor and is redirected radially, reaching a stagnation point of zero vertical velocity at the susceptor surface. The flow pattern in the chamber is characterized by a boundary layer of gas flux being dragged around the susceptor surface and thrown outwards by centrifugal force. This centrifugal pumping action also sucks down the gases toward the susceptor. When the susceptor is heated, the gas above the susceptor is heated and may rise up due to buoyancy, and then falls again after being re-cooled. This instability develops into circulating flow patterns. Such circulation of gas flow would lead to undesirable long residence time of gas molecules and thus cause gas phase reactions. Such circulating flow patterns have to be avoided since small particles formed due to gas-phase reactions may stay in the reactor and grow, and degrade the quality of as-grown films. In our MOCVD system, a large volume of N₂ gas flow is constantly introduced from the chamber ceiling to avoid the formation of that circulating flow pattern.

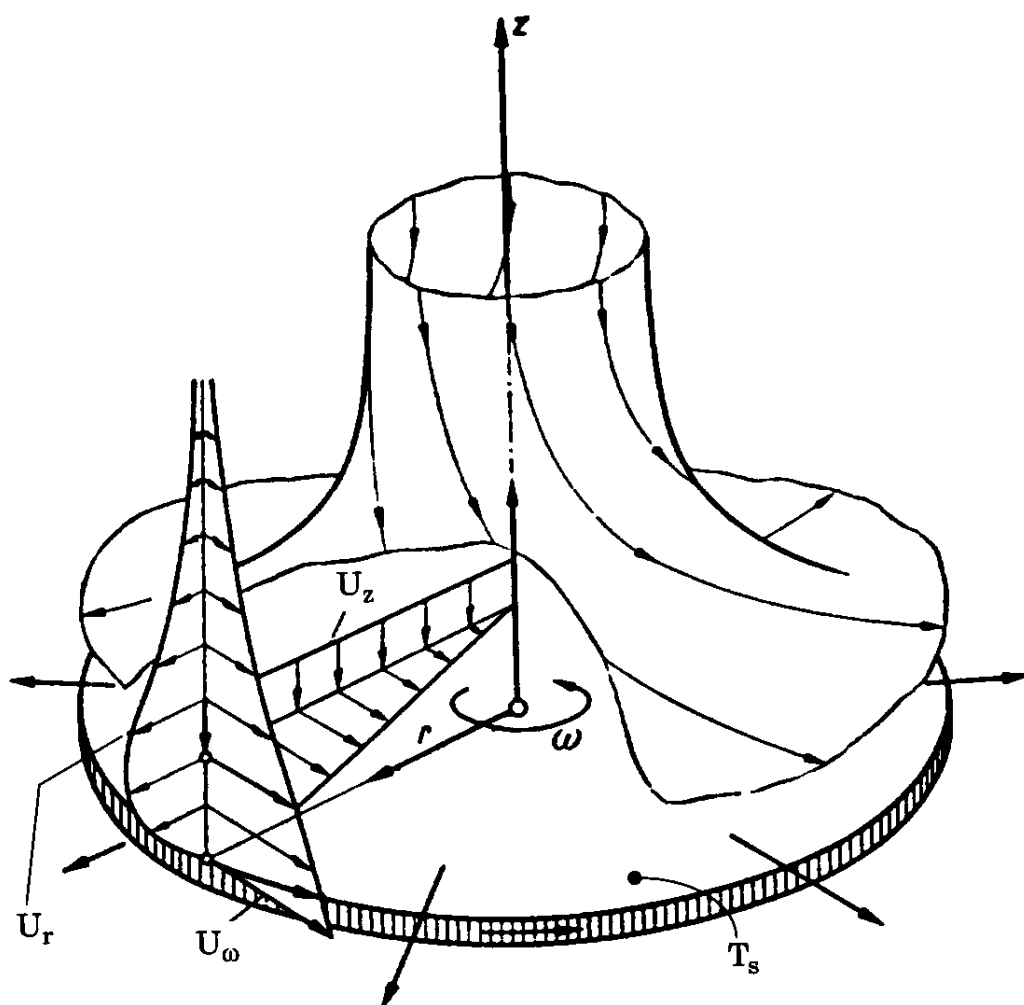


Figure 2.7 A schematic diagram of the flow patterns in an axisymmetric rotating-disk vertical flow reactor ^[84].

2.4.2 Metalorganic precursors and chemical reactions

The vapor pressure of a metalorganic precursor is a critical parameter that determines the concentration of metalorganic precursors entering the reactor, and subsequently the growth rate of the film in the MOCVD process. The vapor pressure of most metalorganic compounds is given by

$$\text{Log } (P(\text{torr})) = B - A/T(K) \quad (2.1)$$

where P (torr) is the metal organic vapor pressure, T (K) is the bubbler temperature, A and B are constants related to the properties of metalorganic materials. The constants A and B of some metalorganic compounds (used in our MOCVD system) and their vapor pressures at 298K are listed in Table 2.3.

Table 2.3. Vapor pressure and melting point of metalorganic precursors

Metalorganic precursor		Pressure at 298 K (mm Hg)	A	B	Melting point (°C)
Zn(C ₂ H ₅) ₂	DEZn	12	2109	8.28	-28
Zn(CH ₃) ₂	DMZn	300	1560	7.80	-42
Ga(C ₂ H ₅) ₃	TEGa	5.0	2162	8.08	-82.3
Mg(C ₅ H ₅) ₂	Cp ₂ Mg	0.04	3556	10.56	176
Mg(C ₆ H ₇) ₂	MCp ₂ Mg	0.24	2358	7.30	29
Fe(C ₅ H ₅) ₂	Cp ₂ Fe	0.005	3680	10.27	171

The flow rate of the metalorganic precursor vapor is determined by

$$F_{MO} = (P_{MO} / P_{Bubbler}) \times F_C \quad (2.2)$$

where F_{MO} and F_C are the flow rates of the metalorganic precursor vapor and carrier gas, respectively. P_{MO} is the vapor pressure of the metalorganic precursor and $P_{Bubbler}$ is the

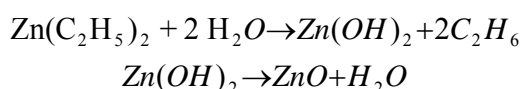
bubbler pressure. Once the flow rate of the metalorganic precursor is known, the concentration of metalorganic precursor entering the reactor can be calculated.

Since the vapor pressure of metalorganic precursors determines the growth rate of films, it is an important factor should be considered for the selection of precursors. Dimethyl Zinc [DMZn: $(\text{CH}_3)_2\text{Zn}$] and Diethyl Zinc [DEZn: $(\text{C}_2\text{H}_5)_2\text{Zn}$] are the most commonly used zinc metalorganic sources. In these two compounds, the Zn-C bond is predominantly covalent and the C-Zn-C group is linear as a result of *sp*-hybridization^[85]. In agreement with their non-polar character, these compounds are among the most volatile organometallic compounds. From Eq. 2.1 and Table 2.3, it is seen that DMZn has a higher vapor pressure than DEZn. A higher growth rate can be achieved by using DMZn instead of DEZn. But it has two main shortcomings:

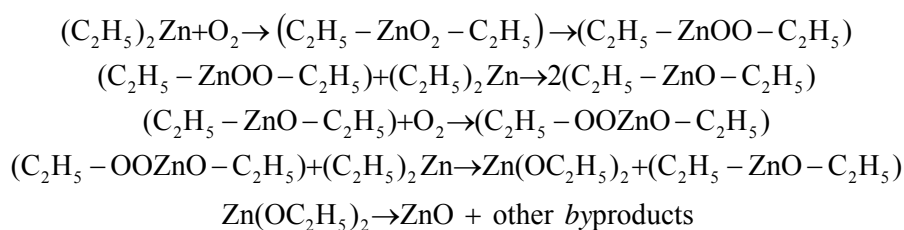
- (i) It has higher rates of carbon contamination during MOCVD film growth by using DMZn than by using DEZn. When DMZn and DEZn dissociatively adsorb onto most substrates at temperatures above 400 K, zinc metal and adsorbed methyl and ethyl groups are formed, respectively. Unlike methyl groups, the larger ethyl groups can undergo β -hydride elimination reactions to produce ethylene (C_2H_4), which then desorbs.
- (ii) Compared to DEZn, DMZn reacts much more vigorously with O_2 and H_2O . It is therefore, difficult to limit gas phase reactions if DMZn is used.

With those considerations, we chose DEZn as the Zinc Precursor. The melting point of DEZn is -28°C , and the boiling point is 117°C and 30°C at pressures of 760 mm Hg and 27 mm Hg, respectively. The strongly electrophilic (accepts an electron) characteristics of zinc ions largely determine the chemical behavior of DEZn. They are electron deficient compounds in that the number of low-lying orbitals available for bonding (four) is greater

than the number of bonding electron pairs (two). This presence of vacant orbitals for bonding explains the tendency of DEZn to form complexes with compounds containing hetero-atoms with free electron pairs (O, N, P, S etc.). This serves to explain the great chemical reactivity of DEZn. DEZn is highly susceptible to be attacked by oxygen and water vapor. The reaction of DEZn with water is as



The reaction of DEZn with oxygen is more complicated ^[86]. A probable reacting route is:



For Mg precursors, two commercially available metalorganic compounds, Bis-(methylcyclopentadienyl)magnesium (MCp_2Mg) and Bis-(cyclopentadienyl)magnesium (Cp_2Mg), are usually used. MCp_2Mg has a melting point of 29°C and its boiling point is 56°C at 0.3mm Hg, while Cp_2Mg , when pure, is a white solid having a melting point of ~281°C. Use of Cp_2Mg often requires additional purification when received from vendors if reproducible doping results are to be obtained ^[87], which can be time consuming and expensive. MCp_2Mg , structurally similar to Cp_2Mg , however has a lower melting point (29°C), permitting the source to be used as a liquid and without any complicated purification process. Therefore, MCp_2Mg is the most common magnesium precursor of choice for MOCVD growth of II-VI compounds. Both the precursors react pyrophorically when exposed to air. In our MOCVD system, MCp_2Mg is chosen as the Mg precursor.

2.5 Summary

In this chapter, a technical background review for this dissertation is presented. Fundamental properties of $\text{Mg}_x\text{Zn}_{1-x}\text{O}$ alloy and its applications are reviewed first. Based on the thermodynamics, the solid solubility of MgO in ZnO is very limited. However, it is found that that solid solubility can be extended by using non-equilibrium growth methods. Due to its tunable bandgap, $\text{Mg}_x\text{Zn}_{1-x}\text{O}$ has been widely used in many electronic and optoelectronic devices. While lots of research projects focused on $\text{Mg}_x\text{Zn}_{1-x}\text{O}$ epitaxial films growth, little attention has been put on $\text{Mg}_x\text{Zn}_{1-x}\text{O}$ polycrystalline films and nanostructures, which are usually applicable in photovoltaic applications. We then do a comprehensive review on various growth technologies for $\text{Mg}_x\text{Zn}_{1-x}\text{O}$ polycrystalline films and nanostructures. Among them, MOCVD is an attractive technology, which not only provides ability of in-situ doping and alloying but also provides controllability of surface morphology of $\text{Mg}_x\text{Zn}_{1-x}\text{O}$. Finally, the MOCVD system at Rutgers and precursors selection are presented and discussed.

Chapter 3 Growth and characterization of $\text{Mg}_x\text{Zn}_{1-x}\text{O}$

polycrystalline films

ZnO has become a promising photovoltaic material ^[88] because of its large direct bandgap, abundance on earth, non-toxicity, and adjustable n-type doping. ZnO can be alloyed with MgO to form the ternary $\text{Mg}_x\text{Zn}_{1-x}\text{O}$, which has a wide variation of bandgap values from ~ 3.3 eV (ZnO) to ~ 7.8 eV (MgO). With bandgap tunability, $\text{Mg}_x\text{Zn}_{1-x}\text{O}$ is used as a window layer in Cu(In,Ga)Se₂ (CIGS) solar cells to tune the conduction band offset for improved device performance ^[89, 13]. $\text{Mg}_x\text{Zn}_{1-x}\text{O}$ is used to enhance the open circuit voltage V_{OC} in poly(3-hexylthiophene) (P3HT)- $\text{Mg}_x\text{Zn}_{1-x}\text{O}$ hybrid solar cells ^[14]. As discussed before, the surface morphology of $\text{Mg}_x\text{Zn}_{1-x}\text{O}$ plays important roles on performances of various solar cells. Two-dimensional (2-D) film with smooth surface is needed for conventional inorganic p-n junction type solar cells.

So far, most growth studies on $\text{Mg}_x\text{Zn}_{1-x}\text{O}$ have been focused on epitaxial thin films deposited on various sapphire substrates with different orientations. Only little information on polycrystalline $\text{Mg}_x\text{Zn}_{1-x}\text{O}$ films for photovoltaic applications is available ^[14, 23]. Moreover, most of these reported results were obtained on the samples grown on fused silica or Si substrates. The growth mechanism of $\text{Mg}_x\text{Zn}_{1-x}\text{O}$ polycrystalline films on transparent conductive electrodes, e.g. GZO films, has not been explored. In this chapter, we report the results of $\text{Mg}_x\text{Zn}_{1-x}\text{O}$ polycrystalline films grown on GZO films by MOCVD.

3.1 Growth optimization of GZO films

Ga-doped ZnO (GZO) has been developed as a new transparent conductive oxide (TCO). In comparison with tin-doped indium oxide (ITO), one of the commonest TCOs, GZO is inexpensive and ecologically-friendly. Recently, a novel structure, formed by ZnO films or nanostructures grown on GZO film/glass substrate, has been used in photovoltaic devices such as DSSCs ^[90], and Cu₂O-ZnO heterojunction solar cells ^[91]. In such a structure, GZO provides small potential barrier to ZnO, favoring the charge collection in the solar cells.

GZO films were grown in a rotating disc MOCVD reactor (Rutgers MOCVD system). Diethylzinc (DEZn) and triethylgallium (TEGa) were used as the Zn and Ga precursor, respectively. Ultra high purity Ar and O₂ gas were used as the carrier and oxidizer, respectively. GZO films were grown on the glass substrates at a chamber pressure of ~50 torr, and a relatively low substrate temperature T_s (380-430°C) to achieve the dense and smooth films with low resistivity. The optimization of substrate temperature has been done by H. Chen in our group. More details can be found in the reference ^[92]. Besides the substrate temperature, the Ga content is another critical factor determining the electrical properties of GZO films, which was controlled by adjusting the precursor flow rate ratio (TEGa/DEZn).

The resistivity of GZO films was characterized by Hall measurement. Figure 3.1 shows the resistivity of GZO films as a function of Ga content. The Ga content was measured by XPS. From this figure, it is easily seen that the resistivity of GZO film decreases with the Ga content. A minimum resistivity of 9.6×10^{-4} ohm·cm, corresponding to a sheet resistance of 12 ohm/square for a 800 nm-thick film, is obtained on GZO film with a 10% of Ga%.

The relationship between Ga concentration and sheet resistance of GZO films has been reported ^[93]. The decreased resistivity with increasing Ga content is easily understood. As Ga is incorporated into ZnO lattice, it replaces Zn^{2+} , serving as a positive defect $\text{Ga}_{\text{Zn}}^{\bullet}$ and thus producing a free electron. As a result, the carrier (electrons) concentration increases with increasing Ga content. Since the resistivity of films is a function of carrier concentration, increased carrier concentration leads to a decrease of resistivity. But the resistivity stops increasing as the carrier concentration as well as the Ga content arrive at some certain value ^[93, 94]. The reason has been attributed to the increase of ionized impurity scattering with increasing carrier concentration. The increased ionized impurity scattering leads to the decreased mobility and increased resistivity. Therefore, an optimum Ga content exists for a lowest resistivity of GZO films, which is around 10-11% in our cases.

The XRD patterns of GZO films with different Ga contents are shown in Fig. 3.2. It is observed that all GZO films have a polycrystalline structure. The Ga content ($\leq 10\%$) doesn't change the wurtzite structure of ZnO. No impurity phases are detected from these XRD patterns. Besides that, we find that the texture of GZO films changes with the Ga incorporation. The preferred orientation (PO) of GZO films change from (10-11) plane to (10-10) plane. Similar phenomenon, i.e. that the PO of GZO films was changing with the Ga content, was reported in the reference ^[95]. But in that case, the PO of GZO films changed from (0002) plane to (10-11) plane with increasing Ga content. It was explained as that the Ga created new nucleation centers during growth process, which in turn changed the nucleation type from homogeneous to heterogeneous and deteriorated the crystal structure ^[95]. Although the direct experimental data is still lacked to explain the PO changes, it is reasonable to guess that the Ga incorporation changes the surface energy of

ZnO and thus influences the texturing of films. Besides the Ga content, the growth parameters during MOCVD growth could also change the PO of GZO films. Figure 3.3 shows the PO of GZO films (with same Ga% of ~10%) changes from (10-10) plane to (0002) plane when the substrate temperature increases from 430°C to 480°C. Same phenomenon was also observed and moreover explained by H. Chen et al.^[92] in our group. Similar PO change with operating parameters was reported in the reference^[96]. More work that discussed about relationship between operating conditions and PO of non-epitaxial polycrystalline ZnO films can be found in the review^[97].

The optical properties of GZO film were also characterized by using a UV-visible spectrophotometer. The transmission spectra of GZO film (with the minimum resistivity of 9.6×10^{-4} ohm·cm) is shown in the Figure 3.4, from which a high transmission >85% in the visible region can be seen. Figure 3.5 shows the FESEM image of such GZO film. The as-grown GZO film appears to be dense with a flat surface. Such dense GZO film, with a flat surface and a low resistivity (9.6×10^{-4} ohm·cm) will be used as a substrate for the following growth optimization of $\text{Mg}_x\text{Zn}_{1-x}\text{O}$ polycrystalline films.

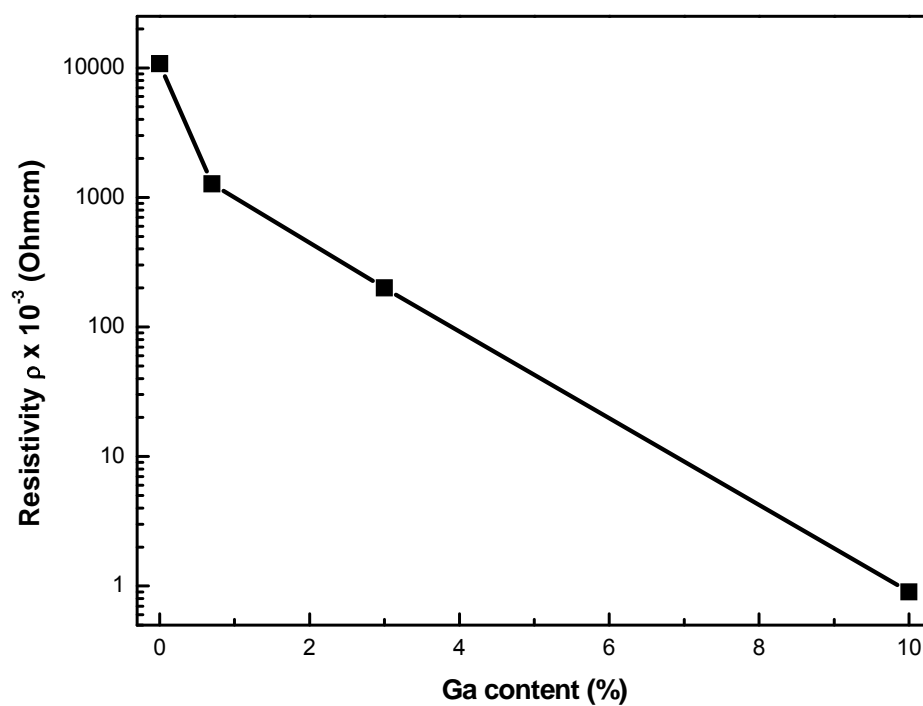


Figure 3.1 Resistivity of GZO films as a function of Ga content.

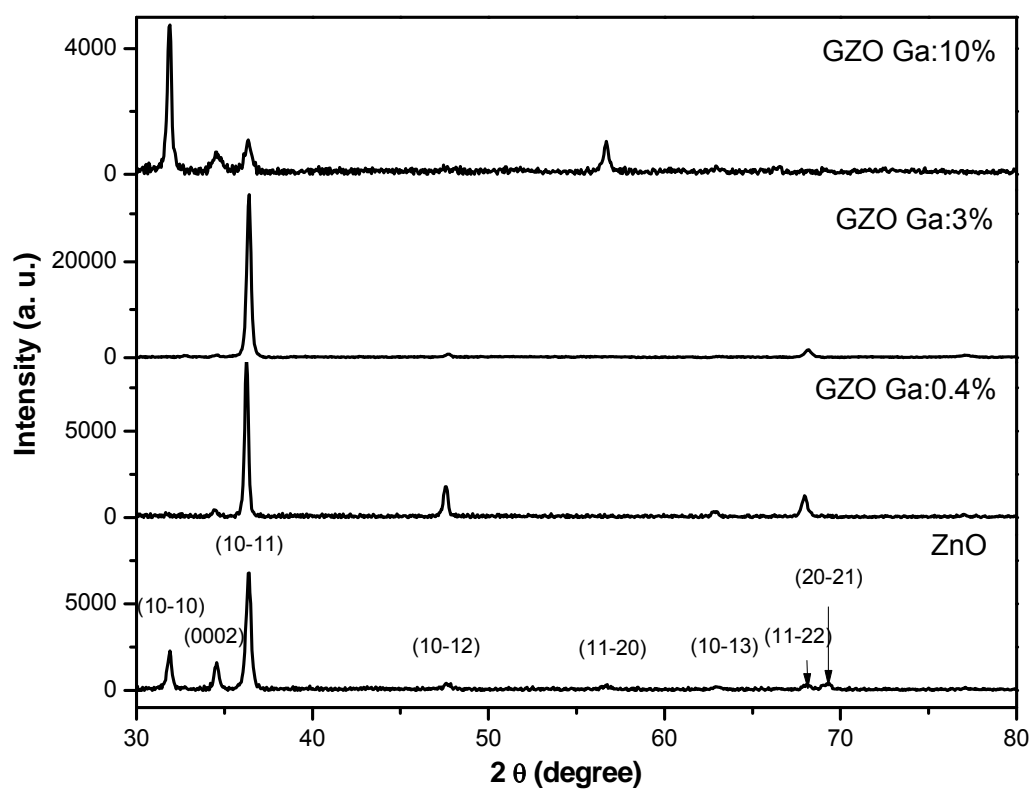


Figure 3.2 XRD results of GZO films with different Ga content, in which pure ZnO is included for a comparison.

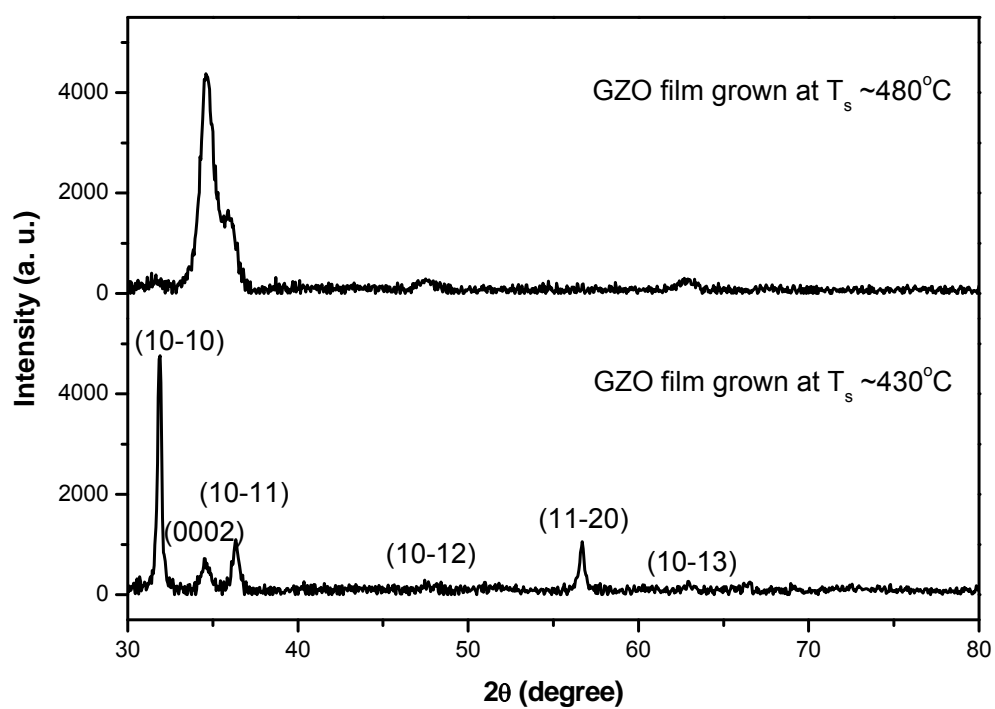


Figure 3.3 XRD patterns of GZO films with same Ga content ($\sim 10\%$) grown at different T_s .

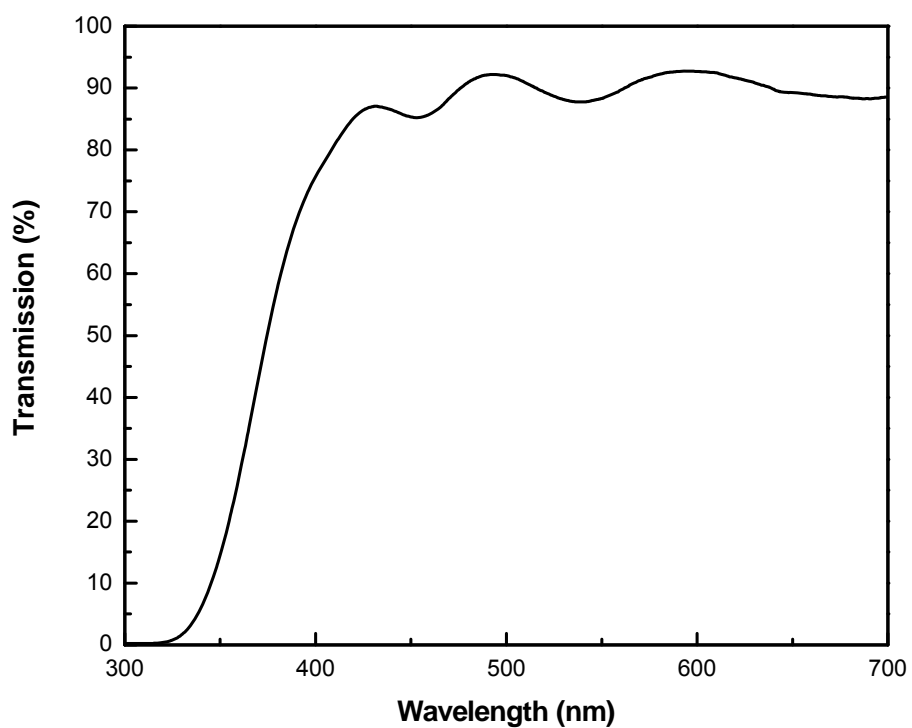


Figure 3.4 Transmission spectra of GZO film with a 10% of Ga% and a low resistivity of $9.6 \times 10^{-4} \text{ ohm}\cdot\text{cm}$.

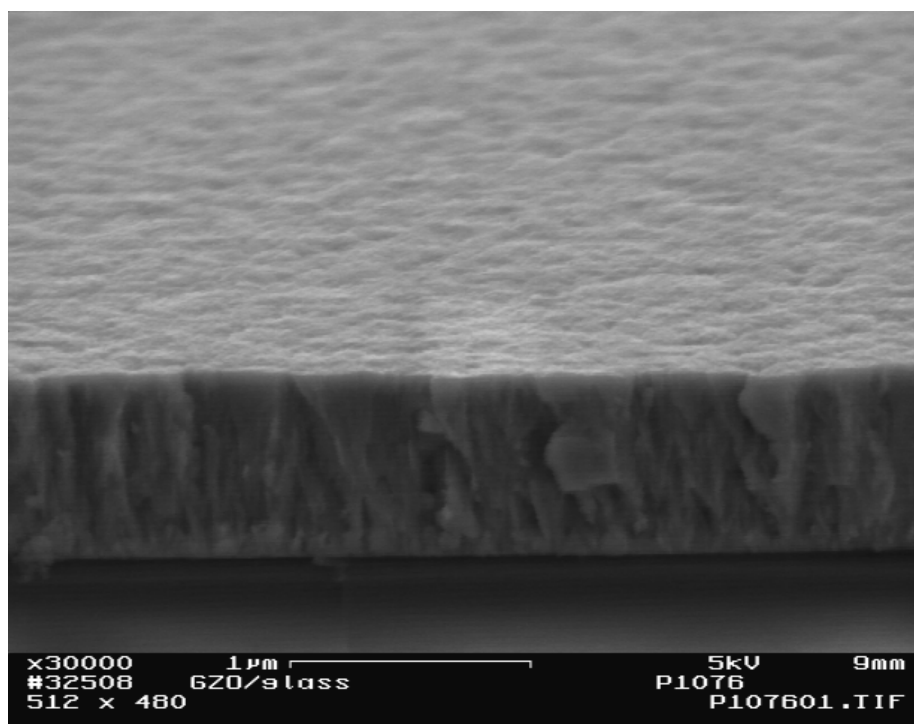


Figure 3.5 FESEM image of GZO film with a 10% of Ga% and a low resistivity of 9.6×10^{-4} ohm·cm.

3.2 Growth of $\text{Mg}_x\text{Zn}_{1-x}\text{O}$ polycrystalline films on GZO films

The $\text{Mg}_x\text{Zn}_{1-x}\text{O}$ ($0 \leq x \leq 0.1$) thin films were sequentially grown on the GZO/glass substrate at a relatively high substrate temperature T_s (500-530°C) and chamber pressure (~60 torr) for effective Mg incorporation and good crystalline quality. Bismethylecyclopentadienyl magnesium (MCp_2Mg) is used as the Mg precursor. The Mg composition in $\text{Mg}_x\text{Zn}_{1-x}\text{O}$ can be tuned by adjusting flow rate ratio ($\text{MCp}_2\text{Mg}/\text{DEZn}$) under appropriate growth conditions.

Shown in figure 3.6(a) is the $\text{Mg}_x\text{Zn}_{1-x}\text{O}$ thin film (~300nm) grown at high temperature (500°C-530°C) on the GZO film. The $\text{Mg}_x\text{Zn}_{1-x}\text{O}$ film has good crystalline quality and optical property due to similar lattice parameters of GZO and $\text{Mg}_x\text{Zn}_{1-x}\text{O}$. However the film appears to have a columnar structure with a rough surface. Such rough film is unfavorable for making the conventional p-n junction solar cells. In order to modify the surface morphology of $\text{Mg}_x\text{Zn}_{1-x}\text{O}$ films, a LT ZnO buffer layer (~20 nm) was grown initially followed by subsequent growth of $\text{Mg}_x\text{Zn}_{1-x}\text{O}$ films. The resulted surface morphology of $\text{Mg}_{0.08}\text{Zn}_{0.92}\text{O}$ thin film is shown in Fig. 3.6(b), where the film becomes dense with a smooth surface in comparison with the morphology of the $\text{Mg}_{0.08}\text{Zn}_{0.92}\text{O}$ thin film grown on the GZO without a ZnO buffer layer shown in Fig. 3.6(a).

The surface roughness of $\text{Mg}_x\text{Zn}_{1-x}\text{O}$ films is examined by atomic force microscopy (AFM). Fig. 3.7(a) and (b) show the 3-D AFM images of $\text{Mg}_{0.08}\text{Zn}_{0.92}\text{O}$ thin films grown without and with a LT ZnO buffer, respectively. The surface roughness (root mean square, i.e. RMS, value) of the $\text{Mg}_{0.08}\text{Zn}_{0.92}\text{O}$ film directly grown on a GZO film without a buffer is ~18 nm, while the film grown with a LT ZnO buffer has a reduced roughness

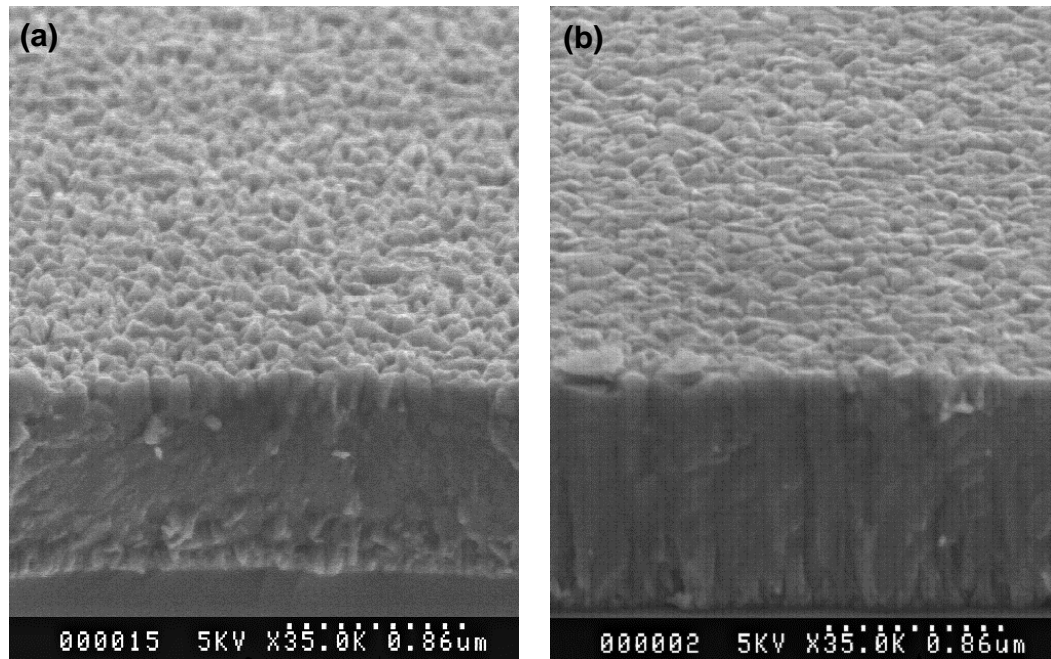


Figure 3.6 FESEM images of (a) $\text{Mg}_{0.08}\text{Zn}_{0.92}\text{O}$ film grown on GZO without a buffer layer, (b) $\text{Mg}_{0.08}\text{Zn}_{0.92}\text{O}$ film grown on GZO with a LT ZnO buffer layer.

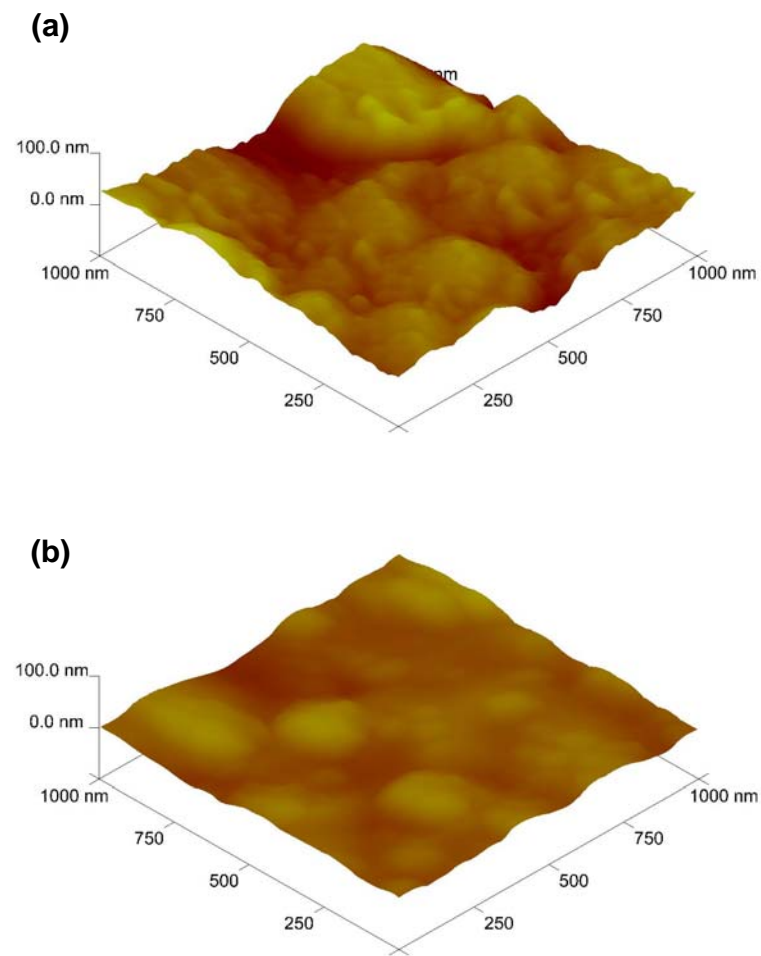


Figure 3.7 AFM images of $\text{Mg}_{0.08}\text{Zn}_{0.92}\text{O}$ film grown on GZO film (a) without any buffer, (b) with a LT ZnO buffer.

of ~ 8 nm. The low-temperature grown ZnO buffer improved the $\text{Mg}_x\text{Zn}_{1-x}\text{O}$ film surface roughness.

To understand the influence of the LT ZnO buffer on the surface morphology of $\text{Mg}_x\text{Zn}_{1-x}\text{O}$ films, XRD is conducted on the $\text{Mg}_{0.08}\text{Zn}_{0.92}\text{O}$ films. Shown in Fig. 3.8 are the XRD θ - 2θ scans on the $\text{Mg}_x\text{Zn}_{1-x}\text{O}$ /GZO films without and with the LT ZnO buffer layer. For comparison, the results of a GZO film and a $\text{Mg}_{0.08}\text{Zn}_{0.92}\text{O}$ film directly grown on glass substrates are also included. The GZO film shows a polycrystalline structure with a preferential orientation along [10-10] (Fig. 3.8(i)). The $\text{Mg}_{0.08}\text{Zn}_{0.92}\text{O}$ film grown on a glass substrate at high temperature of 500-530°C is c-axis oriented (Fig. 3.8(ii)). Fig. 3.8(iii) shows the XRD pattern of $\text{Mg}_{0.08}\text{Zn}_{0.92}\text{O}$ film grown on GZO film without the LT ZnO buffer. The XRD shows the polycrystalline structure similar to that of GZO films (Fig. 3.8(i)) but with a stronger peak on (0002). The XRD result of $\text{Mg}_{0.08}\text{Zn}_{0.92}\text{O}$ film grown on GZO film with the LT ZnO buffer is shown in Fig. 3.8(iv), where the (0002) peak intensity is negligible compared to other peaks, indicating that the c-axis preferred growth of $\text{Mg}_{0.08}\text{Zn}_{0.92}\text{O}$ is suppressed with the use of the LT ZnO buffer. Furthermore, the resulting $\text{Mg}_{0.08}\text{Zn}_{0.92}\text{O}$ film has a textured structure with a preferred orientation along [10-10]. Since the orientation with the fast growth rate, i.e. [0002], is in the plane of (10-10), the elongated grains develop in-plane of the GZO surface during the growth, making the $\text{Mg}_{0.08}\text{Zn}_{0.92}\text{O}$ film dense and smooth.

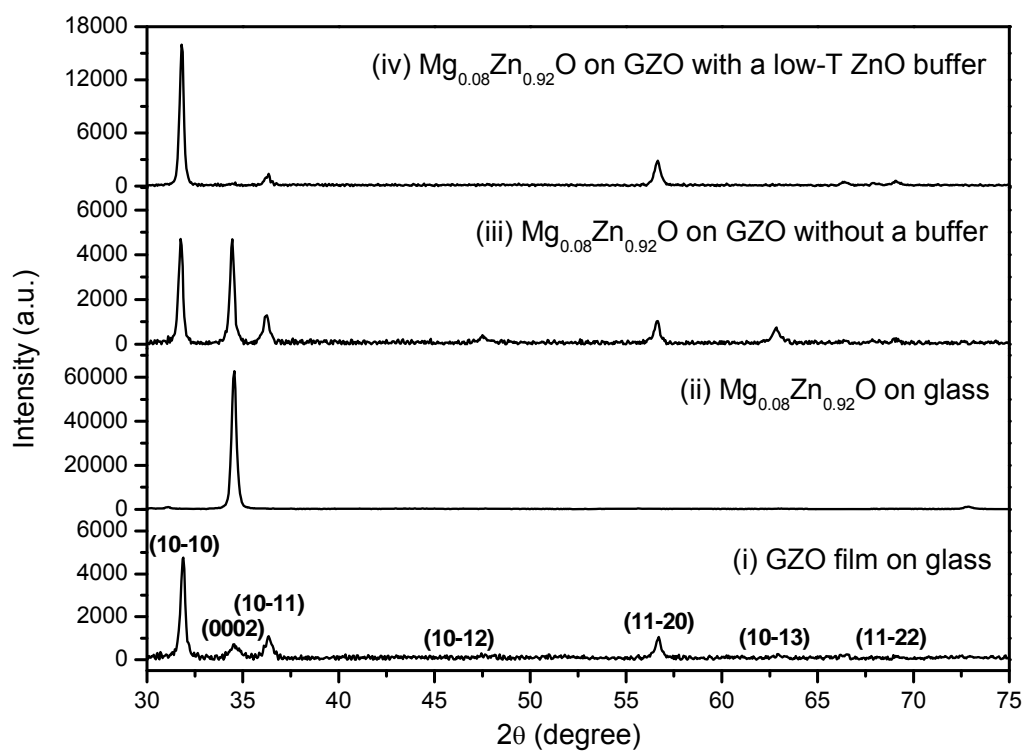


Figure 3.8 The XRD pattern of (i) GZO film on glass, (ii) $\text{Mg}_{0.08}\text{Zn}_{0.92}\text{O}$ film grown on glass, (iii) $\text{Mg}_{0.08}\text{Zn}_{0.92}\text{O}$ film grown on GZO film without a buffer and (iv) and $\text{Mg}_{0.08}\text{Zn}_{0.92}\text{O}$ film grown on GZO film with a LT ZnO buffer.

The LT buffer layer, followed by HT growth, has been widely used in ZnO epitaxial films growth on various single crystal substrates to improve the film crystalline quality, surface roughness, and optical properties [98, 99, 100, 101]. The improvements are mainly attributed to the minimization of the strain caused by the lattice and thermal mismatches between the epilayer and the substrate. In our case, however, both $\text{Mg}_x\text{Zn}_{1-x}\text{O}$ and GZO have the wurtzite structure with similar lattice constants, so that the strain effect is small. Based on the characterization results from SEM, AFM and XRD, it is evident that MgZnO nucleation and then growth are affected by LT ZnO buffer effects. When a $\text{Mg}_{0.08}\text{Zn}_{0.92}\text{O}$ film is directly grown on a glass substrate, due to lack of crystallographic alignment, the adatoms (at the high deposition temperature) diffuse on the surface to arrange themselves towards the lowest surface energy. Since the (0002) plane of $\text{Mg}_x\text{Zn}_{1-x}\text{O}$ ($x < 0.10$) has the highest surface energy [68], it would be covered foremostly by adatoms and the $\text{Mg}_x\text{Zn}_{1-x}\text{O}$ ($x < 0.10$) thin film grows predominantly along the c-axis direction, while growth of crystals with other orientations is inhibited (Fig. 3.8(ii)). The GZO polycrystalline film shows a different surface from that of amorphous glass. Although the crystallographic alignment exists, the adatoms (at high deposition temperature) prefer to coalesce into 3D nuclei at grain boundaries, surface defects, and terraces because all of them are active surface sites and the activation energy for bonding on these sites is lower than elsewhere. Presence of Ga-atoms could also act as nucleation sites [102]. With surface energy anisotropy of $\text{Mg}_x\text{Zn}_{1-x}\text{O}$ crystal, those 3D nuclei easily develop into c-orientated texture (Fig. 3.8(iii)). Since those nucleus sites, introduced by crystal defects and surface terraces, are not uniformly distributed on the substrate surface, the 3-D nucleation usually leads to a rough film (Fig. 3.6(a) and 3.7(a)). When using a LT ZnO buffer, however, the nucleation

behavior is changed. At the low substrate temperature ($\sim 250^\circ\text{C}$), the nucleation is kinetically inhibited. The adatoms reduce surface diffusion energy and prefer the crystallographic sites similar to the GZO film for the interface energy minimization. The LT buffer thus follows the polycrystalline GZO structure but with a developed surface having less surface defects and Ga-atoms. The subsequent HT growth of a $\text{Mg}_x\text{Zn}_{1-x}\text{O}$ film then follows the crystallographic alignment (*i.e.* polycrystalline in this case) of the buffer and the GZO (Fig. 3.8(iv)).

3.3 Summary

We optimized the growth of GZO films on glass substrates by using MOCVD. A relatively low substrate temperature (380°C - 430°C) was used to achieve dense and smooth film. The resistivity was found to be varying with the Ga content and a minimum resistivity of 9.6×10^{-4} ohm-cm was obtained on the GZO film with the Ga content of $\sim 10\%$. It was also found that the texture of GZO films changed with the Ga content and growth parameters. With the increase of the Ga content, the PO of GZO films switched from (10-11) to (10-10). And with the increase of substrate temperature, the PO of GZO films changed from (10-10) to (0002). The optimized GZO film with a low resistivity and high transmittance was used as a substrate for the growth optimization of $\text{Mg}_x\text{Zn}_{1-x}\text{O}$ polycrystalline films.

$\text{Mg}_x\text{Zn}_{1-x}\text{O}$ polycrystalline films were sequentially grown on GZO films. A relatively high substrate temperature T_s (500 - 530°C) was used for effective Mg incorporation and good crystalline quality. The $\text{Mg}_x\text{Zn}_{1-x}\text{O}$ polycrystalline film directly grown on GZO films had a column structure with a rough surface, which is not favorable for making the

conventional p-n junction solar cells. A thin buffer layer was used to modify the surface morphology and roughness. Growth of a LT ($\sim 250^{\circ}\text{C}$) ZnO buffer, followed by high temperature growth of $\text{Mg}_x\text{Zn}_{1-x}\text{O}$, resulted in a high quality polycrystalline $\text{Mg}_x\text{Zn}_{1-x}\text{O}$ film with smooth surface morphology. A growth mechanism was proposed to explain the experimental results.

Chapter 4 Growth and characterization of $\text{Mg}_x\text{Zn}_{1-x}\text{O}$ nanostructures

As discussed in the section 2.3, the growth of 1-D wurtzite $\text{Mg}_x\text{Zn}_{1-x}\text{O}$ nanostructures is more challenging than that of ZnO nanostructures, especially for high Mg content ($>4\%$, the thermodynamic solid solubility of MgO in ZnO). Many technologies, such as MBE, PLD, MOCVD, thermal evaporation etc., have been adopted to grow various nanostructured $\text{Mg}_x\text{Zn}_{1-x}\text{O}$. MOCVD is particularly attractive due to its damage-free process, the ability to realize well control of in-situ doping, alloy composition and surface morphology. Recently, good $\text{Mg}_x\text{Zn}_{1-x}\text{O}$ nanorods with high Mg content ($>15\%$) have been achieved by MOCVD [69, 70]. However, the growth mechanism is not clear yet. The initial growth approaches such as the usage of buffer layers, which we think is very critical for the $\text{Mg}_x\text{Zn}_{1-x}\text{O}$ nanostructures growth, varies with different reports. Both a low T MgZnO buffer and no buffer are reported to be working for the formation of 1-D MgZnO nanostructures. In this chapter, we try to optimize growth of 1-D $\text{Mg}_x\text{Zn}_{1-x}\text{O}$ nanotips on Si substrates firstly. The buffer layer effects on the growth of 1-D wurtzite $\text{Mg}_x\text{Zn}_{1-x}\text{O}$ nanostructures will be studied. Then the $\text{Mg}_x\text{Zn}_{1-x}\text{O}$ nanostructures are grown on GZO film for photovoltaics. A growth mechanism will be proposed.

4.1 Optimization of $\text{Mg}_x\text{Zn}_{1-x}\text{O}$ nanotips growth on Si substrates

$\text{Mg}_x\text{Zn}_{1-x}\text{O}$ nanotips were grown on Si substrates by the MOCVD technology. The diethylzinc (DEZn) and bismethylcyclopentadienyl magnesium (MCp_2Mg) were used as Zn and Mg precursors, respectively. Ultra high purity O_2 was used as oxidizer gas and Ar

as carrier gas. The Mg composition was tuned by adjusting the flow rate of MCp_2Mg under a fixed O/Zn precursors flow rate ratio. Growth parameters, including the substrate temperature, O/Zn precursors flow rate ratio, chamber pressure were found to play important roles on the $\text{Mg}_x\text{Zn}_{1-x}\text{O}$ nanotips growth, and thus would be optimized. Besides, buffer layers were used during the $\text{Mg}_x\text{Zn}_{1-x}\text{O}$ nanotips growth. The effect of buffer layers on the $\text{Mg}_x\text{Zn}_{1-x}\text{O}$ nanotips growth would be investigated.

4.1.1 Substrate temperature

The substrate temperature, T_s , is a very important variable during the growth, having profound effects on the morphology and composition of $\text{Mg}_x\text{Zn}_{1-x}\text{O}$ nanotips. Figure 4.1 shows FESEM images of $\text{Mg}_x\text{Zn}_{1-x}\text{O}$ ($x \sim 7\text{-}8\%$) nanotips grown on Si substrates at different T_s . It is found that a high T_s ($\geq 530^\circ\text{C}$) is preferred to form 1-D nanostructures. But the nanotips grown at higher T_s ($> 560^\circ\text{C}$) are not uniform, as shown in Fig. 4.1(d). It could be explained as that the probabilities of gas phase reaction near the film surface increase with increasing T_s leading to the development of some particles. Those particles could serve as nucleation centers inducing the fast growth of some nanotips and thus degrading the uniformity of the nanotips.

Figure 4.2 shows transmission spectra of $\text{Mg}_x\text{Zn}_{1-x}\text{O}$ nanotips grown at different T_s . As seen, the absorption edge of $\text{Mg}_x\text{Zn}_{1-x}\text{O}$ samples shift towards a longer wavelength with the increase of T_s . It means that a decrease of Mg incorporation happens as the substrate temperature increases. The molecule of MCp_2Mg , the precursor of Mg, has a larger mass than that of DEZn , the precursor of Zn. Since the desorption probability is a function of

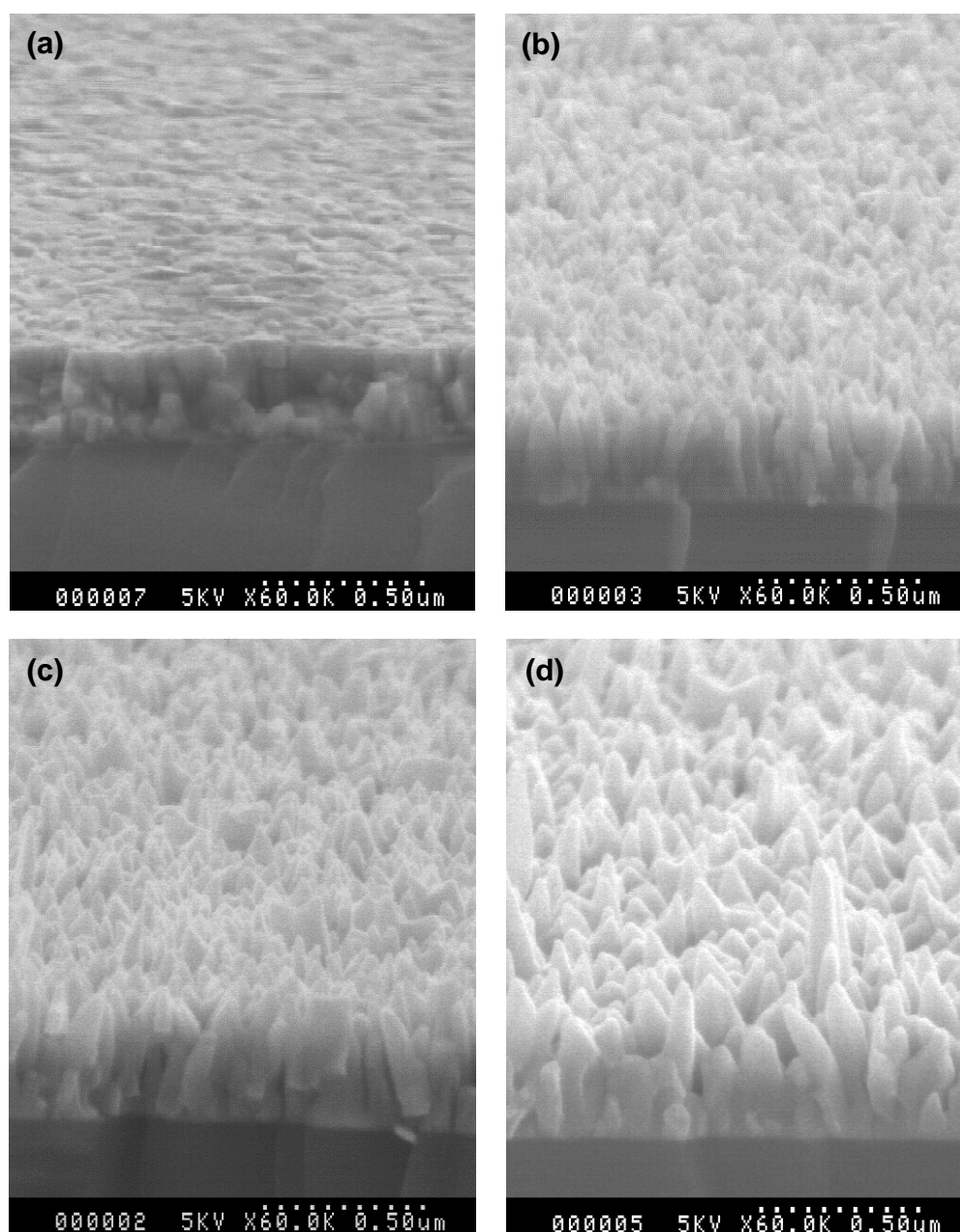


Figure 4.1 FESEM images of $\text{Mg}_x\text{Zn}_{1-x}\text{O}$ nanotips grown on Si substrates at different T_s (a) 500°C, (b) 530°C, (c) 560°C, (d) 590°C.

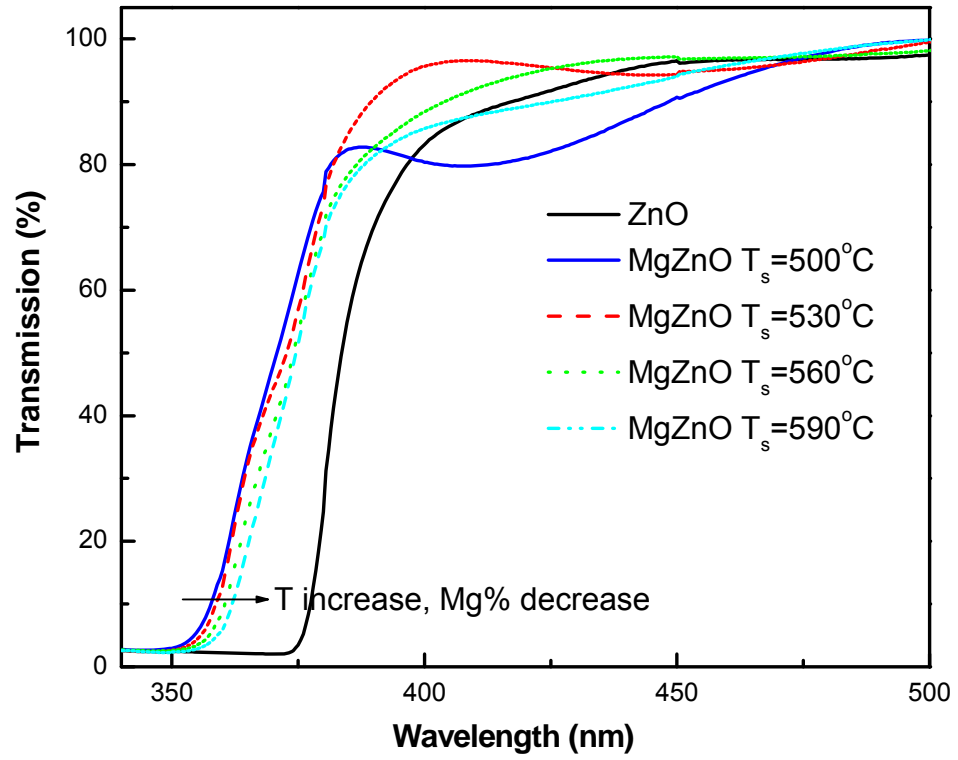


Figure 4.2 Transmission spectra of $\text{Mg}_x\text{Zn}_{1-x}\text{O}$ nanotips grown under different T_s from 500°C to 590°C . The transmission spectrum of ZnO is included as a reference.

temperature and mass, such probability of MCp_2Mg on the film surface increases more quickly than that of DEZn with the increase of T_s , leading to a reduced Mg content. Based on these results, the optimized T_s for $\text{Mg}_x\text{Zn}_{1-x}\text{O}$ nanotips should be in the range of 530°C - 560°C .

4.1.2 O/Zn precursors flow rate ratio

The VI/II flow rate ratio, i.e. O/Zn ratio, is reported to be a critical factor for determining the growth mode of ZnO in the MOCVD system^[103]. In this dissertation work, however, precursors Zn/O flow rate ratio is demonstrated to play an important role on the Mg composition during the $\text{Mg}_x\text{Zn}_{1-x}\text{O}$ nanotips growth. Theoretically, Mg composition should keep increasing with increasing the flow rate of MCp_2Mg . In real cases, however, it is limited by the O/Zn flow rate ratio. At a relatively low O/Zn flow rate ratio (2250/65, where 2250 and 65 represent the flow rate of O_2 and DEZn with a unit of sccm), Mg composition is limited to around 3% and the increased MCp_2Mg flow rate leads to a significant degradation of transmittance, as shown in Fig 4.3(a), implying an ineffective Mg incorporation. At a high O/Zn flow rate ratio (2250/45), Mg composition can easily go up to 6% with the increase of the Mg flow rate, shown in the Figure 4.3(b). The improvement of Mg incorporation at the relatively high O/Zn flow rate ratio may be explained as follows. Under fixed other growth conditions, the flow rate of DEZn determines the growth rate of $\text{Mg}_x\text{Zn}_{1-x}\text{O}$ nanotips since the Mg incorporation is low and the growth rate is mainly determined by the reaction rate of Zn species. A lower ZnO growth rate at a lower Zn flow rate (45 sccm) provides Mg species higher reaction probability with O and results in longer diffusion time of Mg atom to find its stable posit-

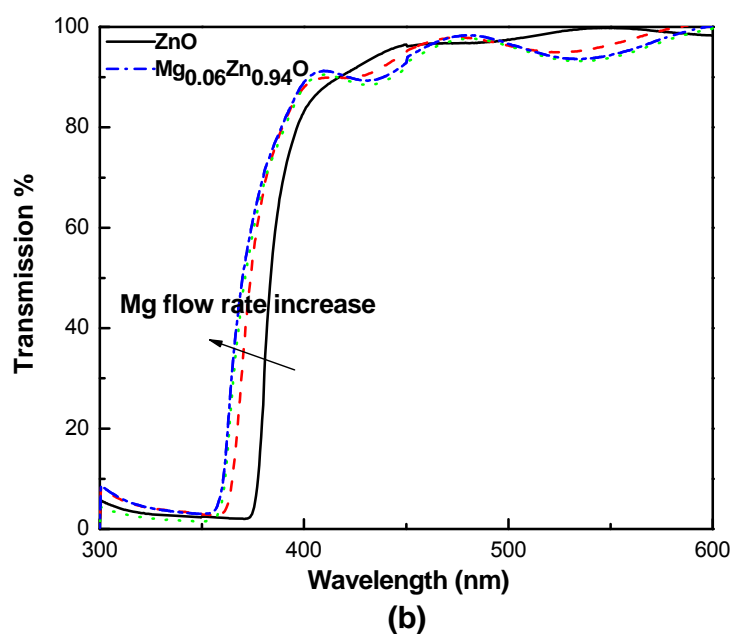
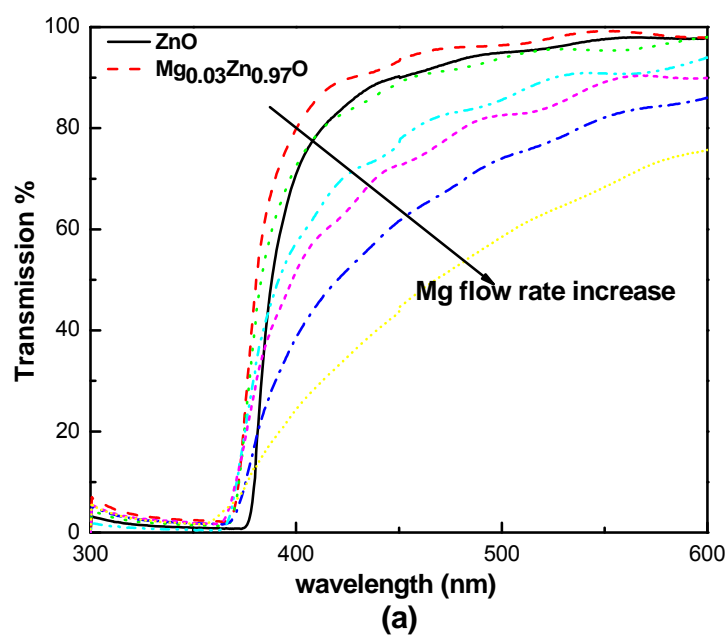


Figure 4.3 Transmission spectra of $\text{Mg}_x\text{Zn}_{1-x}\text{O}$ nanotips grown with different O/Zn precursors flow rate ratios. (a) O/Zn flow ratio is 2250/65; (b) O/Zn flow ratio is 2250/45.

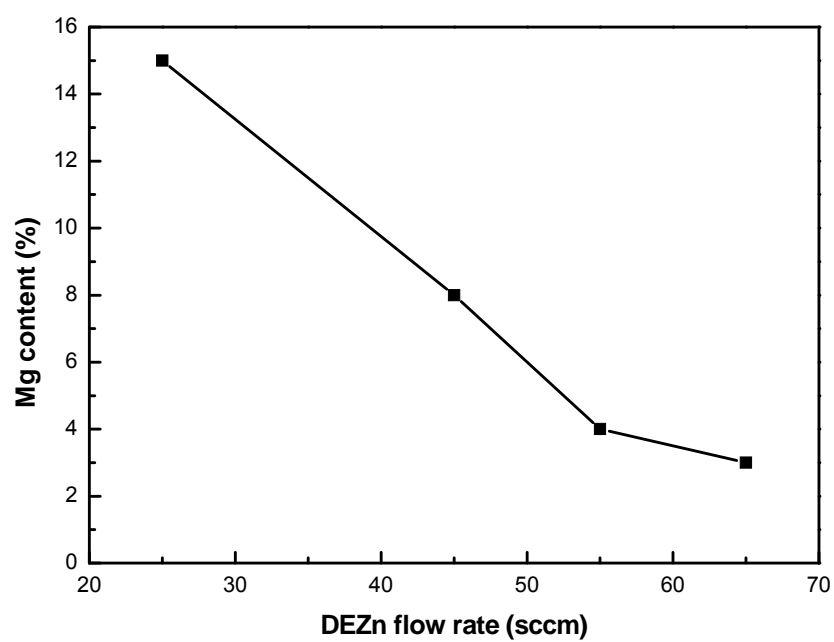


Figure 4.4 Relationship between the maximum Mg incorporation and the flow rate of DEZn, under the fixed O₂ flow rate (2250 sccm).

ion in the wurtzite ZnO lattice and thus higher Mg incorporation. The maximum Mg composition (i.e. limitation) of $\text{Mg}_x\text{Zn}_{1-x}\text{O}$ nanotips obtained at each different DEZn flow rate was shown in Fig. 4.4.

4.1.3 Chamber pressure

The chamber pressure is another sensitive factor, which impacts the Mg incorporation as well as the surface morphology. It has been reported that the vertical growth rate is higher than the lateral growth rate under a high chamber pressure (~ 200 torr) while a better tendency of lateral growth happens under a low chamber pressure (~ 30 torr) ^[104]. For the growth of 1-D $\text{Mg}_x\text{Zn}_{1-x}\text{O}$ nanostructures, therefore, we expect to use a relatively high chamber pressure to maintain a fast growth rate along the vertical direction. However, the chamber pressure cannot be too high since the probability of gas phase reaction also increases with the chamber pressure, which results in a very bad surface morphology and hence a great degradation of optical properties. Through varying the chamber pressure from 40 torr to 110 torr, we found an optimum chamber pressure (~ 60 torr) for good $\text{Mg}_x\text{Zn}_{1-x}\text{O}$ nanotips. It was also found the Mg incorporation varied with the chamber pressure. A little bit increase of Mg incorporation was found when the chamber pressure changed from 50 torr to 90 torr. It could be explained as that higher chamber pressure reduces the mean free path of Mg species and increases their reaction probability with O and thus results in higher Mg incorporation.

4.1.4 Buffer layers

A buffer layer is usually used in the film growth to modify quality of the film/substrate interface, the surface morphology, structural and crystalline properties and even optical and electrical properties of the film. Among almost all ZnO-based films or nanostructures, two different types of ZnO buffer layers are mainly used for improving the quality of the main layer, which are low-T buffer layers and high-T buffer layers^[105]. The low-T buffer can reduce the stress and strain caused by the thermal expansion coefficients difference and lattice mismatch between substrates and films^[105, 106], while the high-T buffer is usually used to produce high crystalline seed layers or template for the subsequent low temperature growth^[107, 108]. In our own work of $\text{Mg}_x\text{Zn}_{1-x}\text{O}$ thin films grown on r-plane sapphires^[19, 58], a high-T thin ZnO buffer layer is used to achieve high-quality films and the thin ZnO buffer acts as a crystalline template and restricts diffusion of Mg into the sapphire substrate. For the $\text{Mg}_x\text{Zn}_{1-x}\text{O}$ nanotips growth, we found a buffer layer is also needed. Figure 4.5 (a) shows the cross-view SEM image of the $\text{Mg}_{0.07}\text{Zn}_{0.93}\text{O}$ sample grown on Si substrates without a buffer layer, from which a column structure with a rough surface is observed. This result is different from previously reported results^[5353], in which $\text{Mg}_{0.08}\text{Zn}_{0.92}\text{O}$ nanowires were successfully grown on Si substrates without using any buffer, and Zn-rich and Mg-rich regions were automatically formed during the initial growth and those phase separated seed layers induced the growth of nanowires.

In order to investigate the influence of the buffer layer on the growth of $\text{Mg}_x\text{Zn}_{1-x}\text{O}$ nanotips, we initially grew a thin (~ 30 nm) ZnO buffer layer at low temperature (LT) ($\sim 300^\circ\text{C}$), a thin MgZnO buffer layer at LT ($\sim 300^\circ\text{C}$), and a thin ZnO buffer at high T (HT) ($\sim 520^\circ\text{C}$), respectively, on Si substrates before the $\text{Mg}_x\text{Zn}_{1-x}\text{O}$ nanotips growth. These

three different types of buffer layers resulted in three different kinds of morphology of $\text{Mg}_x\text{Zn}_{1-x}\text{O}$ nanotips, shown in the Fig. 4.5 (b)-(d). It is seen that good $\text{Mg}_x\text{Zn}_{1-x}\text{O}$ nanotips only form on the HT ZnO buffer (Fig. 4.5(d)). The $\text{Mg}_x\text{Zn}_{1-x}\text{O}$ samples grown on the LT ZnO (Fig. 4.5(b)) and LT MgZnO buffer (Fig. 4.5(c)) have similar morphologies, both of which are composed of dense vertically aligned columns and appear to be dense films.

The XRD θ - 2θ scan of $\text{Mg}_x\text{Zn}_{1-x}\text{O}$ samples grown on different buffers is shown in the figure 4.6. All peaks are indexed based on the wurtzite ZnO structure. No phase separation is observed in those MgZnO samples. The $\text{Mg}_x\text{Zn}_{1-x}\text{O}$ nanotips sample grown on the high-T ZnO buffer shows a c-axis preferred orientation as expected. Only two strong peaks from (0002) and (0004) are observed, implying that the growth habit of $\text{Mg}_x\text{Zn}_{1-x}\text{O}$ ($x \sim 7\%$) nanotips keeps similar to that of ZnO nanotips (i.e. the fastest growth rate along c-axis). As comparison, the $\text{Mg}_x\text{Zn}_{1-x}\text{O}$ samples grown on LT ZnO buffer and LT MgZnO buffer also show a preferential orientation along c-axis. But the presence of other peaks from (10-10), (10-12) and (10-13) confirms the polycrystalline structure of these two samples.

4.1.5 Growth mechanism

Based on the conventional nucleation and growth theory, as-arrived adatoms would find preferential sites on the surface of substrates to form the nucleation sites in the beginning of growth, and those sites would grow up with a continuous sources supply to form films or nanostructures. A 3-D island growth mode (*Volmer-Weber* or VM mode) is proposed to explain the nanotips or nanorods or nanowires growth, where the nucleation islands in the initial growth are desirable to form the 1-D nanostructures. In our $\text{Mg}_x\text{Zn}_{1-x}\text{O}$ nanotips growth, a high-T ZnO buffer layer is believed to induce the VM growth mode in

the first stage of the growth and play a critical role on the formation of $\text{Mg}_x\text{Zn}_{1-x}\text{O}$ nanostructures. The growth mechanism can be proposed as follows.

ZnO nanowires are easily grown on the Si substrates. Due to big lattice mismatch between ZnO and Si, Zn- and O- reactive adatoms randomly migrate on the surface of Si substrates during the initial growth and easily agglomerate together to form the nucleation islands at a high temperature. These nucleation islands will grow up quickly along the c-axis orientation because of the native growth habit of ZnO (i.e. the big surface energy of c-plane makes it preferentially covered by adatoms). With the continuous growth, the growing nucleation islands become more and more separate, which provide preferential nucleation sites to the subsequent MgZnO nanotips growth. Since the Mg and Zn metal adatoms have different adsorption energy, Mg incorporation in ZnO will definitely disturb the surface migration of Zn-O adatoms and hence the growth habit of ZnO. Besides that, Mg incorporation reduces the surface energy anisotropy of ZnO ^[68] and thus reduces the growth rate along c-axis. As a result, the $\text{Mg}_x\text{Zn}_{1-x}\text{O}$ nanotips growth becomes more and more difficult with increasing Mg composition even with a high T ZnO buffer layer. So far, the maximum Mg composition we obtained on $\text{Mg}_x\text{Zn}_{1-x}\text{O}$ nanotips grown on Si substrates is ~15%.

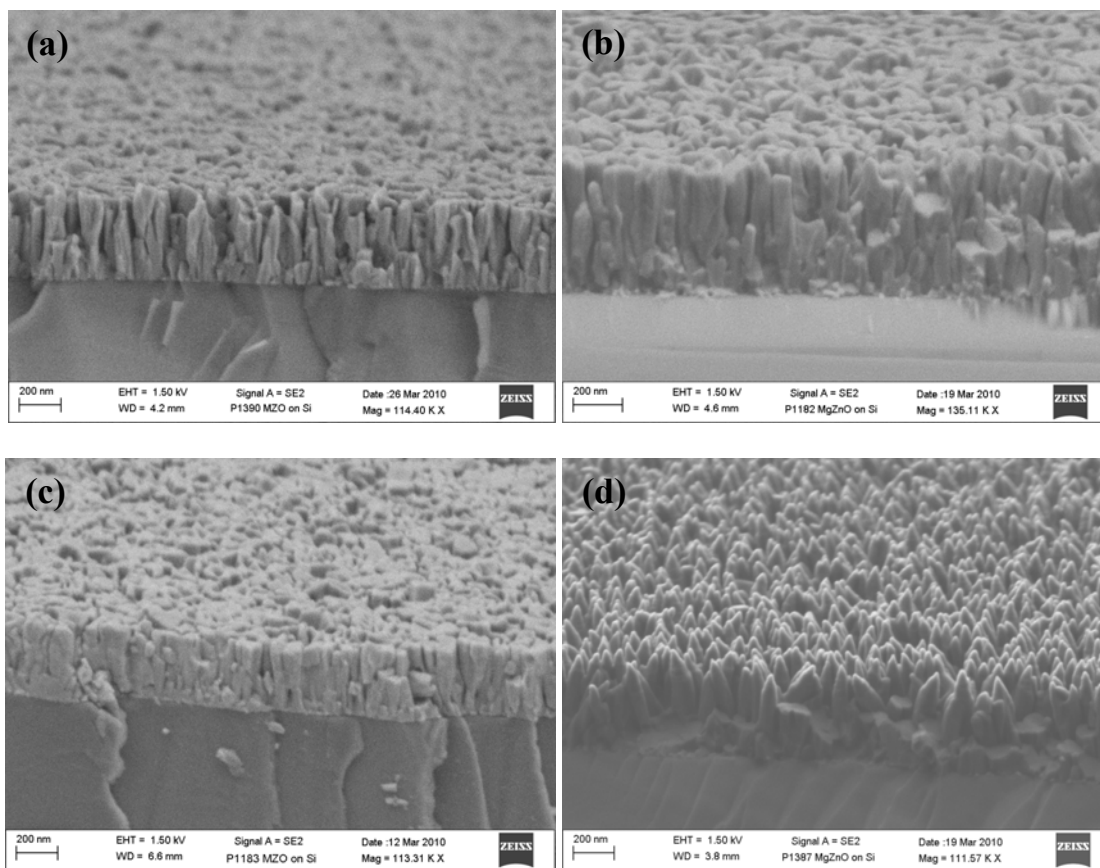


Figure 4.5 FESEM images of $\text{Mg}_x\text{Zn}_{1-x}\text{O}$ ($x \sim 7\%$) samples grown on different buffer layers.

(a) no buffer; (b) a LT ZnO buffer; (c) a low-T MgZnO buffer; (d) a high-T ZnO buffer.

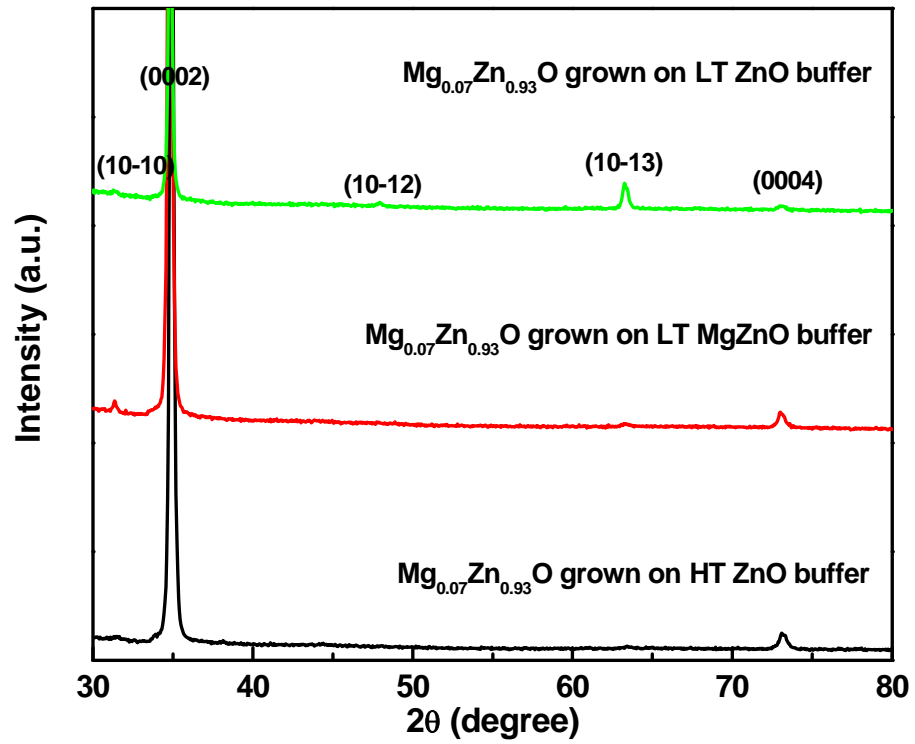


Figure 4.6 XRD patterns of $\text{Mg}_{0.07}\text{Zn}_{0.93}\text{O}$ samples grown on different buffer layers.

4.2 Optimization of $\text{Mg}_x\text{Zn}_{1-x}\text{O}$ nanotips growth on GZO films

With the optimization of $\text{Mg}_x\text{Zn}_{1-x}\text{O}$ nanotips growth on Si substrates, 1-D $\text{Mg}_x\text{Zn}_{1-x}\text{O}$ nanostructures are also grown on GZO films for photovoltaics. Because of the limitation of soften point of glass ($\sim 550^\circ\text{C}$), we chose a T_s of 530°C and use a HT ZnO buffer ($\sim 30\text{-}50\text{ nm}$) for the $\text{Mg}_x\text{Zn}_{1-x}\text{O}$ nanostructures growth. Figure 4.7 (a)-(e) show the cross-section FESEM images of 1-D $\text{Mg}_x\text{Zn}_{1-x}\text{O}$ ($0 \leq x \leq 0.10$) nanostructures ($200\text{-}600\text{ nm}$) on GZO films. All $\text{Mg}_x\text{Zn}_{1-x}\text{O}$ ($x \leq 0.1$) nanostructures appear to be nanotips/nanorods aligned perpendicular to the GZO surface. The aspect ratio of nanotips/nanorods reduces from 7:1 to 2:1 with increasing Mg content from 0 to 0.1. The reduced aspect ratio has been reported on $\text{Mg}_x\text{Zn}_{1-x}\text{O}$ nanorods grown on Si substrates^[69], which could be explained in terms of the surface energy change caused by Mg incorporation into ZnO. As the Mg composition increases beyond 10%, the $\text{Mg}_x\text{Zn}_{1-x}\text{O}$ changes from the 1-D nanostructure into 2-D film (Fig. 4.7(f)), resulted from the reduced surface energy anisotropy^[68].

Figure 4.8 shows the transmission spectra of $\text{Mg}_x\text{Zn}_{1-x}\text{O}$ nanostructures with different Mg%. All $\text{Mg}_x\text{Zn}_{1-x}\text{O}$ samples show high transmission ($>80\%$) in the visible region. The absorption edge has a blue-shift with the increase of Mg%, showing the bandgap increase. The high transmittance with a shorter absorption wavelength makes $\text{Mg}_x\text{Zn}_{1-x}\text{O}$ more advantageous than ZnO to be used as a window layer in solar cells since the overall efficiency could be improved by less absorption loss.

For ZnO nanostructures grown on GZO films^[90, 102], large surface energy anisotropy of ZnO and relatively high growth temperature are the key factors for growth of 1-D nanostructures. Although GZO film is polycrystalline, lots of nucleation sites such as surface defects, and Ga atoms *etc.* would make adatoms coalesce into 3D nuclei that

facilitate fast growth along c-axis direction, forming 1-D nanostructures (Fig. 3.10(a)). As Mg is introduced for growth of $\text{Mg}_x\text{Zn}_{1-x}\text{O}$, the adatoms diffusion and nucleation become complicated. It is found that it is difficult to grow 1-D $\text{Mg}_x\text{Zn}_{1-x}\text{O}$ nanostructures directly on GZO films without using buffer layers. The HT ZnO buffer serves as a nanostructured template formed on the GZO film, and then the $\text{Mg}_x\text{Zn}_{1-x}\text{O}$ adatoms would follow the crystallographic alignment to grow into 1-D nanostructures.

It is still a challenge to achieve good 1-D $\text{Mg}_x\text{Zn}_{1-x}\text{O}$ nanostructures with high aspect ratio and high Mg content ($>10\%$). The reasons could be attributed to two aspects, (i) the intrinsic low surface energy anisotropy and (ii) not well-controlled growth kinetics. The growth parameters such as substrate temperature, chamber pressure, precursor flow rates, and the buffer layer thickness will be further optimized.

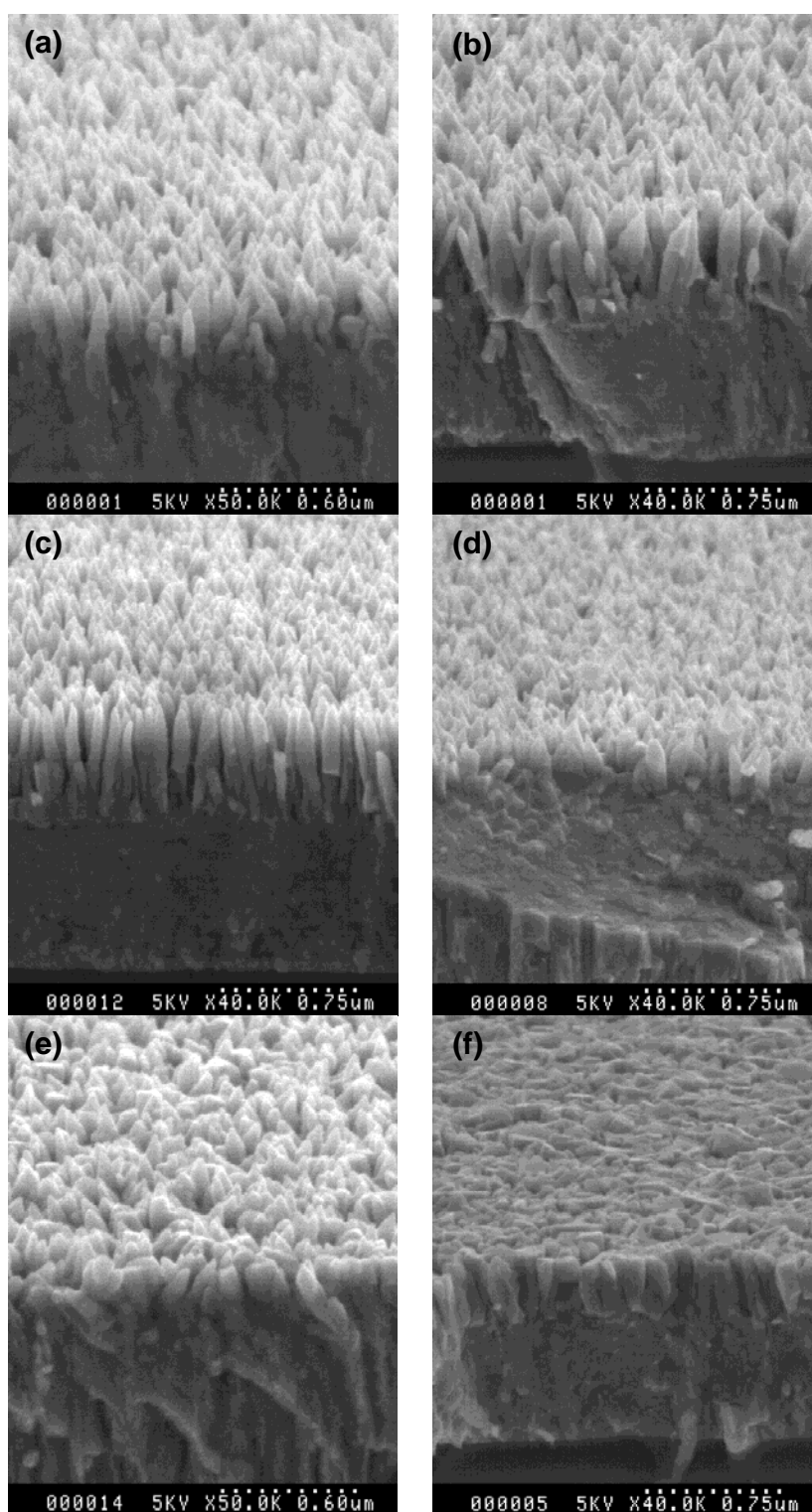


Figure 4.7 FESEM images of $\text{Mg}_x\text{Zn}_{1-x}\text{O}$ nanostructures on GZO films with (a) $x=0$, (b) $x=0.04$, (c) $x=0.06$, (d) $x=0.08$, (e) $x=0.10$ and (f) $x=0.12$.

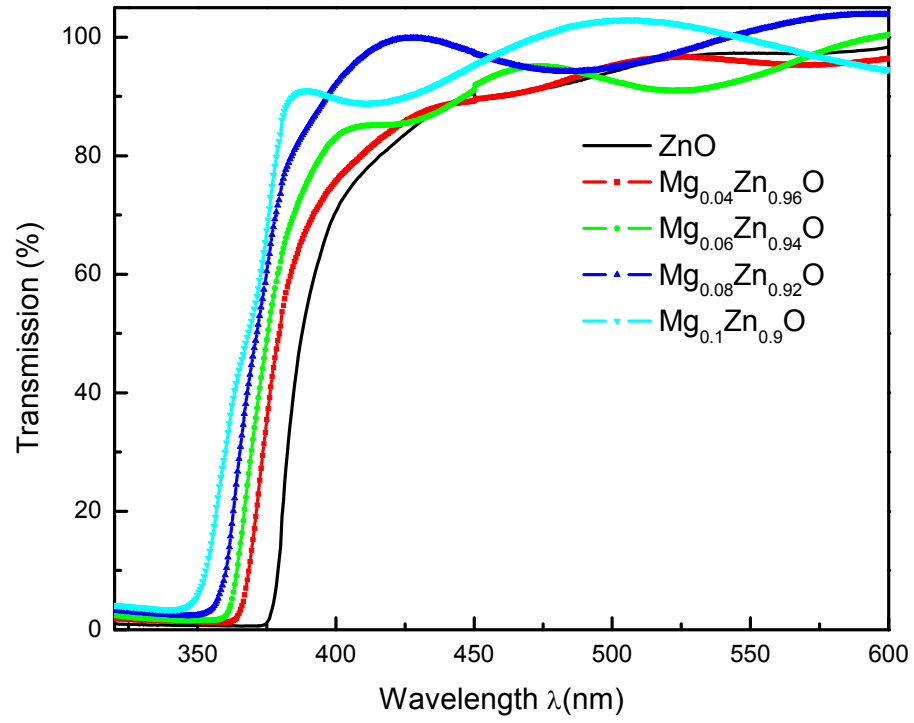


Figure 4.8 Transmission spectra of 1-D $\text{Mg}_x\text{Zn}_{1-x}\text{O}$ ($0 \leq x \leq 0.10$) nanostructures.

4.3 Summary

In this chapter, we presented the growth optimization of 1-D $\text{Mg}_x\text{Zn}_{1-x}\text{O}$ nanostructures. The growth of $\text{Mg}_x\text{Zn}_{1-x}\text{O}$ nanotips was firstly optimized on Si substrates. The substrate temperature, chamber pressure and O/Zn precursors flow rate ratio were optimized, respectively. It is found that $\text{Mg}_x\text{Zn}_{1-x}\text{O}$ nanotips could be successfully grown at a relatively high temperature (530°C-560°C) and an optimum chamber pressure (~ 60 torr). A low Zn precursor flow rate, i.e. a relatively high O/Zn precursors flow rate ratio, was needed to achieve high Mg incorporation in $\text{Mg}_x\text{Zn}_{1-x}\text{O}$ nanotips. Besides that, a buffer layer was found to play critical role on the $\text{Mg}_x\text{Zn}_{1-x}\text{O}$ nanotips growth. A HT ZnO buffer is beneficial for the formation of $\text{Mg}_x\text{Zn}_{1-x}\text{O}$ nanotips. The ZnO buffer forms a nanostructured template at a high temperature, then serving as preferential nucleation sites to induce the sequential growth of $\text{Mg}_x\text{Zn}_{1-x}\text{O}$ nanotips.

1-D $\text{Mg}_x\text{Zn}_{1-x}\text{O}$ nanostructures were also grown on GZO films for photovoltaics. Compared to Si substrate, polycrystalline GZO film provide a more complex surface situation to the $\text{Mg}_x\text{Zn}_{1-x}\text{O}$ nanotips growth. By using a HT ZnO buffer, $\text{Mg}_x\text{Zn}_{1-x}\text{O}$ ($0 \leq x \leq 0.1$) nanotips has been successfully grown on GZO films. It is still challenging to grow $\text{Mg}_x\text{Zn}_{1-x}\text{O}$ nanotips with higher Mg composition ($>10\%$). Further optimization is needed.

Chapter 5 Photovoltaic cells fabricated on $\text{Mg}_x\text{Zn}_{1-x}\text{O}$ films and nanostructures

Due to its tunable bandgap, $\text{Mg}_x\text{Zn}_{1-x}\text{O}$ has been used in excitonic solar cells, e.g. P3HT- $\text{Mg}_x\text{Zn}_{1-x}\text{O}$ hybrid solar cells, and inorganic p-n junction thin film solar cells, e.g. CIGS solar cells, for modifying band offset between p-type semiconductor and n-type semiconductor and thus enhancing the open-circuit voltage V_{OC} of solar cells. In those photovoltaic applications, however, the morphology of $\text{Mg}_x\text{Zn}_{1-x}\text{O}$ layers was not well designed and controlled, which could limit the solar cell performances. As discussed in the chapter 1, 1-D single crystalline nanostructures are preferred in the excitonics solar cells while 2-D dense and smooth films are needed in the conventional inorganic p-n junction solar cells. We, therefore, spent much effort on controlling morphology of $\text{Mg}_x\text{Zn}_{1-x}\text{O}$ layers and put morphology-controlled $\text{Mg}_x\text{Zn}_{1-x}\text{O}$ layers into photovoltaic applications for better solar cell performances.

The growth optimization of $\text{Mg}_x\text{Zn}_{1-x}\text{O}$ 2-D polycrystalline films and 1-D nanostructures has been presented in previous chapters. In this chapter, we are going to present the preliminary results of photovoltaic solar cells fabricated on $\text{Mg}_x\text{Zn}_{1-x}\text{O}$ films and nanostructures. The unique 3-D structure, consisting of 1-D $\text{Mg}_x\text{Zn}_{1-x}\text{O}$ nanostructures and 2-D GZO films, was used in the P3HT- $\text{Mg}_x\text{Zn}_{1-x}\text{O}$ hybrid solar cells and corresponding device performances will be discussed. The $\text{Mg}_x\text{Zn}_{1-x}\text{O}$ polycrystalline film was used as the n-type counterpart, forming a heterojunction thin film solar cell with p-type Cu_2O film. The testing results will be presented. Meanwhile, the effect of Mg composition on the open-circuit voltage will be investigated.

5.1 P3HT-Mg_xZn_{1-x}O hybrid solar cells

5.1.1 Solar cell structure and operating mechanism

Figure 5.1 shows the P3HT-Mg_xZn_{1-x}O hybrid solar cell structure. 1-D Mg_xZn_{1-x}O nanostructures (~500 nm) are sequentially grown on 2-D GZO films by MOCVD, forming a unique 3-D structure. Such unique 3-D structure serve as a photoelectrode, collecting and transporting electrons generated at interface between P3HT and Mg_xZn_{1-x}O. It has some unique advantages as follows.

- (i) **Enhanced Performances:** First, 1-D Mg_xZn_{1-x}O nanotips can provide performance enhancement through light trapping, faster electron transport, larger interface area between Mg_xZn_{1-x}O and P3HT and hence much photo-generated charges. Second, ZnO nanotips and GZO films are from the same material system. GZO offers very low contact potential to ZnO and thus favors the electron injection. The fast photoresponse speed can be achieved.
- (ii) **Enhanced Manufacturability and Reduced Cost:** ZnO is a low cost, non-toxic, environment-friendly material. In contrast to the ITO or FTO, GZO possesses similar electrical and optical properties to ITO and FTO but additional advantages such as low cost, non-toxicity, ease in doping, chemical stability in hydrogen plasma, and thermal stability. Besides that, both Mg_xZn_{1-x}O and GZO layers can be sequentially grown in one MOCVD system under low substrate temperatures (<550°C) without breaking the vacuum, which is applicable for large-scale manufacturing process.

(iii) ***Enhanced Reliability and Lifetime:*** Both GZO and $\text{Mg}_x\text{Zn}_{1-x}\text{O}$ have wide bandgap, protecting solar cells from UV degradation. UV harvesting can be used to increase cell efficiency, and enhance lifetime.

After forming above 3-D photoelectrodes, hybrid solar cells are prepared by spin coating 15g/L chloroform solution of regular P3HT (Rieke Metals E-grade) at ~ 1000 rpm onto the $\text{Mg}_x\text{Zn}_{1-x}\text{O}$ nanotips. Top contacts for hole extraction are formed by deposition of six 0.096 cm^2 and 100 nm thick silver discs on each device.

Figure 5.2 shows the band diagram of Ag-P3HT- $\text{Mg}_x\text{Zn}_{1-x}\text{O}$ -GZO hybrid solar cell, which is roughly drawn based on the theoretical values of electron affinity and bandgap of ZnO, GZO, P3HT and Ag. The main charges contributing to the photovoltaic effect are generated in the interface between $\text{Mg}_x\text{Zn}_{1-x}\text{O}$ and P3HT. Excitons created by light absorption in organic semiconductor, P3HT, do not possess enough energy to dissociate in the bulk. The big band offset (> 1.3 eV between E_C of ZnO and LUMO of P3HT) at the interface between $\text{Mg}_x\text{Zn}_{1-x}\text{O}$ and P3HT provides an exothermic pathway for dissociation of excitons. Dissociated excitons produces electrons to $\text{Mg}_x\text{Zn}_{1-x}\text{O}$ and holes in P3HT, which will transport through 1-D $\text{Mg}_x\text{Zn}_{1-x}\text{O}$ nanotips and P3HT to electrodes, respectively. $\text{Mg}_x\text{Zn}_{1-x}\text{O}$ has a wide bandgap, larger than 3.30 eV, and therefore is transparent to the visible light. The UV light with shorter wavelength than 375 nm (corresponding to an energy value of 3.30 eV) is absorbed by $\text{Mg}_x\text{Zn}_{1-x}\text{O}$, generating free electrons and holes. But they are easily recombined and would not contribute to the photocurrent too much.

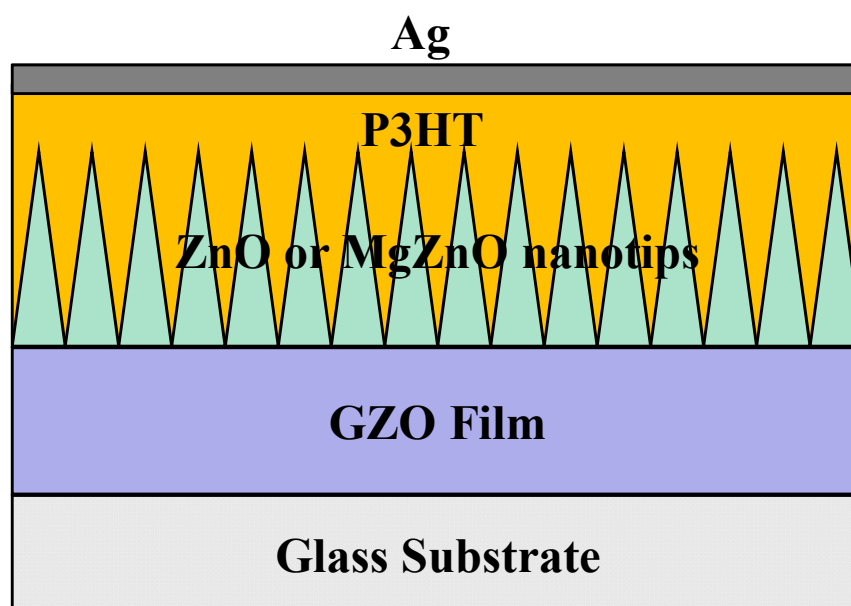


Figure 5.1 A schematic diagram of Ag-P3HT-Mg_xZn_{1-x}O-GZO/glass solar cell.

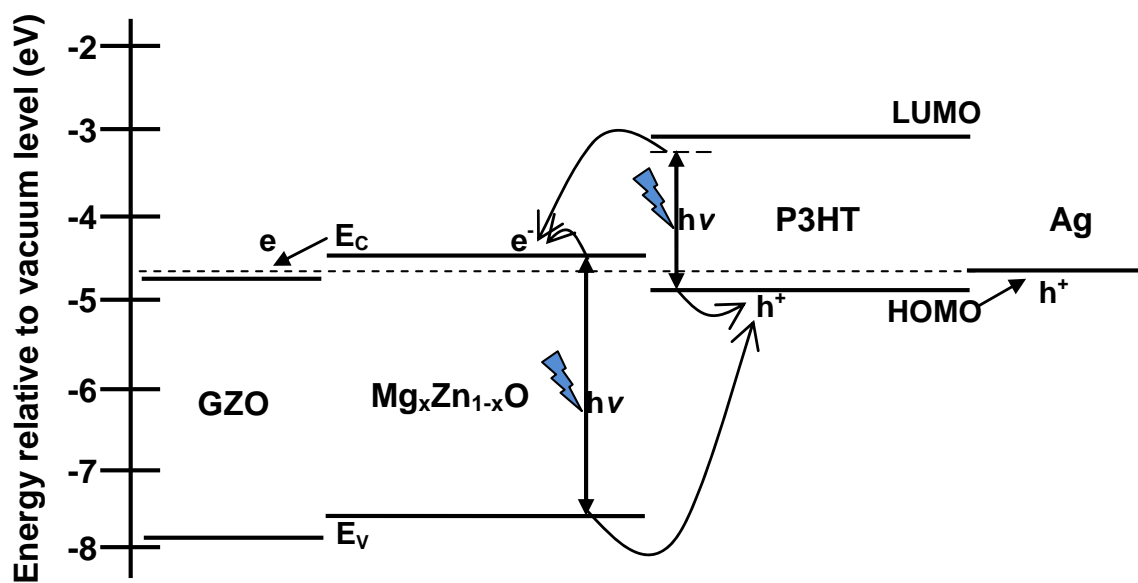


Figure 5.2 Band diagram of Ag-P3HT- $\text{Mg}_x\text{Zn}_{1-x}\text{O}$ -GZO/glass solar cell.

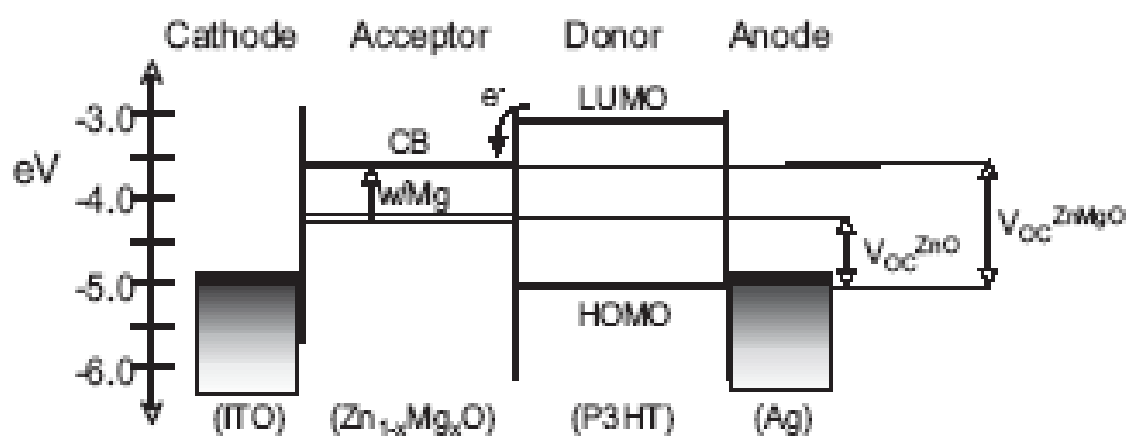


Figure 5.3 Band diagram of ITO- $\text{Mg}_x\text{Zn}_{1-x}\text{O}$ -P3HT-Ag hybrid polymer-metal oxide device, showing the effect of Mg content on the V_{OC} of the device ^[14].

Recently, $\text{Mg}_x\text{Zn}_{1-x}\text{O}$ was used in hybrid polymer-metal oxide solar cells to modify the band offset between polymer semiconductor and metal oxide semiconductor and hence to increase V_{OC} of the device^[14]. The basic idea is easily seen from Fig. 5.3, in which band diagram of ITO- $\text{Mg}_x\text{Zn}_{1-x}\text{O}$ -P3HT-Ag solar cell is shown. With the increase of Mg content in $\text{Mg}_x\text{Zn}_{1-x}\text{O}$, an increase in bandgap of $\text{Mg}_x\text{Zn}_{1-x}\text{O}$ is observed. Their research showed that much of that increase was in the conduction band just as shown in Fig. 5.3. The shift of conduction band (CB) of $\text{Mg}_x\text{Zn}_{1-x}\text{O}$ towards to the vacuum level increases the energy difference between CB of $\text{Mg}_x\text{Zn}_{1-x}\text{O}$ and HOMO of P3HT and thus enhances the V_{OC} of the solar cell. In this dissertation, an enhanced V_{OC} is expected for using $\text{Mg}_x\text{Zn}_{1-x}\text{O}$ instead of ZnO.

5.1.2 Solar cell testing system

The solar cell testing system is shown in Figure 5.4. The quantum efficiency measurements are obtained under illumination from a 150 W Xenon Light source (Oriel Q60000) passing through an Oriel Cornerstone 130 monochromator, Stanford Research SR540 light chopper, and focused on the sample with a fiber optics probe, as shown in Fig. 5.4 (a). The AC photocurrent is collected with an EG&G 5210 Lock-in amplifier. Light source power versus wavelength is calibrated using a silicon photodiode (Texas Instrument OPT101) of known responsivity. For each wavelength λ , the external quantum efficiency (EQE), also known as incident photon-to-current conversion efficiency (IPCE), is calculated from the solar cell photoresponse PR_λ according to:

$$PR_\lambda = J_\lambda / W_\lambda \quad (5.1)$$

$$EQE_\lambda = PR_\lambda hc / (q \cdot \lambda) \quad (5.2)$$

Where J_λ (mA/cm²) is the photocurrent density, W_λ (mW/cm²) is the incident light power, h is the Planck constant, q is the charge of electron and c is the speed of light.

The power conversion efficiency measurements are shown in Fig. 5.4 (b). The solar cells are directly to the light generated from the 150 W Xe light source (Oriel Q60000) filtered through an AM 1.5G filter (100 mA/cm²). A potentiostat (EG&G 273A) is connected to the device to measure the photocurrent and photovoltage. The data acquisition, monochromator control and data analysis is integrated with homemade Labview program.

For broadband variable sunlight simulated measurements, the I - V curves are recorded with an EG&G 273A potentiostat at 200 mV/s in the dark and under variable illumination intensity from a 150 W Xe light source. The light intensity is calibrated for the spectral mismatch with the AM 1.5G (100 mA/cm²) solar spectrum. For one sun conditions, the Xe light source intensity with AM 1.5G filter is adjusted and measured to be 100 mW/cm² with a Newport thermopile. The power conversion efficiency η is calculated from the equation:

$$\eta(\%) = (J_{SC}) \cdot (V_{OC}) \cdot FF / (P_{in}) \times 100\% \quad (5.3)$$

where J_{SC} (mA/cm²) is the short-circuit current density, V_{OC} (V) is the open circuit voltage, FF is the fill factor, which describes the power extraction efficiency of solar cells, and P_{in} (mW/cm²) is the overall illumination power incident on the solar cells.

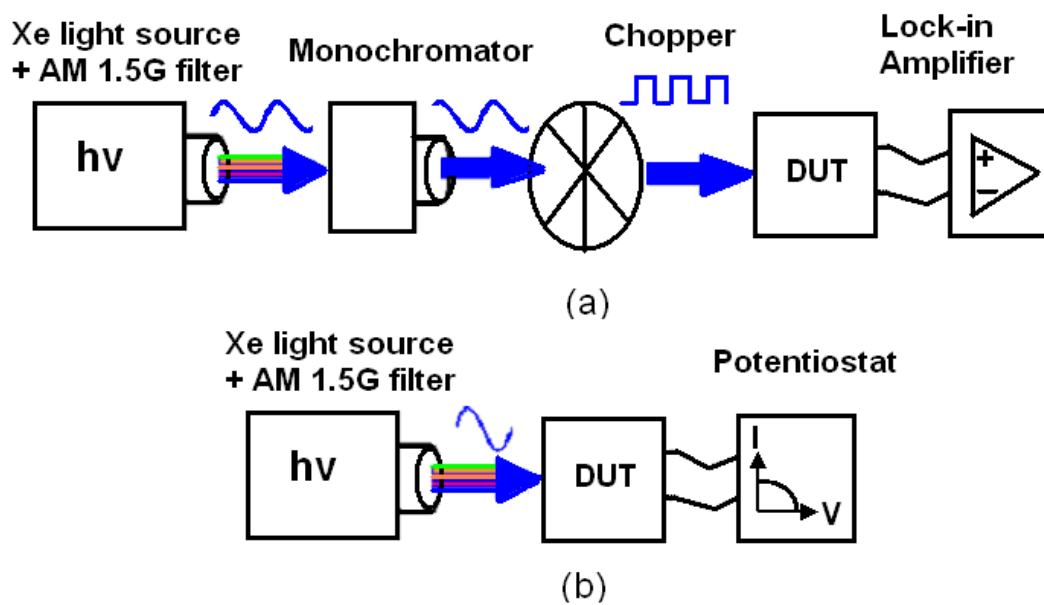


Figure 5.4 Schematic illustration of solar cell testing system, (a) quantum efficiency measurements; (b) power conversion efficiency measurements.

5.1.3 Preliminary results of solar cells

As discussed in the section 5.1.1, the Mg incorporation in $\text{Mg}_x\text{Zn}_{1-x}\text{O}$ leads to the increase of bandgap and such increase mostly happens on the conduction band, causing the increase of energy difference between E_C of $\text{Mg}_x\text{Zn}_{1-x}\text{O}$ and HOMO of P3HT and hence causing the increase of V_{OC} of the device. Figure 5.5 shows the UV-vis absorption spectra of solar cells made with ZnO, $\text{Mg}_{0.04}\text{Zn}_{0.96}\text{O}$ and $\text{Mg}_{0.05}\text{Zn}_{0.95}\text{O}$. The optical bandgap values of those 3 $\text{Mg}_x\text{Zn}_{1-x}\text{O}$ samples from UV-vis absorption spectra of the solar cells are 3.42, 3.52 and 3.60 eV, respectively. Based on the discussion above, the open-circuit voltage V_{OC} of the solar cells should increase in proportion to the increase in $\text{Mg}_x\text{Zn}_{1-x}\text{O}$ bandgap. Hence, there should be an increase of 100 mV with $\text{Mg}_{0.04}\text{Zn}_{0.96}\text{O}$, and 180 mV with $\text{Mg}_{0.05}\text{Zn}_{0.95}\text{O}$ on the solar cells V_{OC} . The predicted and measured V_{OC} values for solar cells as function of Mg contents are found to be in good agreement.

Annealing is an effective method for improving P3HT-PCBM organic photovoltaic devices^[109]. The annealing effect was also reported for ZnO-P3HT solar cells using the solution-grown ZnO nanowires impregnated with P3HT dissolved in dichlorobenzene^[110]. This effect is attributed to a rearrangement of the P3HT and PCBM nanostructure in larger clusters of improved charge mobility and light absorption, caused by the recrystallization of P3HT induced by heating beyond its glass transition temperature.

We also observe this effect in the case of P3HT- $\text{Mg}_x\text{Zn}_{1-x}\text{O}$ devices by annealing them at 150°C for 10 min in air. Annealing significantly improves the device characteristics as shown in Fig. 5.6. Several reasons can be invoked for that effect: (i) oxidation of Ag layer at the P3HT interface, which could improve its electron blocking; (ii) better impregnation

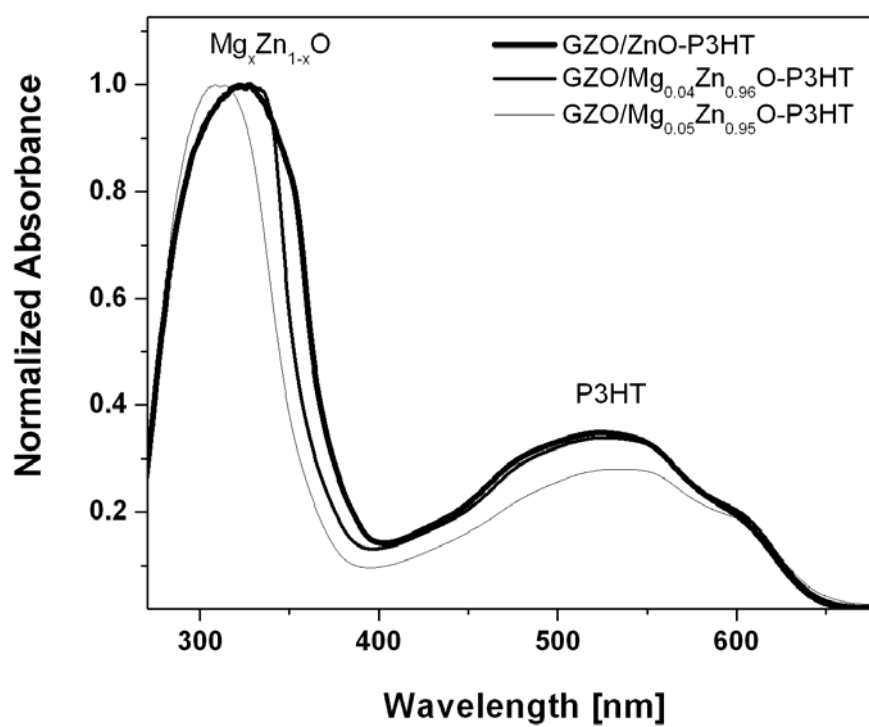


Figure 5.5 UV-vis spectra of the GZO-Mg_xZn_{1-x}O-P3HT solar cells with x= 0, 0.04, 0.05.

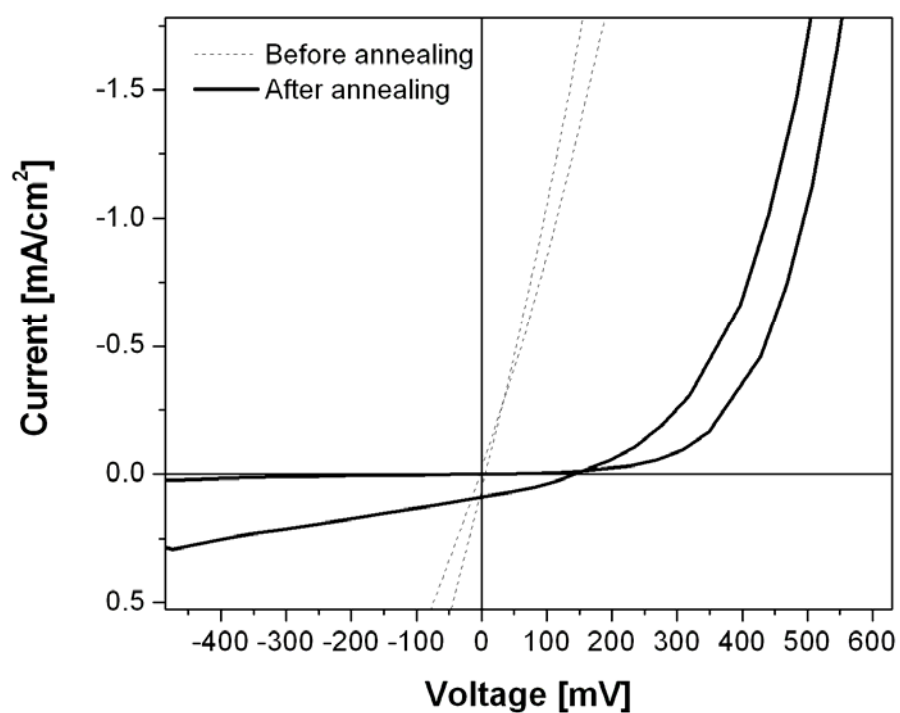


Figure 5.6 J-V curves of GZO-Mg_{0.04}Zn_{0.96}O-P3HT solar cells in the dark and under 1 sun before and after annealing.

of P3HT in the nanotips; and (iii) improvement of P3HT hole mobility by formation of more crystalline P3HT phase.

The preliminary results show that $\text{Mg}_x\text{Zn}_{1-x}\text{O}$ is promising to be used in hybrid polymer solar cells for the enhancement of V_{OC} . However, the overall solar conversion efficiency of the cells is still low because of the low fill factor (FF), low short-circuit current (I_{SC}) etc. The thickness of $\text{Mg}_x\text{Zn}_{1-x}\text{O}$ nanotips, thickness of the P3HT layer, the impregnation situation of P3HT in $\text{Mg}_x\text{Zn}_{1-x}\text{O}$ nanotips, contact quality of electrodes have to be further optimized to achieve higher solar performance.

5.2 Cu_2O - $\text{Mg}_x\text{Zn}_{1-x}\text{O}$ heterojunction thin film solar cells

It has been demonstrated that n-type ZnO and p-type Cu_2O form heterojunction solar cells, in which Cu_2O serves as the photon absorber and ZnO serves as the electron acceptor and conductor ^[9, 10]. A solar conversion efficiency of $\sim 2\%$ was recently reported for Cu_2O -ZnO solar cells ^[9]; however, it is still one order of magnitude lower than the theoretical limit of Cu_2O solar cells ($\sim 20\%$) ^[111]. The low solar conversion efficiency of Cu_2O -ZnO solar cells was attributed to the high defect density in polycrystalline Cu_2O thin films and low quality of the Cu_2O -ZnO heterojunction resulted from non-optimal deposition, and inefficient minority carrier transport caused by the planar interface structure ^[112, 113, 114, 115, 116]. Various strategies have been used to improve the solar conversion efficiency (η) of Cu_2O -ZnO heterojunctions, such as using post-deposition cyanide treatment ^[112], improving the electrical properties of Cu_2O films by optimizing deposition conditions ^[113, 10], refining deposition conditions of the ZnO layers ^[114, 115], and applying a nanowire architecture to the Cu_2O -ZnO interface ^[116]. In this dissertation,

another method to increase the efficiency of Cu_2O - ZnO solar cells is demonstrated, which is through using the ternary alloy $\text{Mg}_x\text{Zn}_{1-x}\text{O}$ to replace the ZnO , and thus to increase the open circuit voltage V_{OC} .

The effect of Mg incorporation in $\text{Mg}_x\text{Zn}_{1-x}\text{O}$ on V_{OC} of P3HT- $\text{Mg}_x\text{Zn}_{1-x}\text{O}$ hybrid solar cells has been discussed and experimentally demonstrated in last section 5.1. Different mechanisms have also been proposed to explain the enhanced V_{OC} and solar conversion efficiency of CIGS solar cells that were fabricated by using $\text{Mg}_x\text{Zn}_{1-x}\text{O}$ instead of ZnO ^[12, 13]. For Cu_2O - $\text{Mg}_x\text{Zn}_{1-x}\text{O}$ heterojunction solar cells, however, the effect of Mg incorporation on V_{OC} of solar cells is unknown. The energy band alignment of $\text{Mg}_x\text{Zn}_{1-x}\text{O}$ - Cu_2O heterojunction is unclear. In this dissertation, we try to determine the band alignment between $\text{Mg}_x\text{Zn}_{1-x}\text{O}$ and Cu_2O determined by using X-ray photoelectron spectroscopy (XPS), from which we investigate the Mg composition effect on the performance of $\text{Mg}_x\text{Zn}_{1-x}\text{O}$ - Cu_2O heterojunction solar cells.

5.2.1 Solar cell structure and fabrication

Figure 5.7 shows the structure of Cu_2O - $\text{Mg}_x\text{Zn}_{1-x}\text{O}$ heterojunction solar cells. In design of this cell structure, the deposition sequence of p- Cu_2O on ZnO films is chosen based on two considerations:

- (i) p- Cu_2O on ZnO shows smaller lattice mismatch than the inverse structure and hence lower density of interface defects and a better solar cell performance ^[117].
- (ii) This deposition sequence can avoid formation of the impurity phase CuO at the interface that usually occurs in the inverse sequence.

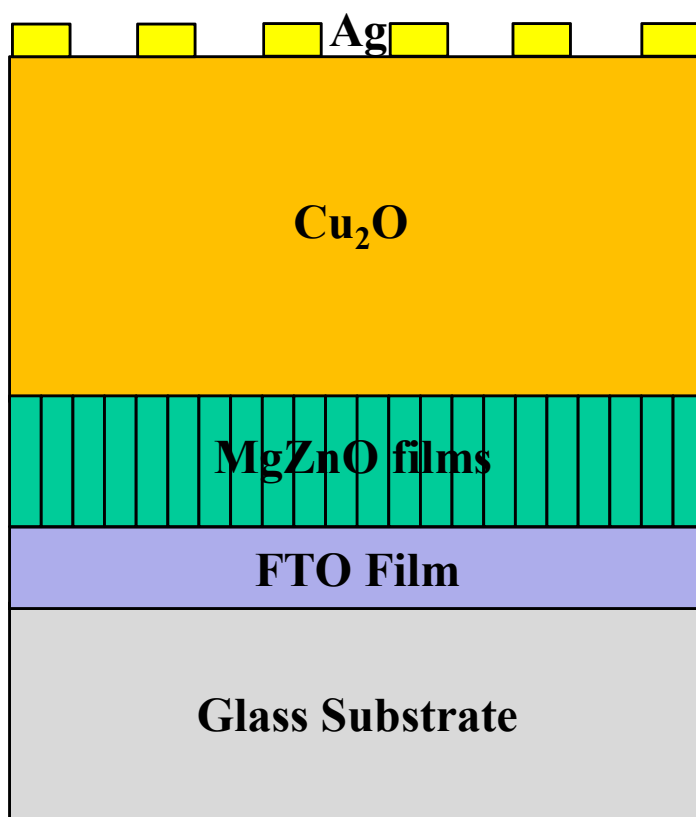


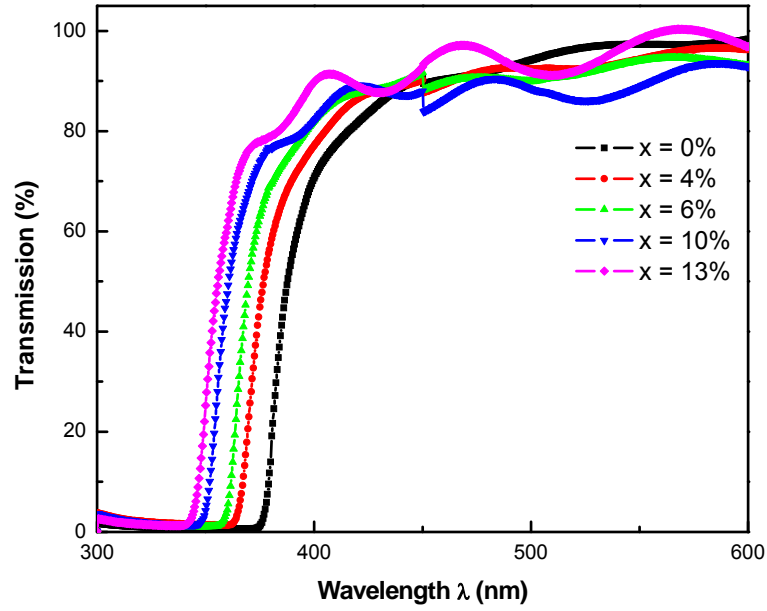
Figure 5.7 The schematic diagram of Ag- Cu_2O - $\text{Mg}_x\text{Zn}_{1-x}\text{O}$ -FTO heterojunction solar cells.

5.2.1.1 Growth of $\text{Mg}_x\text{Zn}_{1-x}\text{O}$ films

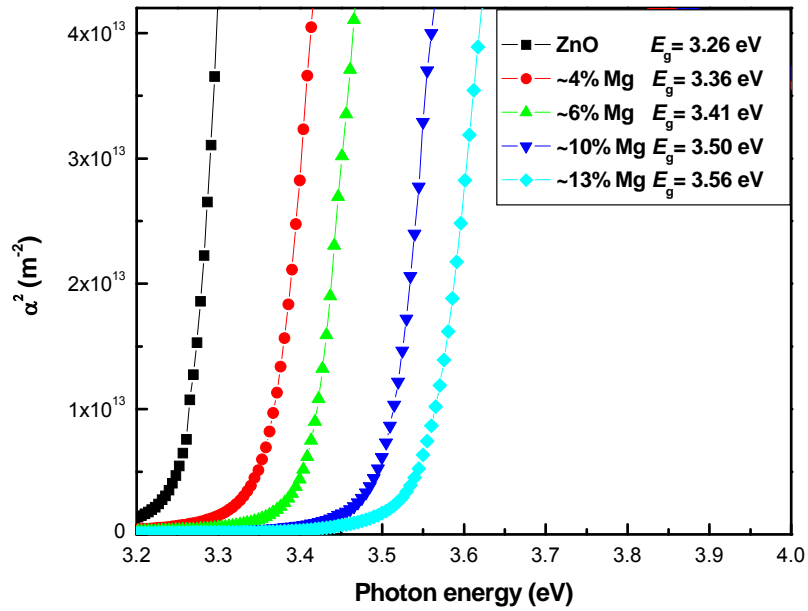
For fabricating the solar cells, $\text{Mg}_x\text{Zn}_{1-x}\text{O}$ films were firstly grown on 1''x1'' fluorine-doped tin oxide (FTO)/glass substrates (Pilkington TEC7) by the MOCVD technique at temperature of $\sim 520^\circ\text{C}$. Diethylzinc (DEZn) and Bis(methylcyclopentadienyl)magnesium (MCp_2Mg) were chosen as the Zn and Mg precursors, respectively. The Mg composition ($0 \leq x \leq 0.13$) was tuned by changing the precursor flow rate ratio ($\text{MCp}_2\text{Mg}/\text{DEZn}$). All $\text{Mg}_x\text{Zn}_{1-x}\text{O}$ films were kept ~ 600 nm thick.

The transmission spectra of $\text{Mg}_x\text{Zn}_{1-x}\text{O}$ films were measured at room temperature with a UV-visible spectrophotometer (BECKMAN DU 530), shown in Fig. 5.8(a). A transmittance of $>80\%$ in the visible light region is observed on all films, which allows most of the visible light transmitted into the light-absorber layer (Cu_2O) of solar cells. Based on the transmission data, the absorption coefficient α can be calculated from Beer's law. The bandgap values of $\text{Mg}_x\text{Zn}_{1-x}\text{O}$ films are determined by plotting the absorption coefficient α^2 as a function of photon energy ($h\nu$) and fitting these curves to the equation $\alpha = A^*(h\nu - E_g)^{1/2}$, where A^* is a frequency-independent constant, as shown in Fig. 5.8(b).

Figure 5.9(a) and (b) show the FESEM (field emission scanning electron microscopy) images of as-grown $\text{Mg}_x\text{Zn}_{1-x}\text{O}$ with $x=0$ and $x=0.1$, respectively. It is observed that the $\text{Mg}_x\text{Zn}_{1-x}\text{O}$ surface morphology evolves with increasing of the Mg composition x . During MOCVD growth, nanostructured ZnO is formed at temperature $400\text{-}500^\circ\text{C}$ ^[7373], resulting from the polarity of ZnO along $\langle 0001 \rangle$ direction. This leads to a high surface energy on $\{0001\}$ planes ^[118] and hence a fast growth rate along the c-axis ^[119]. With the Mg incorporation into ZnO, however, this polarity is weakened, leading to the reduction of the anisotropy of surface energy among all ZnO planes ^[68]. The growth rates along a- and



(a)



(b)

Figure 5.8 (a) Transmission spectra of $\text{Mg}_x\text{Zn}_{1-x}\text{O}$ ($0 \leq x \leq 0.13$) films, (b) Plots of α^2 versus $h\nu$ for $\text{Mg}_x\text{Zn}_{1-x}\text{O}$ ($0 \leq x \leq 0.13$) films.

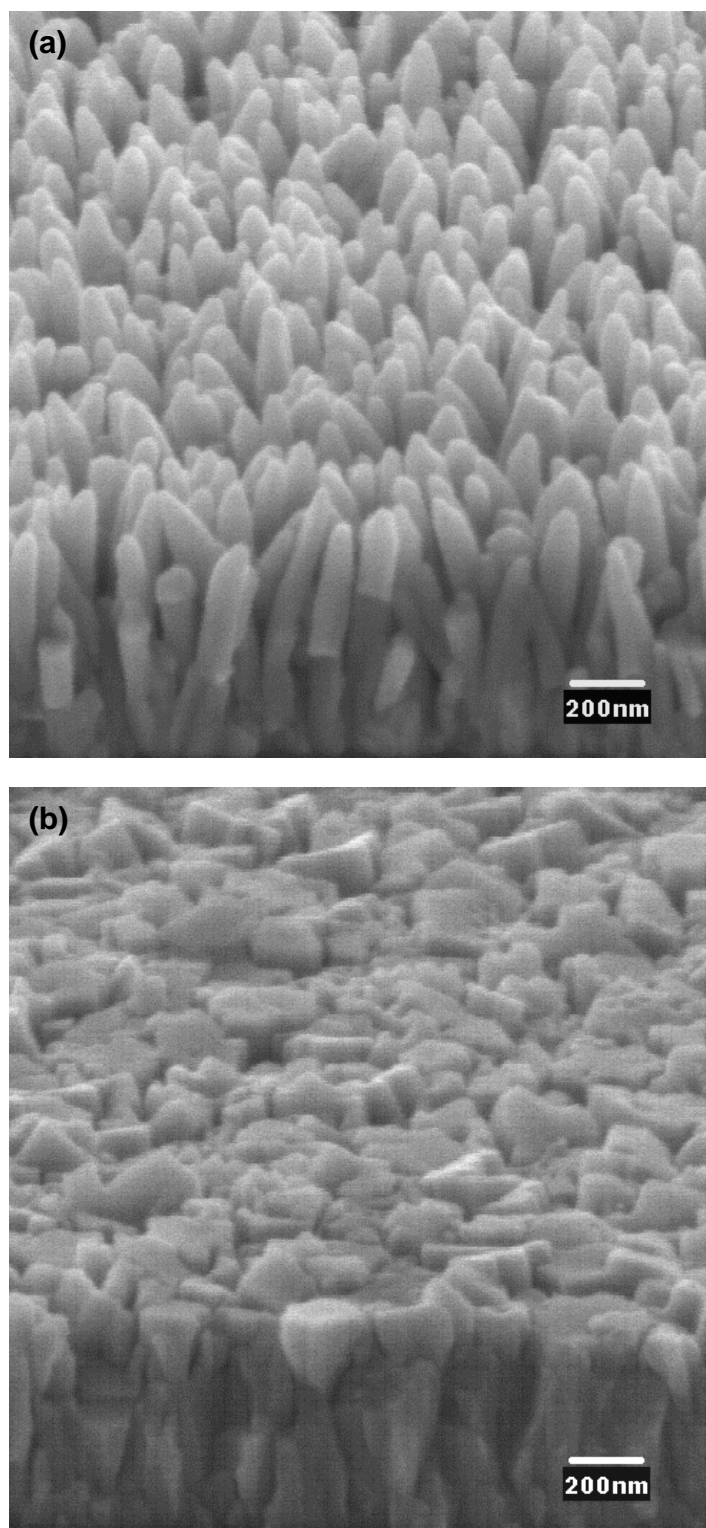


Figure 5.9 FESEM images of as-grown $\text{Mg}_x\text{Zn}_{1-x}\text{O}$ layers with (a) $x = 0$ and (b) $x = 0.10$.

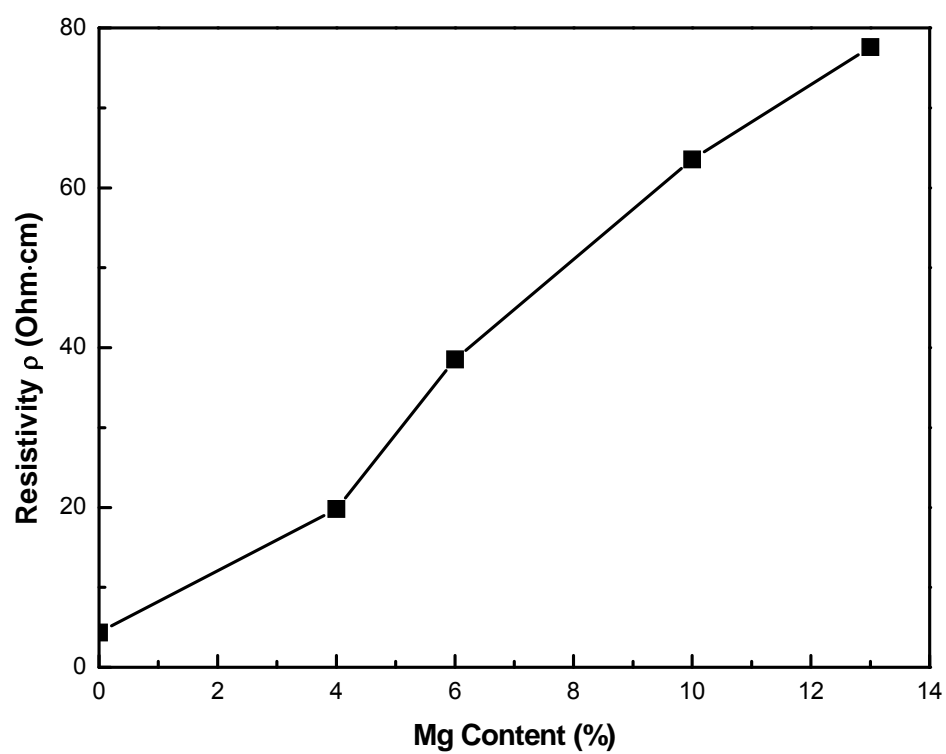


Figure 5.10 Resistivity of $\text{Mg}_x\text{Zn}_{1-x}\text{O}$ ($0 \leq x \leq 0.13$) films as a function of Mg content (x).

b-axis would increase, while that along the c-axis decreases. As a result, the morphology of $\text{Mg}_x\text{Zn}_{1-x}\text{O}$ changes from sharp nanotip arrays to dense columns with increasing x , as shown in Fig. 5.9(a) and (b).

The electrical properties of $\text{Mg}_x\text{Zn}_{1-x}\text{O}$ films were characterized by Hall measurements on the Van der Pauw patterns. Figure 5.10 shows the resistivity of $\text{Mg}_x\text{Zn}_{1-x}\text{O}$ ($0 \leq x \leq 0.13$) films as a function of Mg content (x). It is seen that the resistivity of $\text{Mg}_x\text{Zn}_{1-x}\text{O}$ films increases with Mg content.

5.2.1.2 Deposition of Cu_2O films

Cu_2O thin films have been grown by various methods including thermal oxidation of Cu foils^[120], metal-organic chemical vapor deposition (MOCVD)^[121], sputtering^[117], and electrochemical deposition^[122]. Among them, the electrodeposition is the attractive technique because of its ability to use low-cost equipment and chemicals, large area coating, and precise control of deposition parameters.

Cu_2O films were electrodeposited from aqueous solutions of CuSO_4 ($0.4 \text{ mol}\cdot\text{L}^{-1}$) and lactic acid ($3 \text{ mol}\cdot\text{L}^{-1}$), with the pH value ~ 11 -12 controlled by NaOH. The working electrode substrates were $\text{Mg}_x\text{Zn}_{1-x}\text{O}/\text{FTO}/\text{glass}$. The counter electrode was a Cu foil. Electrodeposition was performed at a constant voltage of -0.4 V with the bath temperature of 90°C , under which a growth rate of $\sim 0.2 \mu\text{m}/\text{min}$ was obtained. The thickness of ~ 4.2 - $4.5 \mu\text{m}$ was controlled for all Cu_2O films.

Figure 5.11(a) shows the morphology of as-deposited Cu_2O film ($\sim 4.5 \mu\text{m}$ thick) on $\text{Mg}_x\text{Zn}_{1-x}\text{O}/\text{FTO}/\text{glass}$ substrates, taken by FESEM. The dense Cu_2O film shows a similar morphology to previous reports^[10, 116]. Figure 5.11(b) shows the plot of absorption

coefficient α^2 as a function of photon energy ($h\nu$), from which the bandgap of Cu_2O is determined to be 2.0 eV.

The XRD pattern of Cu_2O film is shown in Fig. 5.12, from which a polycrystalline and pure Cu_2O phase is observed. None of the other phases, such as CuO or Cu are detected although these two impurities could easily be incorporated into Cu_2O during the deposition process^[10]. XPS was used to verify the purity of Cu_2O , as shown in Fig. 5.13(a). The $\text{Cu } 2p_{3/2}$ peak is fit into a single peak at a binding energy of 932.42 eV with a FWHM of 1.27 eV as known from literature values for Cu(I) in Cu_2O ^[123]. No sub-peak at a binding energy of 933.73 eV, which is attributed to the Cu(II) in CuO , is observed. Moreover, the shake-up satellites peaks that usually appear in CuO and at a binding energy 940 eV - 945 eV^[124] are not seen in this spectrum. Another possible impurity, Cu , is not easy to quantify by XPS because the $\text{Cu } 2p_{3/2}$ peak binding energies of Cu(0) and Cu(I) are very close (~ 0.1 eV difference). But these two states can be distinguished from the $\text{Cu LMM-2 Auger transition}$ peak positions which also appear in photoemission spectra; the peak positions are 568 eV for Cu(metal) and 570 eV for Cu_2O ^[125]. In our sample, a broad peak centered at 570 eV was found, as shown in Fig. 5.13(b). Although a small peak at 568 eV is possibly buried in the broad peak, it appears that the amount of Cu is negligible.

Metal contacts (Ag) were finally deposited by a Hummer Anatech 6.6 argon plasma sputtering system. Devices were annealed for 15 minutes at 200 °C in air. J-V testing was conducted with an EG&G 273A potentiostat using the full spectrum of a xenon light source shaped with a AM1.5 filter and adjusted to 100 mW/cm^2 with a Newport thermopile.

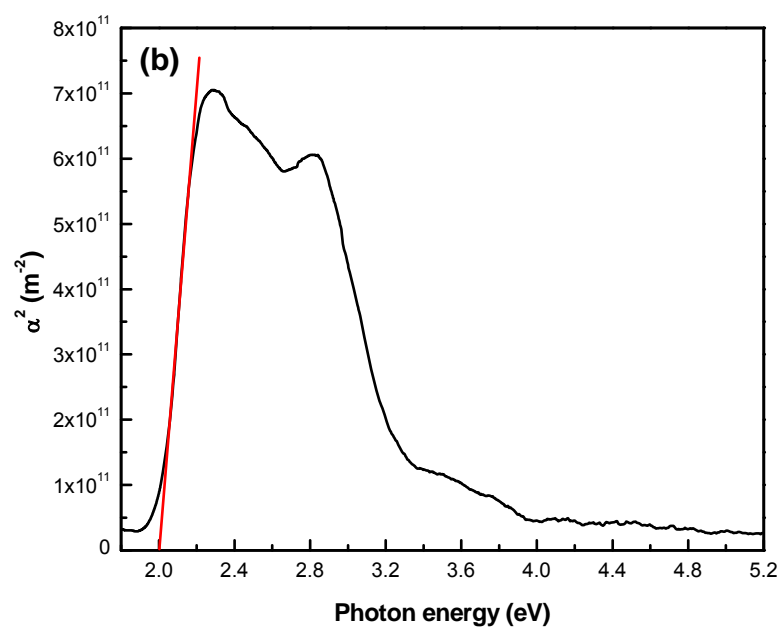
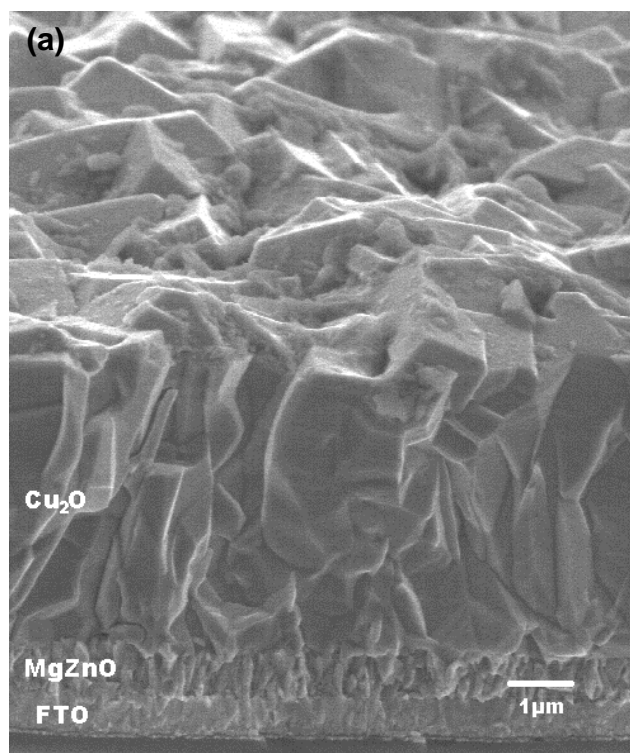


Figure 5.11 (a) an FESEM image of the Cu_2O film deposited on $\text{Mg}_{0.1}\text{Zn}_{0.9}\text{O}$ -FTO films;

(b) A plot of α^2 versus photon energy ($h\nu$) for the Cu_2O film.

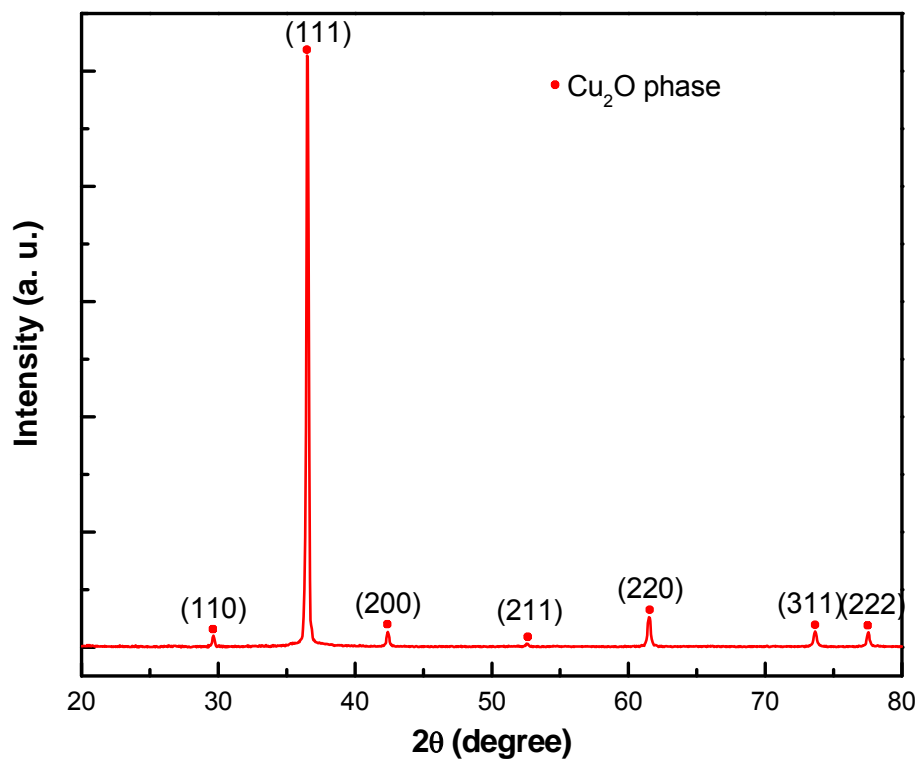


Figure 5.12 A typical XRD pattern of the Cu₂O film.

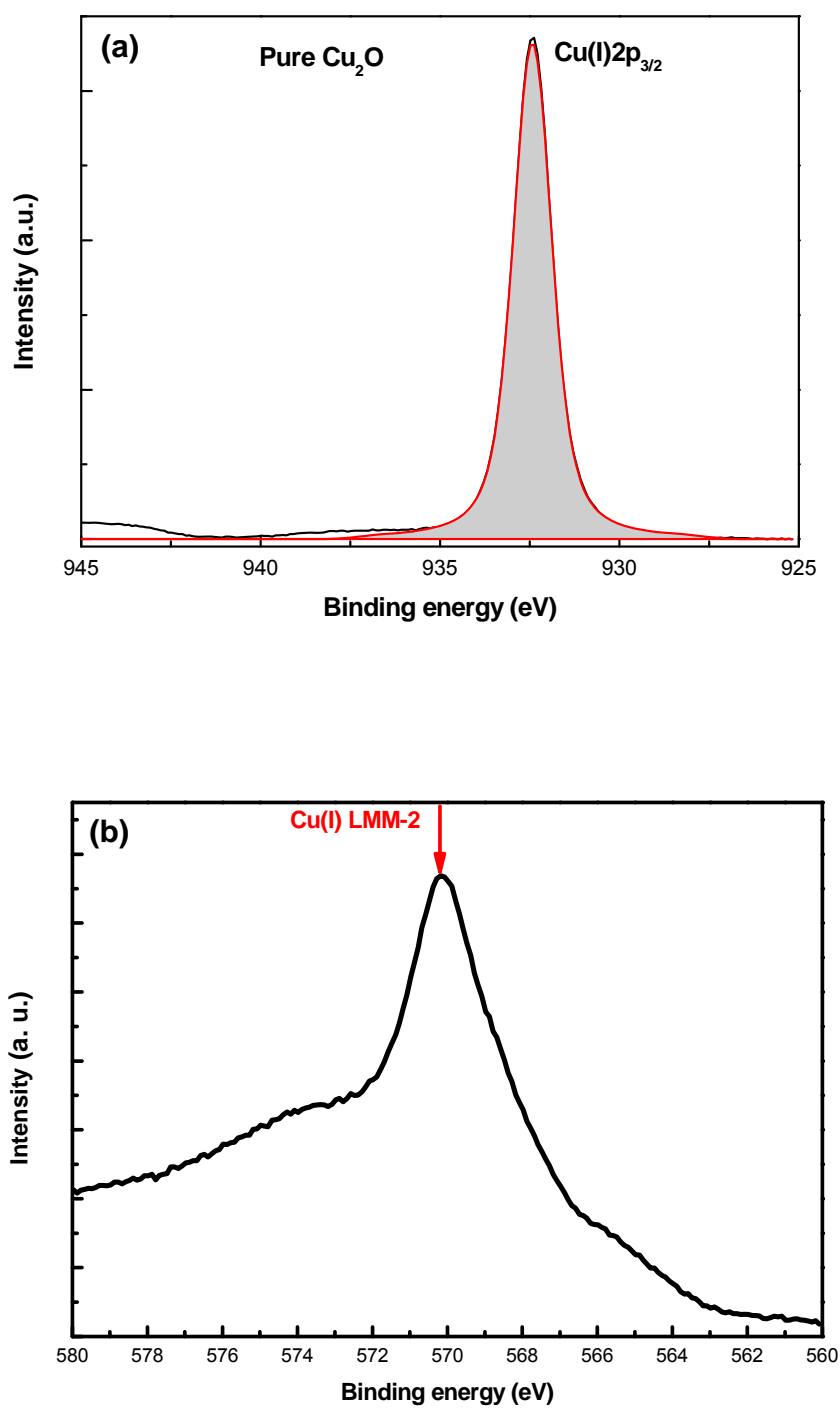


Figure 5.13 (a) The $\text{Cu } 2p_{3/2}$ XPS spectrum from a Cu_2O film; (b) Cu LMM-2 Auger peak of Cu_2O film.

5.2.2 Testing results of $\text{Cu}_2\text{O-Mg}_x\text{Zn}_{1-x}\text{O}$ heterojunction solar cells

The current density-voltage (J-V) curves of the heterojunction devices under illumination are shown in Fig. 5.14 and various parameters of the solar cells examined are listed in the Table 5.1. As expected, the V_{OC} value increases with increasing Mg content, from 251 mV for the pure ZnO-based device, up to 575 mV for the $\text{Mg}_{0.1}\text{Zn}_{0.9}\text{O}$ -based one. Besides V_{OC} , shunt resistance (R_{sh}) gets improved with increasing Mg content (x) in $\text{Mg}_x\text{Zn}_{1-x}\text{O}$, increasing from $189 \Omega\text{cm}^2$ for $x=0$ to $677 \Omega\text{cm}^2$ for $x=0.10$. Unlike the V_{OC} and R_{sh} , the short circuit current density J_{SC} stops being improved and starts to decrease as the Mg percentage increases to over 4%. The resistivity, ρ , of $\text{Mg}_x\text{Zn}_{1-x}\text{O}$ films increases with Mg content (x) from $\sim 4 \Omega\cdot\text{cm}$ ($x = 0$) to $\sim 63 \Omega\cdot\text{cm}$ for ($x = 0.1$), as shown in Fig. 5.10, resulting in an increase in the series resistance R_s (Table 1). Although R_s increases a little bit with increasing Mg content, the fill factor (FF) obtains an improvement from 0.34 ($x=0$) to 0.42 ($x=0.1$). With the improved V_{OC} , FF and R_{sh} , the solar conversion efficiency η of devices keep increasing with the increase of Mg content (x) until $x = 0.1$. The highest solar conversion efficiency was obtained on the $\text{Mg}_{0.1}\text{Zn}_{0.9}\text{O}$ sample, $\eta_{AM1.5} = 0.71 \%$, with the $J_{SC} = 3.0 \text{ mA/cm}^2$ and $V_{OC} = 575 \text{ mV}$.

Table 5.1 Photovoltaic parameters of the $\text{FTO/Mg}_x\text{Zn}_{1-x}\text{O-Cu}_2\text{O/Ag}$ solar cells with different Mg composition x examined under AM1.5 simulated sunlight

% Mg	η (%)	FF	$J_{SC}(\text{mA/cm}^2)$	$V_{OC}(\text{mV})$	$R_s(\Omega\text{cm}^2)$	$R_{sh}(\Omega\text{cm}^2)$
0	0.21	0.34	2.38	251	60	189
4	0.47	0.34	3.44	390	64	223
6	0.57	0.35	3.30	488	91	350
10	0.71	0.42	3.00	575	95	677
13	0.06	0.28	0.45	520	1077	1208

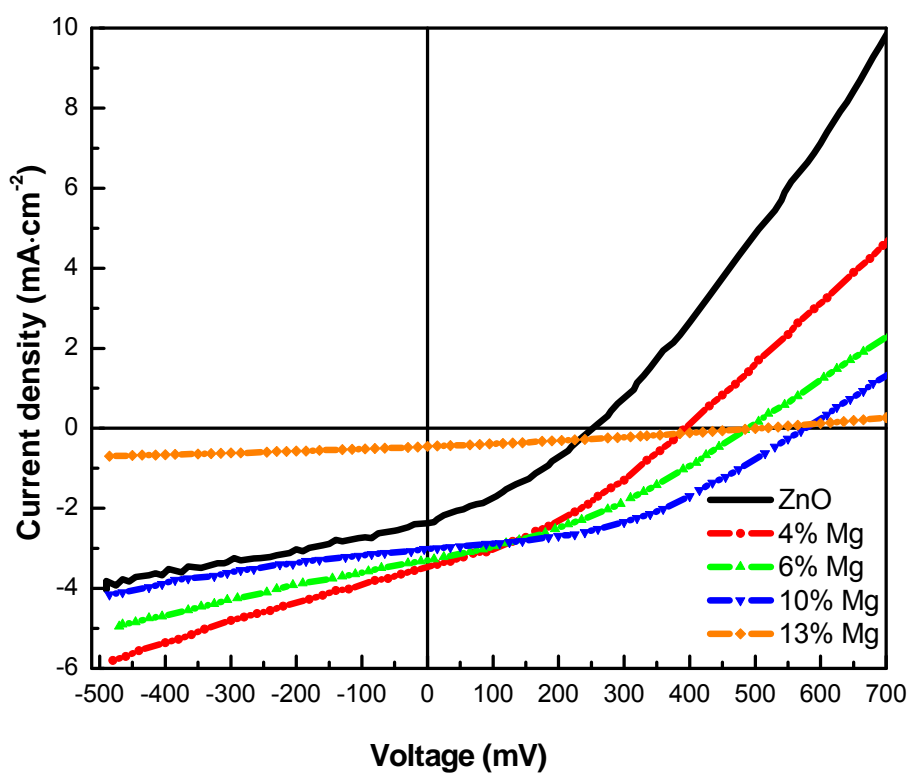


Figure 5.14 Current density (J)-voltage (V) characteristics of FTO/Mg_xZn_{1-x}O-Cu₂O/Ag solar cells under AM1.5 simulated sunlight.

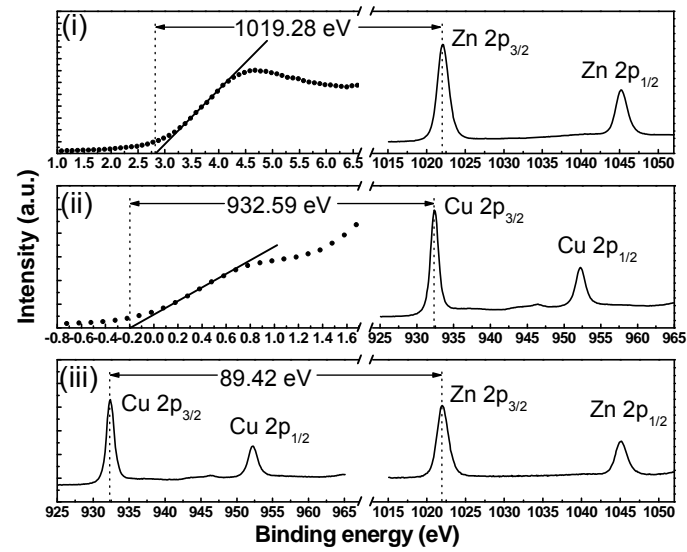
A solar cell with a higher Mg content of 13% was also fabricated. However, the electrodeposition of Cu₂O became difficult with a small deposition rate and poor control of film uniformity. The reason could be attributed to the rougher surface morphology and higher resistivity of Mg_{0.13}Zn_{0.87}O films ($\rho \sim 78 \text{ } \Omega \cdot \text{cm}$) in comparison with other Mg_xZn_{1-x}O ($x \leq 0.1$) films. As consequence, the thickness of as-deposited Cu₂O film was low ($\sim 2.5 \text{ } \mu\text{m}$), resulting in lower J_{SC} and deteriorated performances as shown in Fig. 5.14.

5.2.3 The effect of Mg composition on V_{OC}

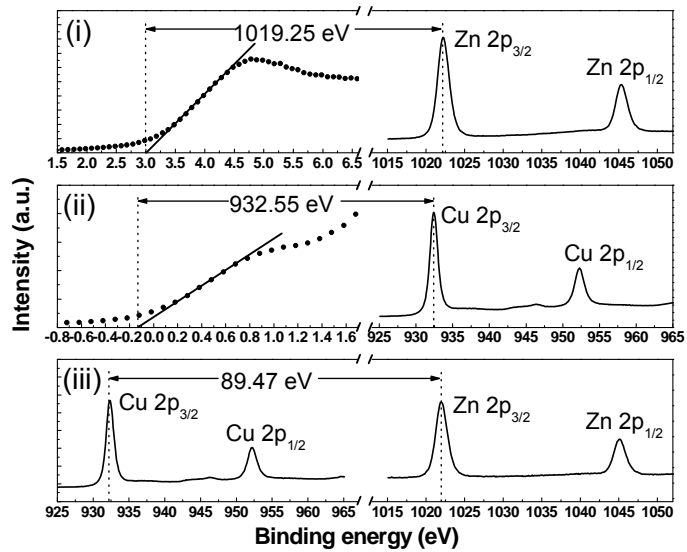
In order to understand the enhancement of V_{OC} caused by Mg incorporation in ZnO, we determined the band alignment of Cu₂O and Mg_xZn_{1-x}O using the XPS method proposed by E.A. Kraut, *et al* ^[126]. In this method, the valence band offset (VBO) ΔE_V at the Cu₂O-Mg_xZn_{1-x}O heterojunction interface is given by the following equation:

$$\begin{aligned} \Delta E_V = & (E_{\text{Zn}2p}^{\text{Mg}_x\text{Zn}_{1-x}\text{O}} - E_V^{\text{Mg}_x\text{Zn}_{1-x}\text{O}}) - (E_{\text{Cu}2p}^{\text{Cu}_2\text{O}} - E_V^{\text{Cu}_2\text{O}}) \\ & - (E_{\text{Zn}2p}^{\text{Mg}_x\text{Zn}_{1-x}\text{O}}(i) - E_{\text{Cu}2p}^{\text{Cu}_2\text{O}}(i)) \end{aligned} \quad (5.4)$$

where E_A^B refers the binding energy of core level “A” in the sample “B”, E_V^B refers the valence band maximum (VBM) and $E_A^B(i)$ represents the binding energy of core level “A” in the sample “B” at the interface. Two heterojunctions of Cu₂O-ZnO and Cu₂O-Mg_{0.1}Zn_{0.9}O were chosen for the XPS measurement. Fig. 5.15(a) shows the XPS spectra determined from the Cu₂O-ZnO heterojunction. The Cu₂O-Mg_{0.1}Zn_{0.9}O spectra are shown in Fig. 5.15(b). Based on the XPS data, the corresponding band alignments of Cu₂O-ZnO and Cu₂O-Mg_{0.1}Zn_{0.9}O heterojunctions are schematically drawn as Fig. 5.16.



(a)



(b)

Figure 5.15 XPS spectra of (a) a $\text{Cu}_2\text{O-ZnO}$ heterojunction, (b) a $\text{Cu}_2\text{O-Mg}_{0.1}\text{Zn}_{0.9}\text{O}$ heterojunction, showing the binding energy separations (i) between the Zn 2p_{3/2} core level and the VBM of bulk ZnO (a), bulk $\text{Mg}_{0.1}\text{Zn}_{0.9}\text{O}$ (b), (ii) between the Cu 2p_{3/2} core level and the VBM of a bulk Cu_2O film, and (iii) between the Zn 2p_{3/2} and the Cu 2p_{3/2} core levels at the heterojunction interface, respectively.

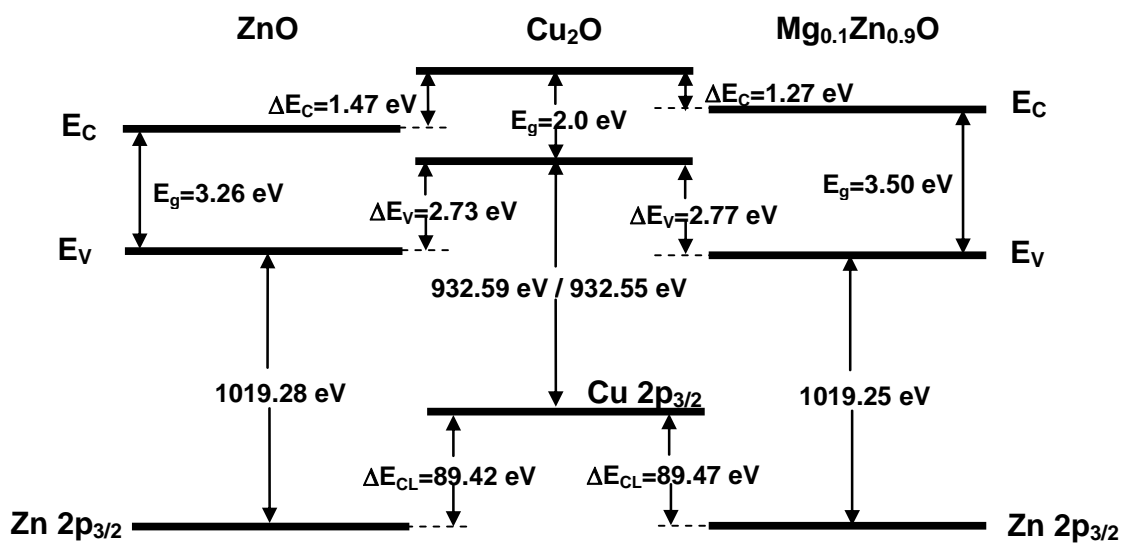


Figure 5.16 Schematic of the flat-band diagrams at the heterojunction interfaces determined from the XPS measurements. For simplicity, the Cu₂O-ZnO and Cu₂O-Mg_{0.1}Zn_{0.9}O interfaces are drawn with Cu₂O in the middle.

From Fig. 5.16, we can see the VBOs for $\text{Cu}_2\text{O-ZnO}$ and $\text{Cu}_2\text{O-Mg}_x\text{Zn}_{1-x}\text{O}$ are 2.73 eV and 2.77 eV, respectively. And the conduction band offsets (CBOs) are determined to be 1.47 eV for $\text{Cu}_2\text{O-ZnO}$ and 1.27 eV for $\text{Cu}_2\text{O-Mg}_{0.1}\text{Zn}_{0.9}\text{O}$. The 0.2 eV difference moves the conduction band of $\text{Mg}_{0.1}\text{Zn}_{0.9}\text{O}$ closer to the vacuum level compared to ZnO ; we assume that this change in conduction band edge is responsible for the enhancement of V_{OC} . It is difficult to determine the theoretical V_{OC} from this band alignment without knowing the built-in potential V_{bi} determined by the effective work function difference between p and n semiconductors. In order to roughly estimate the theoretical V_{OC} of $\text{Cu}_2\text{O-Mg}_x\text{Zn}_{1-x}\text{O}$ solar cells, we used two assumptions as follows. The first common assumption is that the built-in potential V_{bi} alone sets the upper limit to V_{OC} , which is approximately true for conventional p-n heterojunction solar cells. The second assumption is that no band bending happens in an ideal type II heterojunction under forward bias V , as shown in Figure 5.17, where V is set to V_{bi} . By assuming that the Fermi level E_{Fn} in n- $\text{Mg}_x\text{Zn}_{1-x}\text{O}$ is close to E_{Cn} (CBM in n- $\text{Mg}_x\text{Zn}_{1-x}\text{O}$), and E_{Fp} in p- Cu_2O is close to E_{Vp} (VBM in p- Cu_2O) due to the high doping level in both n and p materials, the energy difference between E_{Cn} and E_{Vp} would be approximately equal to the V_{bi} , *i.e.* the upper limit of V_{OC} . With this assumption, the upper limit of theoretical V_{OC} is estimated to be 530 mV for $\text{Cu}_2\text{O-ZnO}$ and 730 mV for $\text{Cu}_2\text{O-Mg}_{0.1}\text{Zn}_{0.9}\text{O}$, respectively.

The equivalent circuit of the solar cell is shown in Fig. 5.18. It is seen that the low shunt resistance (R_{sh}) could degrade V_{OC} significantly. R_{sh} is generally caused by parallel high-conductivity paths (PHCPs) through the solar cell, or on the edges of the cell. In our case, the interface defects and grain boundaries of both polycrystalline films in the space charge region (SCR) of the heterojunction could act as PHCPs, thus contributing to the R_{sh} .

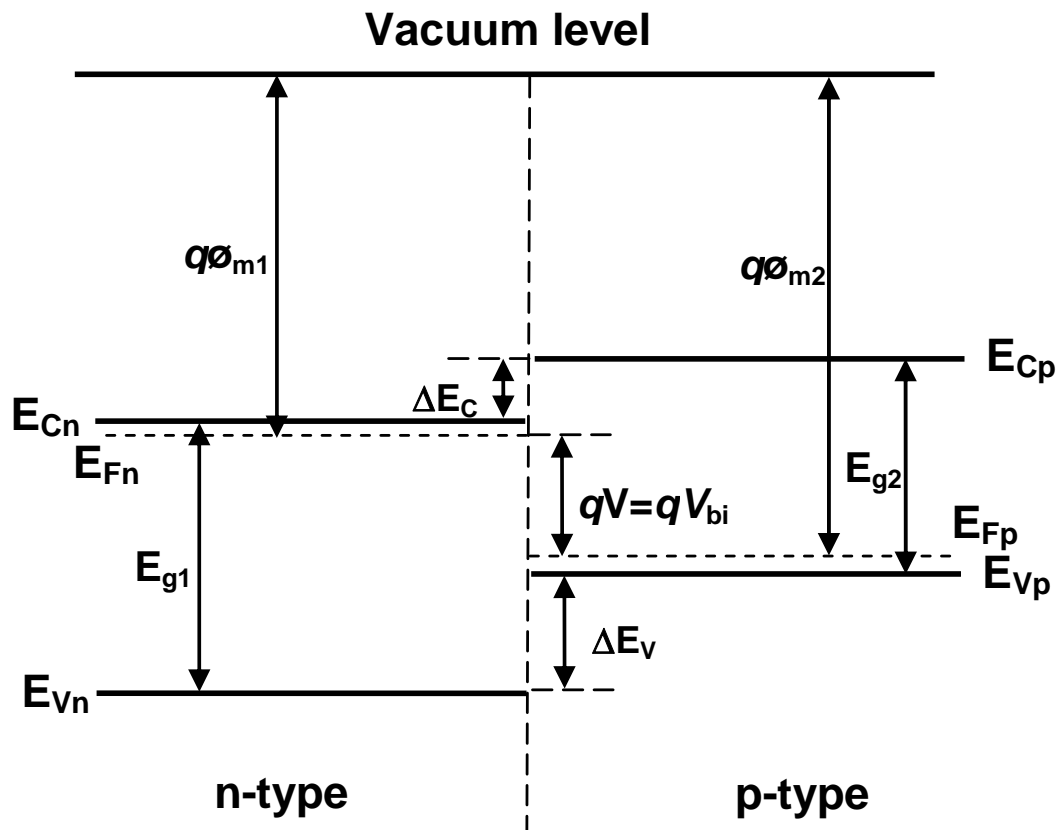


Figure 5.17 Energy-band diagrams for a p-n heterojunction with type II band alignment under forward bias V , where V is set to V_{bi} , the upper limit of V_{OC} .

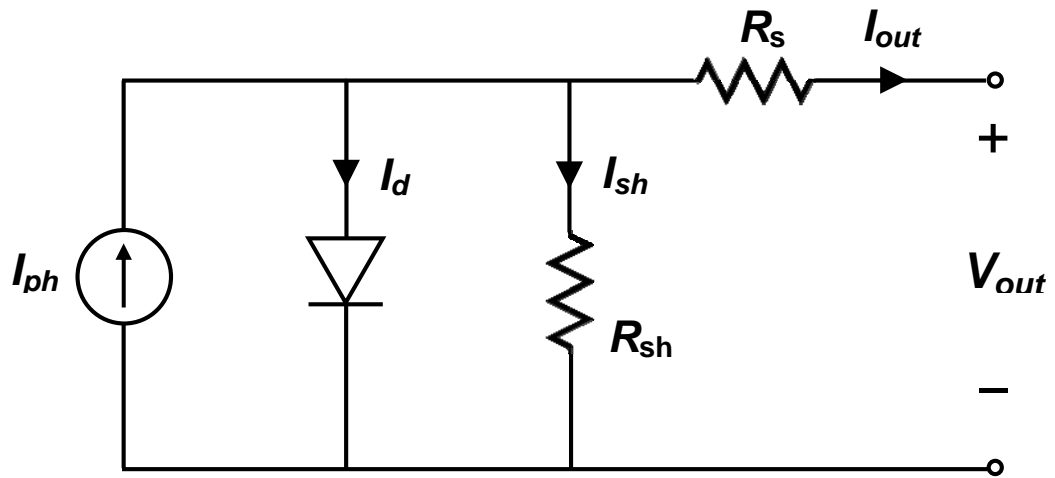
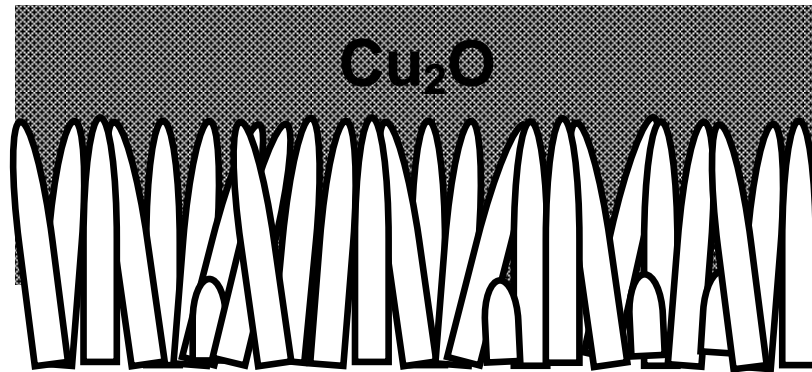
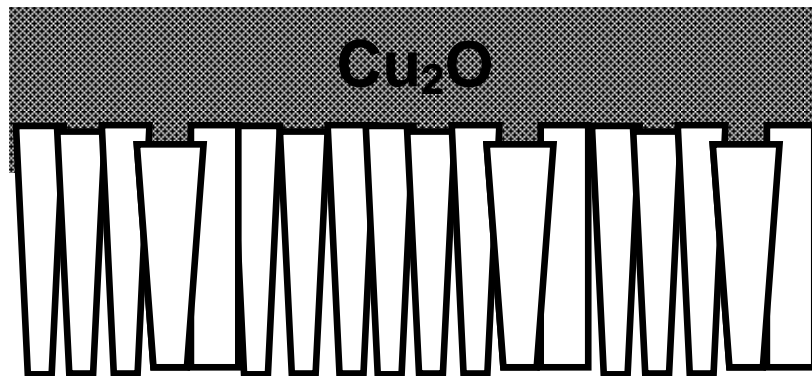


Figure 5.18 Equivalent circuit of the solar cell, where I_{ph} , I_d and I_{sh} are photogenerated current, dark current and shunt current, respectively.



(a)



(b)

Figure 5.19 (a) Schematic image of the interface between Cu_2O and ZnO , showing a relatively big junction area; (b) Schematic image of the interface between Cu_2O and $\text{Mg}_{0.1}\text{Zn}_{0.9}\text{O}$, showing a relatively small junction area.

As shown in Table 1, R_{sh} value increases with increasing Mg concentration, from 189 Ωcm^2 for ZnO to 677 Ωcm^2 for $\text{Mg}_{0.1}\text{Zn}_{0.9}\text{O}$, indicating a decrease of the PHCPs with increasing Mg. In addition to the defects contribution, the surface morphology also impact the PHCP. Fig. 5.9 (a) and (b) show different surface morphologies between $\text{Mg}_x\text{Zn}_{1-x}\text{O}$ ($x=0.1$) and ZnO ($x=0$) films, which result in the different effective junction area between $\text{Mg}_x\text{Zn}_{1-x}\text{O}$ and Cu_2O . The Cu_2O -ZnO heterojunction have a larger effective junction area than that of the Cu_2O - $\text{Mg}_{0.1}\text{Zn}_{0.9}\text{O}$ cell, due to the nanorods-like surface of ZnO in comparison to the relatively smooth surface of $\text{Mg}_{0.1}\text{Zn}_{0.9}\text{O}$, as shown in Fig. 5.19. A larger junction area is favorable for generating more electron/hole pairs, hence a higher photocurrent, however, it would concomitantly possesses more interface defects and grain boundaries. As shown in Table 1, the Cu_2O -ZnO cell has lower R_{sh} due to higher PHCPs than that of Cu_2O - $\text{Mg}_{0.1}\text{Zn}_{0.9}\text{O}$. The lower R_{sh} in Cu_2O -ZnO degrades V_{OC} values (a deviation of 279 mV from the real V_{OC} to the theoretical one) more than that of Cu_2O - $\text{Mg}_{0.1}\text{Zn}_{0.9}\text{O}$ (a deviation of 155 mV).

5.3 Summary

In summary, $\text{Mg}_x\text{Zn}_{1-x}\text{O}$ nanostructures and polycrystalline films were used in P3HT- $\text{Mg}_x\text{Zn}_{1-x}\text{O}$ hybrid solar cells and Cu_2O - $\text{Mg}_x\text{Zn}_{1-x}\text{O}$ heterojunction thin film solar cells, respectively. A unique 3-D structure, consisting of 1-D $\text{Mg}_x\text{Zn}_{1-x}\text{O}$ nanotips and 2-D GZO films was used as a photoelectrode in P3HT- $\text{Mg}_x\text{Zn}_{1-x}\text{O}$ hybrid solar cells. The 1-D $\text{Mg}_x\text{Zn}_{1-x}\text{O}$ nanotips was desgined not only to improve carrier generation and transportation but also to adjust the band offset between $\text{Mg}_x\text{Zn}_{1-x}\text{O}$ and P3HT and hence to increase the V_{OC} of the solar cell. The preliminary testing results show that $\text{Mg}_x\text{Zn}_{1-x}\text{O}$ is

promising to be used in hybrid polymer solar cells for the enhancement of V_{OC} , although further optimization of solar cells performances is needed. Besides that, we also demonstrated $Cu_2O-Mg_xZn_{1-x}O$ heterojunction thin film solar cells, in which $Mg_xZn_{1-x}O$ polycrystalline films were grown on FTO substrates by MOCVD and Cu_2O films were deposited on $Mg_xZn_{1-x}O$ films by electrodeposition. The solar cells show enhanced V_{OC} and solar conversion efficiency $\eta_{AM1.5}$ with increasing Mg composition until 10%. The solar conversion efficiency $\eta_{AM1.5} = 0.71\%$, with $J_{SC} = 3.0 \text{ mA/cm}^2$ and $V_{OC} = 575 \text{ mV}$ were obtained in the $Cu_2O-Mg_{0.1}Zn_{0.9}O$ cell. Further increasing of Mg incorporation ($>10\%$) would increase the resistivity of $Mg_xZn_{1-x}O$ films and degrade the quality of Cu_2O films made by the electrodeposition, therefore, result in poor cell performance. The effects of Mg composition in $Mg_xZn_{1-x}O$ on the open circuit voltage of the solar cells were investigated. It was found that Mg incorporation into ZnO reduced the conduction band offset between $Mg_xZn_{1-x}O$ and Cu_2O , resulting in an increase of V_{OC} . Furthermore, the Mg incorporation ($0 \leq x \leq 0.1$) increased the R_{sh} , correspondingly improves V_{OC} value.

Chapter 6 Conclusions and Suggestions for Future Work

6.1 Conclusions

In this dissertation, we developed the MOCVD growth technology of $\text{Mg}_x\text{Zn}_{1-x}\text{O}$ polycrystalline films and single crystalline nanostructures for photovoltaic applications. $\text{Mg}_x\text{Zn}_{1-x}\text{O}$ films have been used in several types of solar cells including organic-inorganic hybrid solar cells and inorganic thin film solar cells. The surface morphology of $\text{Mg}_x\text{Zn}_{1-x}\text{O}$ plays important roles on performances of various solar cells. One-dimensional (1-D) single crystalline semiconductor nanostructures are advantageous in excitonic solar cells, since the nanostructured 1-D architecture provides a larger surface and hence interface area (i.e. charge generation area) and faster electron transport path. On the other hand, the two-dimensional (2-D) film with smooth surface is needed for conventional inorganic solar cells, in which rough film surface could lead to large interface area and hence high recombination probabilities. Both $\text{Mg}_x\text{Zn}_{1-x}\text{O}$ 1-D nanostructures and 2-D films can be grown by MOCVD and the surface morphology switch between 1-D nanostructures and 2-D films can be controlled by using buffer layers.

2-D $\text{Mg}_x\text{Zn}_{1-x}\text{O}$ polycrystalline films are sequentially grown on GZO films using MOCVD. The GZO film is first grown on glass substrates at a relatively low substrate temperature T_s ($\sim 400^\circ\text{C}$), which produces a smooth surface and low resistivity of the film. Then the $\text{Mg}_x\text{Zn}_{1-x}\text{O}$ film is grown on the GZO film at a relatively high T_s ($\sim 500^\circ\text{C}$). As-grown $\text{Mg}_x\text{Zn}_{1-x}\text{O}$ film is highly crystalline with good optical properties but with a rough surface (roughness, rms value ~ 18 nm). Such rough surface is unfavorable for making the conventional p-n junction solar cells. In order to modify the surface

morphology of $\text{Mg}_x\text{Zn}_{1-x}\text{O}$ films, a LT ($\sim 250^\circ\text{C}$) ZnO buffer layer (~ 20 nm) is grown initially followed by subsequent HT ($\sim 500^\circ\text{C}$) growth of $\text{Mg}_x\text{Zn}_{1-x}\text{O}$ films. By using the LT ZnO buffer, the $\text{Mg}_x\text{Zn}_{1-x}\text{O}$ film becomes dense and smooth with a reduced surface roughness (~ 8 nm). A growth mechanism is proposed to explain the LT ZnO buffer effect on the surface morphology of $\text{Mg}_x\text{Zn}_{1-x}\text{O}$ film. The LT buffer changes the surface energy and morphology of GZO film surface and thus changes the nucleation behavior of the following growth of $\text{Mg}_x\text{Zn}_{1-x}\text{O}$, leading to a microstructure change of the $\text{Mg}_x\text{Zn}_{1-x}\text{O}$ film compared to that without using a LT ZnO buffer. The microstructure of $\text{Mg}_x\text{Zn}_{1-x}\text{O}$ films changes from one with c-axis preferred orientation to one with $[10\text{-}10]$ preferred orientation, which should be responsible for the improvement of surface roughness.

Growth of 1-D $\text{Mg}_x\text{Zn}_{1-x}\text{O}$ nanostructures by MOCVD is optimized on Si substrates firstly. It is found that a high T_s (530°C - 560°C) is good for the formation of nanostructures. However, too high T_s ($>560^\circ\text{C}$) increases the phase reaction probability, making nanostructures non-uniform. Besides that, Mg incorporation is reduced with the increase of T_s . In order to achieve high Mg content in $\text{Mg}_x\text{Zn}_{1-x}\text{O}$ nanostructures, a low DEZn flow rate (25 sccm) is preferred. The optimum chamber pressure of ~ 60 torr is needed for growth of $\text{Mg}_x\text{Zn}_{1-x}\text{O}$ nanotips. It is also found that a HT ($\sim 520^\circ\text{C}$) ZnO buffer layer (~ 30 nm) plays a critical role in the growth of $\text{Mg}_x\text{Zn}_{1-x}\text{O}$ nanostructures. It could serve as a template layer or a nucleation layer inducing the sequential growth of $\text{Mg}_x\text{Zn}_{1-x}\text{O}$ nanostructures. 1-D $\text{Mg}_x\text{Zn}_{1-x}\text{O}$ ($0 \leq x \leq 0.10$) nanostructures are also grown on GZO films for photovoltaic applications. A HT ($\sim 520^\circ\text{C}$) ZnO buffer layer (~ 30 - 50 nm) is also used, which serves as a nanostructured template for nucleation. The $\text{Mg}_x\text{Zn}_{1-x}\text{O}$ adatoms will follow the crystallographic alignment of that template to grow into 1-D nanostructures. It is

still challenging to grow $\text{Mg}_x\text{Zn}_{1-x}\text{O}$ nanostructures on GZO films with x value higher than 0.1, which could be related to the reduced surface energy anisotropy of $\text{Mg}_x\text{Zn}_{1-x}\text{O}$ with the increase of x .

1-D $\text{Mg}_x\text{Zn}_{1-x}\text{O}$ nanostructures grown on 2-D GZO films form a promising 3-D photoelectrode, which has been implemented into the $\text{Mg}_x\text{Zn}_{1-x}\text{O}$ -P3HT hybrid solar cells. The preliminary testing results of solar cells show that the V_{OC} gets improved with the increase of Mg content (less than 10% in this dissertation work). The predicted and measured V_{OC} values of solar cells as function of Mg contents are found to be in good agreement. In addition, the annealing effects on solar cell performances are investigated. Annealing (150°C for 10 min in air) significantly improves the device characteristics. The reasons could be attributed to several factors (i) oxidation of Ag layer at the P3HT interface, probably improving the electron blocking, (ii) better impregnation of P3HT in the nanostructures, and (iii) improvement of hole mobility in P3HT.

$\text{Mg}_x\text{Zn}_{1-x}\text{O}$ films are used as the n-type semiconductor and a window layer in Cu_2O - $\text{Mg}_x\text{Zn}_{1-x}\text{O}$ heterojunction solar cells. The bandgap engineering of $\text{Mg}_x\text{Zn}_{1-x}\text{O}$ is designed to modify the band offset between $\text{Mg}_x\text{Zn}_{1-x}\text{O}$ and Cu_2O and thus increase V_{OC} and solar performances of solar cells. The preliminary testing results show that V_{OC} is improved, increasing from 251 mV for the ZnO-based device, up to 575 mV for the $\text{Mg}_{0.1}\text{Zn}_{0.9}\text{O}$ -based one. The highest solar conversion efficiency is obtained on the $\text{Mg}_{0.1}\text{Zn}_{0.9}\text{O}$ sample, $\eta_{\text{AM1.5}} = 0.71\%$, with the $J_{\text{SC}} = 3.0 \text{ mA/cm}^2$ and $V_{\text{OC}} = 575 \text{ mV}$. The band alignment of Cu_2O - $\text{Mg}_x\text{Zn}_{1-x}\text{O}$ heterojunction is measured by XPS to understand the Mg effect on V_{OC} . It is found that Mg incorporation into ZnO reduces the conduction band offset between $\text{Mg}_x\text{Zn}_{1-x}\text{O}$ and Cu_2O , resulting in an increase of V_{OC} . Furthermore, the Mg

incorporation ($x \leq 0.1$) increases the shunt resistance R_{sh} , correspondingly improves V_{oc} value. These results show that $Mg_xZn_{1-x}O$ has become a promising photovoltaic material because of its tunable bandgap values and controllable surface morphology.

6.2 Suggestions for Future Work

Up to date, most research on $Mg_xZn_{1-x}O$ has been focused on the epitaxial films grown on various lattice-matched substrates for electronics and optoelectronics applications. There have been few reports on $Mg_xZn_{1-x}O$ polycrystalline films and single crystalline nanostructures for photovoltaics. In this dissertation, we developed $Mg_xZn_{1-x}O$ polycrystalline films and single crystalline nanostructures by MOCVD for Cu_2O - $Mg_xZn_{1-x}O$ heterojunction thin film solar cells and P3HT- $Mg_xZn_{1-x}O$ hybrid solar cells, respectively. However, there are still many problems needed to be solved and the solar cells performances can be further improved.

$Mg_xZn_{1-x}O$ polycrystalline films: The growth of $Mg_xZn_{1-x}O$ polycrystalline films needs to be further optimized. The proposed growth mechanism for explaining how the LT ZnO buffer influence the surface morphology and roughness of $Mg_xZn_{1-x}O$ polycrystalline films needs to be further experimentally proved. Besides GZO films, other transparent conductive electrodes (FTO or ITO), metals or other p-type semiconductor films can become substrates for the growth of $Mg_xZn_{1-x}O$ polycrystalline films for different applications. The growth of $Mg_xZn_{1-x}O$ polycrystalline films on such substrates needs to be systematically investigated.

Mg_xZn_{1-x}O nanostructures: There are two targets to realize successful growth of 1-D Mg_xZn_{1-x}O nanostructures. The first one is to achieve the expected morphology, i.e. nanotips. The second is to reach enough high Mg composition. However, more Mg incorporation brings more difficulties on forming nanotips. So far, the highest Mg composition we have achieved is 15% for Mg_xZn_{1-x}O nanotips grown on Si substrate and 10% for Mg_xZn_{1-x}O nanotips grown on GZO films, respectively. Further optimization on substrate temperature, O/Zn precursors flow rate ratio, chamber pressure, buffer layer thickness etc. has to be done to get Mg_xZn_{1-x}O nanotips with higher Mg composition (>10%). Since the surface status (e.g. defects, steps, chemical bonding) of GZO films can influence the nucleation behavior and thus the film structure development, the growth of GZO films also needs to be optimized for the subsequent growth of Mg_xZn_{1-x}O nanotips with higher Mg composition (>10%). The microstructure, texture, surface roughness and morphology of GZO films should be well controlled through growth.

P3HT-Mg_xZn_{1-x}O hybrid solar cells: So far, the solar conversion efficiency of the cells is still low. The reason could be attributed to (i) poor hole transportation in polymer semiconductor P3HT, (ii) poor impregnation of P3HT in Mg_xZn_{1-x}O nanostructures, (iii) big leakage current due to poor junction interface quality. Therefore, the further improvement of solar cell performances should be focused on optimizing the thickness of Mg_xZn_{1-x}O nanotips, thickness of the P3HT layer, the impregnation of P3HT in Mg_xZn_{1-x}O nanotips, contact quality of electrodes. The effects of Mg composition on the solar cell performances should be investigated. Blocking layers and antireflective coatings should also be considered to further improve the solar conversion efficiency.

Cu₂O-Mg_xZn_{1-x}O heterojunction thin film solar cells: The highest solar conversion efficiency that we have gotten for such solar cells is around 0.7%, which is far below the theoretical maximum power conversion efficiency (Shockley-Queisser limit) of Cu₂O, ~20%. We demonstrated an effective way to increase the V_{OC} and hence the solar conversion efficiency. But there are still many improvements can be done to further enhance the efficiency, which are: (i) modifying the electrical properties of Mg_xZn_{1-x}O films through in-situ doping during MOCVD growth, e.g. Ga-doping, to reduce the series resistance, (ii) modifying the surface morphology and roughness of Mg_xZn_{1-x}O films to increase the shunt resistance, (iii) modifying the electrical properties of Cu₂O films to improving the holes transportation, (iv) changing FTO with GZO to reduce the cost and concomitantly to reduce the contact resistance between electrode and Mg_xZn_{1-x}O films, and (v) optimizing thickness of Mg_xZn_{1-x}O films and Cu₂O films.

References

- [1] B. Li, L. Wang, B. Kang, P. Wang, Y. Qiu, *Sol. Energy Mater. Sol. Cells* 90, 549 (2006).
- [2] K. Keis, E. Magnusson, H. Lindstrom, S. E. Lindquist, A. Hagfeldt, *Sol. Energy Mater. Sol. Cells* 73, 51(2002).
- [3] M. Law, L. E. Greene, J. C. Johnson, R. Saykally, P. Yang, *Nat. Mater.* 4, 455 (2005).
- [4] J. B. Baxter, E. S. Aydil, *Appl. Phys. Lett.* 86, 053114 (2005).
- [5] A. D. Pasquier, H. Chen, and Y. Lu, *Appl. Phys. Lett.* 89, 253513 (2006).
- [6] I. Gonzalez-Valls, M. Lira-Cantu, *Energy Environ. Sci.* 2, 19–34 (2009).
- [7] A. M. Peiro, P. Ravirajan, K. Govender, D. S. Boyle, P. O'Brien, D. D. C. Bradley, J. Nelson, J. R. Durrant, *J. Mater. Chem.* 16, 2088 (2006).
- [8] S. D. Oosterhout, M. M. Wienk, S. S. van Bavel, R. Thiedmann, L. Jan Anton Koster, J. Gilot, J. Loos, V. Schmidt, R. A. J. Janssen, R. J. Janssen, *Nat. Mater.* 8, 818-824 (2009).
- [9] A. Mittiga, E. Salza, F. Sarto, M. Tucci and R. Vasanthi, *Appl. Phys. Lett.* 88, 163502 (2006).
- [10] M. Izaki, T. Shinagawa, K. Mizuno, Y. Ida, M. Inaba, A. Tasaka, *J. Phys. D: Appl. Phys.* 40, 3326-3329 (2007).
- [11] M. A. Contreras, K. Ramanathan, J. AbuShama, F. Hasoon, D. L. Young, B. Egaas, R. Noufi, *Progr. Photovolt. Res. Appl.* 13, 209 (2005).
- [12] A. Yamada, K. Matsubara, K. Sakurai, S. Ishizuka, H. Tampo, P. J. Fons, K. Iwata, S. Niki, *Appl. Phys. Lett.* 85, 5607-5609 (2004).
- [13] T. Minemoto, Y. Hashimoto, W. Shams-Kolahi, T. Satoh, T. Negami, H. Takakura, Y. Hamakawa, *Sol. Energy Mater. Sol. Cells* 75, 121-126 (2003).
- [14] D. C. Olson, S. E. Shaheen, M. S. White, W. J. Mitchell, M. F. A. M. van Hest, R. T. Collins, D. S. Ginley, *Adv. Funct. Mater.* 17, 264-269 (2007).
- [15] B. A. Gregg, *J. Phys. Chem. B* 107, 4688-4698 (2003).
- [16] A. Ohtomo, M. Kawasaki, T. Koida, K. Masubuchi, H. Koinuma, *Appl. Phys. Lett.* 72, 2466-2468 (1998).
- [17] T. Takagi, H. Tanaka, S. Fujita, S. Fujita, *Jpn. J. Appl. Phys.* 42, L401-L403 (2003).
- [18] T. Minemoto, T. Negami, S. Nishiwaki, H. Takakura, Y. Hamakawa, *Thin Solid Films* 372, 173-176 (2000).
- [19] S. Muthukumar, Y. Chen, J. Zhong, F. Cosandey, Y. Lu, T. Siegrist, *J. Cryst. Growth* 261, 316-323 (2004).
- [20] Z. Ji, Y. Song, Y. Xiang, K. Liu, C. Wang, Z. Ye, *J. Cryst. Growth* 265, 537-540 (2004).

- [21] Y. Jin, B. Zhang, S. Yang, Y. Wang, J. Chen, H. Zhang, C. Huang, C. Cao, H. Cao, R. P. H. Chang, *Solid State Commun.* 119, 409-413 (2001).
- [22] Y. Zhang, G. Du, D. Liu, H. Zhu, Y. Cui, X. Dong, S. Yang, *J. Cryst. Growth* 268, 140–143 (2004).
- [23] F. Y. Meng, Y. Chiba, A. Yamada, M. Konagai, *Sol. Energy Mater. Sol. Cells* 91, 1887-1891 (2007).
- [24] W. B. Pearson, *A Handbook of Lattice Spacings and Structures of Metals and Alloys*, New York: Pergamon Press. vol. 2, 1967.
- [25] E. R. Segnit, A. E. Holland, *J. Am. Ceram. Soc.* 48, 412 (1965).
- [26] A. Ohtomo, M. Kawasaki, I. Ohkubo, H. Koinuma, T. Yasuda, and Y. Segawa, *Appl. Phys. Lett.* 75, 980-982 (1999).
- [27] A. Ohtomo, R. Shiroki, I. Ohkubo, H. Koinuma, and M. Kawasaki, *Appl. Phys. Lett.* 75, 4088-4090 (1999).
- [28] W. Yang, S. S. Hullavarad, B. Nagaraj, I. Takeuchi, R. P. Sharma, T. Venkatesan, R. D. Vispute, H. Shen, *Appl. Phys. Lett.* 82, 3424 (2003).
- [29] S. Fujita, et al. *Phys. Stat. Sol. (b)* 241, 599 (2004).
- [30] A. Tsukazaki, A. Ohtomo, T. Kita, Y. Ohno, H. Ohno, M. Kawasaki, *Science* 315, 1388 (2007).
- [31] Z. Vashaei, T. Minegishi, T. Yao, *J. Cryst. Growth* 306, 269 (2007).
- [32] C.-H. Lee, J. Yoo, Y.-J. Doh, G.-C. Yi, *Appl. Phys. Lett.* 94, 043504 (2009).
- [33] A. Ohtomo, K. Tamura, M. Kawasaki, T. Makino, Y. Segawa, Z. K. Tang, G. K. L. Wong, Y. Matsumoto, H. Koinuma, *Appl. Phys. Lett.* 77, 2204 (2000).
- [34] W. I. Park, G.-C. Yi, M. Kim, S. J. Pennycook, *Adv. Mater.* 15, 526 (2003).
- [35] T. Makino, C. H. Chia, Nguen T. Tuan, H. D. Sun, Y. Segawa, M. Kawasaki, A. Ohtomo, K. Tamura, H. Koinuma, *Appl. Phys. Lett.* 77, 975 (2000).
- [36] T. Makino, C. H. Chia, Nguen T. Tuan, Y. Segawa, M. Kawasaki, A. Ohtomo, K. Tamura, H. Koinuma, *Appl. Phys. Lett.* 77, 1632 (2000).
- [37] G. Coli, K. K. Bajaji, *Appl. Phys. Lett.* 78, 2861 (2001).
- [38] C. H. Chia, T. Makino, Y. Segawa, M. Kawasaki, A. Ohtomo, K. Tamura, H. Koinuma, *Appl. Phys. Lett.* 90, 3650 (2001).
- [39] B. P. Zhang, N. T. Binh, K. Wakatsuki, C. Y. Liu, Y. Segawaa, N. Usami, *Appl. Phys. Lett.* 86, 032105 (2005).
- [40] M. Brandt, H. von Wenckstern, M. Stölzel, H. Hochmuth, M. Lorenz, M. Grundmann, *Semicond. Sci. Technol.* 26, 014040 (2011).
- [41] N. B. Chen, C. H. Sui, *Mater. Sci. Eng. B* 126, 16 (2006).
- [42] A. Janotti, C. G. Van de Walle, *Rep. Prog. Phys.* 72, 126501 (2009).

- [43] N. W. Emanetoglu, S. Muthukumar, P. Wu, R. H. Wittstruck, Y. Chen, Y. Lu, IEEE Transactions on Ultrasonics, Ferroelectrics and Frequency Control 50, 537 (2003).
- [44] Y. Chen, G. Saraf, Y. Lu, L. S. Wielunski, T. Siegrist, J. Vac. Sci. Technol. A 25, 857 (2007).
- [45] Y. Kwon, Y. Li, Y. W. Heo, M. Jones, P. H. Holloway, D. P. Norton, Z. V. Park, S. Li, Appl. Phys. Lett. 84, 2685 (2004).
- [46] A. Ohtomo, S. Takagi, K. Tamura, T. Makino, Y. Segawa, H. Koinuma, M. Kawasaki, Jpn. J. Appl. Phys. 45, L694 (2006).
- [47] C.-J. Ku, Z. Duan, P. I. Reyes, Y. Lu, Y. Xu, C.-L. Hsueh, E. Garfunkel, Appl. Phys. Lett. 98, 025112 (2011).
- [48] W. Yang, R. D. Vispute, S. Choopun, R. P. Sharma, T. Venkatesana, H. Shen, Appl. Phys. Lett. 78, 2787 (2001).
- [49] Z. G. Ju, C. X. Shan, D. Y. Jiang, J. Y. Zhang, B. Yao, D. X. Zhao, D. Z. Shen, X. W. Fan, Appl. Phys. Lett. 93, 173505 (2008).
- [50] L. K. Wang, Z. G. Ju, J. Y. Zhang, J. Zheng, D. Z. Shen, B. Yao, D. X. Zhao, Z. Z. Zhang, B. H. Li, C. X. Shan, Appl. Phys. Lett. 95, 131113 (2009).
- [51] X. M. Chen, G. H. Wu, D. H. Bao, Appl. Phys. Lett. 93, 093501 (2008).
- [52] X. M. Chen, G. H. Wu, P. Jiang, W. F. Liu, D. H. Bao, Appl. Phys. Lett. 94, 033501 (2009).
- [53] D. C. Kim, B. H. Kong, S. K. Mohanta, H. K. Cho, J. H. Park, J. B. Yoo, Cryst. Growth Des. 9, 4308 (2009).
- [54] Y. W. Heo, Y. W. Kwon, Y. Li, S. J. Pearton, D. P. Norton, Appl. Phys. Lett. 84, 3474 (2004).
- [55] X. Zhang, X. M. Li, T. L. Chen, C. Y. Zhang, W. D. Yu, Appl. Phys. Lett. 87, 092101 (2005).
- [56] Z. P. Wei, B. Yao, Z. Z. Zhang, Y. M. Lu, D. Z. Shen, B. H. Li, X. H. Wang, J. Y. Zhang, D. X. Zhao, X. W. Fan, Z. K. Tang, Appl. Phys. Lett. 89, 102104 (2006).
- [57] Y. F. Li, B. Yao, R. Deng, B. H. Li, J. Y. Zhang, Y. M. Zhao, D. Y. Jiang, Z. Z. Zhang, C. X. Shan, D. Z. Shen, X. W. Fan, Y. M. Lu, J. Phys. D: Appl. Phys. 42, 105102 (2009).
- [58] S. Muthukumar, J. Zhong, Y. Chen, Y. Lu, T. Siegrist, Appl. Phys. Lett. 82, 742 (2003).
- [59] C. X. Cong, B. Yao, Y. P. Xie, G. Z. Xing, B. H. Li, X. H. Wang, Z. P. Wei, Z. Z. Zhang, Y. M. Lv, D. Z. Shen, X. W. Fan, J. Mater. Res. 22, 2936 (2007).
- [60] J. Y. Moon, J. H. Kim, H. Kim, H. S. Lee, Y. Y. Kim, H. K. Cho, H. S. Kim, Thin Solid Films 517, 3931 (2009).
- [61] D. Zhao, Y. Liu, D. Shen, Y. Lu, J. Zhang, X. Fan, J. Appl. Phys. 90, 5561 (2001).
- [62] S. R. Meher, K. P. Biju, M. K. Jain, J. Sol-Gel Sci. Technol. 52, 228 (2009).

- [63] B. K. Sonawane, M. P. Bhole, D. S. Patil, *Physica B* 405, 1603 (2010).
- [64] Y. Chiba, F. Meng, A. Yamada, M. Konagai, *Jap. J. Appl. Phys.* 46, 5040 (2007).
- [65] T. Terasako, S. Shirakata, T. Kariya, *Thin Solid Films* 420-421, 13 (2002).
- [66] X. Zhang, X. M. Li, T. L. chen, J. M. Bian, C. Y. Zhang, *Thin Solid Films* 492, 248 (2005).
- [67] W. Li, E. Shi, W. Zhong, Z. Yin, *J. Cryst. Growth* 203, 186 (1999).
- [68] M. Kim, Y. Hong, J. Yoo, G. Yi, G. Park, K. Kong, H. Chang, *Phys. Status Solidi RPL* 2, 197-199 (2008).
- [69] J. Yoo, Y. J. Hong, G.-C. Yi, B. Chon, T. Joo, *Semicond. Sci. Technol.* 23, 095015 (2008).
- [70] C. H. Ku, H. H. Chiang, J. J. Wu, *Chem. Phys. Lett.* 404, 132 (2005).
- [71] J. R. Wang, Z. Z. Ye, J. Y. Huang, Q. B. Ma, X. Q. Gu, H. P. He, L. P. Zhu, J. G. Lu, *Mater. Lett.* 62, 1263-1266 (2008).
- [72] D. C. Kim, J. H. Lee, S. K. Mohanta, H. K. Cho, H. Kim, J. Y. Lee, *Cryst. Eng. Comm.* 13, 813-818 (2011).
- [73] S. Muthukumar, H. Sheng, J. Zhong, Z. Zhang, N. W. Emanetoglu, Y. Lu, *IEEE Trans. Nanotechnol.* 2, 50 (2003).
- [74] D. C. Kim, J. H. Lee, S. K. Mohanta, H. K. Cho, J. Y. Lee, *Nanotechnology* 21, 425503 (2010) .
- [75] B. H. Kong, S. O. Jun, Y. Y. Kim, D. C. Kim, H. K. Cho, *Phys. Stat. Sol. (b)* 244, 1517-1521 (2007).
- [76] M. Zhi, L. Zhu, Z. Ye, F. Wang, B. Zhao, *J. Phys. Chem. B* 109, 23930-23934 (2005) .
- [77] H. Tang, H. He, L. Zhu, Z. Ye, M. Zhi, F. Yang, B. Zhao, *J. Phys. D: Appl. Phys.* 39, 3764-3768 (2006)
- [78] L. Zhu, M. Zhi, Z. Ye, B. Zhao, *Appl. Phys. Lett.* 88, 113106 (2006).
- [79] Y. Z. Zhang, J. G. Lu, Z. Z. Ye, Y. J. Zeng, L. P. Zhu, J. Y. Huang, *J. Phys. D: Appl. Phys.* 40, 3490-3493 (2007).
- [80] Y. W. Heo, M. Kaufman, K. Pruessner, D. P. Norton, F. Ren, M. F. Chisholm, P. H. Fleming, *Solid-State Electron.* 47, 2269-2273 (2003).
- [81] M. Lorenz, E. M. Kaidashev, A. Rahm, Th. Nobis, J. Lenzner, G. Wagner, D. Spemann, H. Hochmuth, M. Grundmann, *Appl. Phys. Lett.* 86, 143113 (2005).
- [82] H. Y. Yang, S. P. Lau, S. F. Yu, M. Tanemura, T. Okita, H. Hatano, K. S. Teng, S. P. Wilks, *Appl. Phys. Lett.* 89, 081107 (2006).
- [83] C. J. Pan, H. C. Hsu, H. M. Cheng, C. Y. Wu, W. F. Hsieh, *J. Solid State Chem.* 180, 1188-1192 (2007).

- [84] D. L. Smith, *Thin-film deposition: principles and practice*, McGraw-Hill, Inc. New York, 1995.
- [85] M. Farnsworth, C. H. Kline, J. G. Noltes, *Zinc Chemical*, International Lead Zinc Research Organization, Inc. New York, 1973.
- [86] M. H. Abraham, J. Chem. Soc. 4130 (1960).
- [87] M. L. Timmons, P. K. Chiang, and S. V. Hattangady, J. Cryst. Growth, 77, 37-41 (1986).
- [88] M. Law, L. E. Greene, J. C. Johnson, R. Saykally, P. Yang, Nat. Mater. 4, 455-459 (2005).
- [89] A. Yamada, K. Matsubara, K. Sakurai, S. Ishizuka, H. Tampo, P. J. Fons, K. Iwata, S. Niki, Appl. Phys. Lett. 85, 5607-5609 (2004).
- [90] H. Chen, A. Du Pasquier, G. Saraf, J. Zhong, Y. Lu, Semicond. Sci. Technol. 23, 045004 (2008).
- [91] T.-J. Hsueh, C.-L. Hsu, S.-J. Chang, P.-W. Guo, J.-H. Hsieh, I.-C. Chen, Scr. Mater. 57, 53-56 (2007).
- [92] H. Chen, Z. Duan, Y. Lu, A. Du Pasquier, J. Electron. Mater. 38, 1612 (2009).
- [93] Y. Li, G. S. Tompa, S. Liang, C. Gorla, Y. Lu, J. Doyle, J. Vac. Sci. Technol. A 15, 1063 (1997).
- [94] V. Bhosle, A. Tiwari, J. Narayan, J. Appl. Phys. 100, 033713 (2006).
- [95] V. Khranovskyy, U. Grossner, O. Nilsen, V. Lazorenko, G. V. Lashkarev, B. G. Svensson, R. Yakimova, Thin Solid Films 515, 472-476 (2006).
- [96] J. J. Robbins, J. Harvey, J. Leaf, C. Fry, C. A. Wolden, Thin Solid Films 473, 35 (2005).
- [97] Y. Kajikawa, J. Cryst. Growth 289, 387-394 (2006).
- [98] H. J. Ko, Y. F. Chen, J. M. Ko, T. Hanada, Z. Zhu, T. Fukuda, T. Yao, J. Cryst. Growth 207, 87-94 (1999).
- [99] A. Dadgar, N. Oleynik, D. Forster, S. Deiter, H. Witek, J. Bläsing, F. Bertram, A. Krtischil, A. Diez, J. Christen, A. Krost, J. Cryst. Growth 267, 140-144 (2004).
- [100] J. F. Yan, Y. M. Lu, Y. C. Liu, H. W. Liang, B. H. Li, D. Z. Shen, J. Y. Zhang, X. W. Fan, J. Cryst. Growth 266, 505-510 (2004).
- [101] F. Xiu, Z. Yang, D. Zhao, J. Liu, K. A. Alim, A. A. Balandin, M. E. Itkis, R. C. Haddon, J. Cryst. Growth 286, 61-65 (2006).
- [102] Y.-K. Tseng, C.-J. Huang, H.-M. Cheng, I.-N. Lin, K.-S. Liu, I.-C. Chen, Adv. Funct. Mater. 13, 811-814 (2003).
- [103] K. Ogata, K. Maejima, Sz. Fujita, Sg. Fujita, J. Cryst. Growth, 248, 25 (2003).
- [104] X. Ni, Y. Fu, Y. T. Moon, N. Biyikli, H. Morkoç, J. Cryst. Growth, 290, 166 (2006).

- [105] V. Khranovskyy, R. Minikayev, S. Trushkin, G. Lashkarev, V. Lazorenko, U. Grossner, W. Paszkowicz, A. Suchocki, B. G. Svensson, R. Yakimova, *J. Cryst. Growth* 308, 93 (2007).
- [106] T. Nakamura, Y. Yamada, T. Kusumori, H. Minoura, H. Muto, *Thin Solid Films* 411, 60 (2002).
- [107] S. Muthukumar, C. R. Gorla, N. W. Emanetoglu, S. Liang, and Y. Lu, *J. Cryst. Growth* 225, 197 (2001).
- [108] P. Misra, L. M. Kukreja, *Thin Solid Films* 485, 42 (2005).
- [109] U. Zhokhavets, T. Erb, H. Hoppe, G. Gobsch, N. S. Sariciftci, *Thin Solid Films* 496, 679 (2006).
- [110] D. C. Olson, M. S. White, Y.-J. Lee, N. Kopidakis, S. E. Shaheen, D. S. Ginley, J. A. Voigt, and J. W. P. Hsu, *J. Phys. Chem. C* 111, 16640 (2007).
- [111] B. P. Rai, *Cu₂O solar cells: A review*, *Sol. Cells* 25, 265-272 (1988).
- [112] G. K. Paul, R. Ghosh, S. K. Bera, S. Bandyopadhyay, T. Sakurai, K. Akimoto, *Chem. Phys. Lett.* 463, 117-120 (2008).
- [113] S. S. Jeong, A. Mittiga, E. Salza, A. Masci, S. Passerini, *Electrochim. Acta* 53, 2226-2231 (2008).
- [114] T. Minami, T. Miyata, K. Ihara, Y. Minamino, S. Tsukada, *Thin Solid Films* 494, 47-52 (2006).
- [115] H. Tanaka, T. Shimakawa, T. Miyata, H. Sato, T. Minami, *Thin Solid Films* 469-470, 80-85 (2004).
- [116] K. P. Musselman, A. Wisnet, D. C. Iza, H. C. Hesse, C. Scheu, J. L. MacManus-Driscoll, L. Schmidt-Mende, *Adv. Mater.* 22, E254-E258 (2010).
- [117] K. Akimoto, S. Ishizuka, M. Yanagita, Y. Nawa, G. K. Paul, T. Sakurai, *Sol. Energy* 80, 715-722 (2006).
- [118] P. W. Tasker, *The stability of ionic crystal surfaces*, *J. Phys. C: Solid State Phys.* 12, 4977-4984 (1979).
- [119] W. Li, E. Shi, W. Zhong, Z. Yin, *J. Cryst. Growth* 203, 186-196 (1999).
- [120] N. A. Mohemmed Shanid, M. Abdul Khadar, *Thin Solid Films* 516, 6245-6252 (2008).
- [121] G. G. Condorelli, G. Malandrino, I. Fragala, *Chem. Mater.* 6, 1861-1866 (1994).
- [122] P. E. De Jongh, D. Vanmaekelbergh, J. J. Kelly, *Chem. Mater.* 11, 3512-3517 (1999).
- [123] J. P. Tobin, W. Hirschwald, J. Cunningham, *Appl. Surf. Sci.* 16, 441-452 (1983).
- [124] P. E. Larson, *J. Electron Spectrosc. Relate. Phenom.* 4, 213-218 (1974).

- [125] T. Ghodselahi, M. A. Vesaghi, A. Shafiekhani, A. Baghizadeh, M. Lameii, Appl. Surf. Sci. 255, 2730-2734 (2008).
- [126] E. A. Kraut, R. W. Grant, J. R. Waldrop, S. P. Kowalczyk, Phys. Rev. Lett. 44, 1620-1623 (1980).

CURRICULUM VITAE OF ZIQING DUAN

EDUCATION

- | | |
|-----------|--|
| May 2012 | Doctor of Philosophy in Electrical & Computer Engineering
Rutgers University, New Brunswick, New Jersey 08901 |
| July 2005 | Master of Engineer in Materials Science & Engineering
Shanghai Institute of Ceramics, Chinese Academy of Sciences, China |
| July 2002 | Bachelor of Engineer in Materials Science & Engineering
Zhengzhou University, China |

RESEARCH EXPERIENCE

Research Assistant in Electrical & Computer Engineering Department (2007 – Present)

- Developed wide-bandgap semiconductor ZnO epitaxial films, amorphous/polycrystalline films, nanostructures on various substrates using MOCVD for multiple electronic devices including solar cells, thin-film transistors (TFT), memristors, Schottky diodes, and biosensors.
- Controlled the surface morphology of $\text{Mg}_x\text{Zn}_{1-x}\text{O}$ films/nanostructures through using different buffer layers for photovoltaic applications.
- Enhanced the open-circuit voltage (V_{OC}) of Cu_2O -ZnO heterojunction solar cells by adjusting the band offset between the window layer and the light absorber.
- Developed unique 3-D photoelectrodes, consisting of 1-D ZnO nanostructures and 2-D Ga-doped ZnO (GZO) films, for dye-sensitized solar cells (DSSCs) and organic-inorganic hybrid solar cells.
- Demonstrated Fe-doped ZnO nanostructures using MOCVD for memristors and improved the resistive switching performance by designing FeZnO/MgO or $\text{FeZnO}_{1+x}/\text{FeZn}_{1-x}\text{O}$ multilayers.
- Solved the problem of high background doping level of ZnO films grown by MOCVD through modifying the growth process and successfully developed enhancement-mode ZnO-based TFTs.
- Improved ZnO-based TFTs performances and thermal stability by incorporating Mg into ZnO.
- Improved ZnO-based Schottky diode performance by designing $\text{Mg}_x\text{Zn}_{1-x}\text{O/GaZnO}$ multilayers.
- Performed regular maintenance and troubleshooting of the MOCVD system.

- Performed structural, electrical and optical characterization of ZnO-based thin films/nanostructures and devices using XRD, SEM, EDX, TEM, AFM, XPS, Hall measurements, I-V, Transmission etc.

TEACHING EXPERIENCE

Teaching Assistant in Electrical & Computer Engineering Department (2007-2010)

- Taught laboratory sections of two undergraduate courses: Electronic Devices and Digital Electronics.

PUBLICATIONS

1. **Ziqing Duan**, Aurelien Du Pasquier, Yicheng Lu, Yi Xu, Eric Garfunkel, Effects of Mg Composition on Open Circuit Voltage in $\text{Cu}_2\text{O-Mg}_x\text{Zn}_{1-x}\text{O}$ Heterojunction Solar Cells, *Solar Energy Materials and Solar Cells*, 2012, 96: 292-297. (IF: 4.746)
2. **Ziqing Duan**, Yicheng Lu, Aurelien Du Pasquier, Morphological control of $\text{Mg}_x\text{Zn}_{1-x}\text{O}$ layers grown on Ga:ZnO/glass substrates for photovoltaics, *Journal of Crystal Growth*, 2011. (In Press) (IF: 1.746)
3. Yang Zhang, **Ziqing Duan**, Rui Li, Chieh-Jen Ku, Pavel I. Reyes, Almamun Ashrafi, Jian Zhong, and Yicheng Lu, Vertically Integrated ZnO 1D1R Resistive Switching Device, *Applied Physics Letters*, 2012. (to be submitted) (IF: 3.841)
4. Yang Zhang, **Ziqing Duan**, Rui Li, Chieh-Jen Ku, Pavel I. Reyes, Almamun Ashrafi, and Yicheng Lu, FeZnO-based Resistive Switching Devices, *Journal of Electronic Materials*, 2011 (Accepted) (IF: 1.421)
5. Yan Cao, Elena Galoppini, Pavel Ivanoff Reyes, **Ziqing Duan**, and Yicheng Lu, Morphology Effects on The Biofunctionalization of Nanostructured ZnO, *Langmuir*, 2012 (submitted) (IF: 4.269)
6. Pavel Ivanoff Reyes, Ji Li, **Ziqing Duan**, Xiaotian Yang, Ying Cai, Qingrong Huang and Yicheng Lu, ZnO Surface Acoustic Wave Sensors Built on Zein-Coated Flexible Food Packages, *Sensor Letters*, 2012. (submitted) (IF: 0.602)
7. Pavel Reyes, **Ziqing Duan**, Yicheng Lu, Dimitriy Khavulya and Nada Boustany, ZnO Nanostructure-Modified QCM for Dynamic Monitoring of Cell Adhesion and Proliferation, *Biosensors and Bioelectronics*, 2012. (submitted) (IF: 5.361)
8. Pavel Ivanoff Reyes, Chieh-Jen Ku, **Ziqing Duan**, Yi Xu, Eric Garfunkel and Yicheng Lu, Reduction of Persistent Photoconductivity in ZnO Thin Film Transistor-Based UV Photodetector, *Applied Physics Letters*, 2012. (submitted) (IF: 3.841)
9. Chieh-Jen Ku, **Ziqing Duan**, Pavel I. Reyes, Yicheng Lu, Yi Xu, Chien-Lan Hsueh, Eric Garfunkel, Effects of Mg on the electrical characteristics and thermal stability of $\text{Mg}_x\text{Zn}_{1-x}\text{O}$ thin film transistors, *Applied Physics Letters*, 2011, 98: 123511. (IF: 3.841)

10. Pavel Ivanoff Reyes, Chieh-Jen Ku, **Ziqing Duan**, Yicheng Lu, Aniruddh Solanki, and Ki-Bum Lee, ZnO thin film transistor immunosensor with high sensitivity and selectivity, *Applied Physics Letters*, 2011, 98: 173702. (IF: 3.841)
11. **Ziqing Duan**, Nathalie Pereira, Yicheng Lu, Aurelien Du Pasquier, Gel probe photocurrent measurement of cuprous oxide films, *Solar Energy Materials and Solar Cells*, 2010, 94:1741-1746. (IF: 4.746)
12. Aurelien Du Pasquier, **Ziqing Duan**, Nathalie Pereira, Yicheng Lu, Cuprous Oxide Solution Preparation and Application to Cu₂O-ZnO Solar Cells, *ECS Transactions*, 2010, 28 (4): 179-190.
13. Hanhong Chen, **Ziqing Duan**, Yicheng Lu, Aurelien Du Pasquier, Dye-Sensitized Solar Cells Combining ZnO Nanotip Arrays and Nonliquid Gel Electrolytes, *Journal of Electronic Materials*, 2009, 38 (8): 1612. (IF: 1.421)
14. Ying Chen, Pavel I. Reyes, **Ziqing Duan**, Gaurav Saraf, Richard Wittstruck, Yicheng Lu, Olena Taratula, Elena Galoppini, Multifunctional ZnO-Based Thin-Film Bulk Acoustic Resonator for Biosensors, *Journal of Electronic Materials*, 2009, 38 (8): 1605. (IF: 1.421)
15. Ying Chen, Gaurav Saraf, Pavel I. Reyes, **Ziqing Duan**, Jian Zhong, Yicheng Lu, Structural, electrical, and piezoelectric properties of ZnO films on SiC-6H substrates, *Journal of Vacuum Science and Technology B*, 2009, 27 (3): 1631. (IF: 1.271)
16. Pavel I. Reyes, Zheng Zhang, Hanhong Chen, **Ziqing Duan**, Jian Zhong, Gaurav Saraf, Yicheng Lu, Olena Taratula, Elena Galoppini, Nada N. Boustany, A ZnO nanostructure-based quartz crystal microbalance device for biochemical sensing, *IEEE Sensors Journal*, 2009, 9 (10): 1302. (IF: 1.473)
17. Jun Zhu, Hanhong Chen, Gaurav Saraf, **Ziqing Duan**, Yicheng Lu, S. T. Hsu, ZnO TFT Devices Built on Glass Substrates, *Journal of Electronic Materials*, 2008, 37 (8): 1237. (IF: 1.421)
18. Olena Taratula, Elena Galoppini, Richard Mendelsohn, Pavel Ivanoff Reyes, Zheng Zhang, **Ziqing Duan**, Jian Zhong, Yicheng Lu, Stepwise Functionalization of ZnO Nanotips with DNA, *Langmuir*, 2009, 25 (4): 2107–2113. (IF: 4.269)